Technische Universität München
Max-Planck-Institut für Astrophysik

Modeling detonations in Type Ia supernovae

Michael Fink

Vollständiger Abdruck der von der Fakultät für Physik der Technischen Universität München zur Erlangung des akademischen Grades eines

Doktors der Naturwissenschaften

genehmigten Dissertation.

Vorsitzender:	Univ.-Prof. Shawn Bishop, Ph.D.
Prüfer der Dissertation:	
	1. Priv.-Doz. Dr. Friedrich K. Röpke
	2. Univ.-Prof. Dr. Thorsten Feldmann

Die Dissertation wurde am 24.08.2010 bei der Technischen Universität München eingereicht und durch die Fakultät für Physik am 23.11.2010 angenommen.

Contents

1. Introduction

1.1. Detonations and Type Ia supernovae

Explosive burning can propagate through a fuel in two distinct modes that differ in the mechanism of flame propagation. In subsonic *deflagrations*, heat conduction from the hot burning products heats up the neighboring unburnt fuel until it also ignites. *Detonations*, which this work focuses on, spread by a strong shock wave that compresses and heats the matter behind it sufficiently to ignite it. Thereby, a balance is attained such that the energy release in the reactions supports the shock. As shocks propagate supersonically through a medium, this is also true for detonation waves. Thus, detonations move much faster than deflagrations and convert energy at a very rapid rate. This is the basis of their technical applications: a good solid explosive can convert energy at a rate of 10^{10} W per square centimeter of its detonation front (Fickett & Davis 1979).

Terrestrial detonations are usually powered by chemical reactions. They have been investigated extensively by both experiment and theory (see e.g. Clavin 2004, for a review of recent theoretical developments). Most of their properties can be described well by the simple one-dimensional theory of steady state detonations: the Chapman–Jouguet and the slightly more advanced Zel'dovich–von Neumann–Doering theory (see e.g. Fickett & Davis 1979). However, real detonations show very complex three-dimensional sub-structures that can be described by the steady one-dimensional theory only in an average sense; also, many phenomena are still unexplained by theory.

Detonations in astrophysical contexts, on the other hand, obey the same fundamental physics, but are powered by nuclear reactions. They act on very different length and time scales and can be by far more energetic. A site where detonations are believed to occur are *Type Ia supernovae*. By performing astronomical observations of such explosions, one can thus also learn something about detonation burning. Viewed from the opposite perspective, a sound understanding of detonation physics may be key to understanding Type Ia supernovae. This work is on the subject of detonations in Type Ia supernovae and tries to follow both these directions.

Type Ia supernovae are believed to be thermonuclear explosions in the electron degenerate matter of carbon/oxygen white dwarf (C/O WD) stars (Hoyle & Fowler 1960), which are the evolutionary end product of low mass stars. As WDs cannot gain anymore energy from nuclear fusion (as they do not reach sufficient temperatures for further reactions), a single such star is an inert object. Thus, an external trigger, like the accretion of matter from a companion star in a binary

system, is believed to trigger the explosion. Unfortunately, even after several decades of scientific research, the question of the progenitor system and the exact explosion mechanism are still open.

From an observer's perspective a Type Ia supernova is like a suddenly appearing very luminous "new star" that reaches its maximum brightness in a few days to weeks and then fades again over several months. This characteristic luminosity evolution, the light curve, is believed to be powered by the decay energy of radioactive ^{56}Ni produced in the explosion (Truran et al. 1967; Colgate & McKee 1969; Kuchner et al. 1994). Furthermore, a characteristic spectral evolution can be observed that is used to classify a supernova as Type Ia (see next section) and to distinguish it from core-collapse supernovae. Type Ia supernovae are of great importance for astrophysics: due to their extraordinary brightness (at maximum they can even outshine a whole galaxy) and homogeneity, they can be used as cosmic distance indicators; moreover, they are believed to be one of the main sources for the production of heavy elements in the universe.

In the following, a more detailed overview of the observable characteristics of Type Ia supernovae is given (Sect. 1.2) and the existing explosion models are briefly reviewed (Sect. 1.3). Then, the objectives and the organization of this work are explained (Sect. 1.4).

1.2. Observable characteristics of Type Ia supernovae

To understand the main problems of Type Ia supernova modeling, an overview of their observational properties is indispensable. The following brief review is based on Filippenko (1997a), Filippenko (1997b), and Hillebrandt & Niemeyer (2000). Supernovae are classified on the basis of their spectra. Thermonuclear or Type Ia supernovae can be distinguished from core collapse supernovae (types II, Ib, and Ic) by the following spectral characteristics (see e.g. Harkness & Wheeler 1990): Type Ia supernovae do not show hydrogen in their spectra at any time, in contrast to Type II supernovae. The main feature of Type Ia supernovae is a deep absorption trough of singly ionized silicon (Si II) near 6150 Å in their maximum-light spectra. This feature originates from the Si II doublet at 6347 Å and 6371 Å. The weighted average of these two lines at 6355 Å is then blue-shifted to ∼6150 Å (the blue-shifted absorption component in typical spectral lines of Type Ia supernovae is explained below). Type Ib and Ic supernovae also do not show any features of hydrogen in their spectra. But, instead of Si II, Type Ib supernovae have prominent lines of neutral helium (He I). Type Ic supernovae show neither Si II nor He I.

Photometrically, most Type Ia supernovae are fairly homogeneous. The temporal evolution of luminosity, the *light curve*, has a very similar shape for the majority of events. After the explosion the luminosity increases until it reaches its maximum at about 20 days ($M_B \approx M_V \approx -19.3$ mag, Hamuy et al. 1996). After maximum light the luminosity drops about 3 mag in one month. Then, the decline slows

down to a rate of about 0.5 mag per month. In this phase, the luminosity decreases exponentially, i.e., linearly in magnitudes.

Now, more detailed *spectral properties* and the basic mechanisms of spectrum formation are discussed. Typically, the lines in Type Ia supernovae show an absorption trough, which is blue-shifted relative to the resonance wavelength of the line, and an accompanying emission component to the red. This so-called P-Cygni line profile is characteristic for resonant line scattering in an optically thin expanding atmosphere that is back-illuminated by continuum radiation from an optically thick photosphere. Rather than having a real thermal continuum, Type Ia supernovae show a pseudo-continuum which results from a forest of overlapping Doppler-broadened P-Cygni lines (associated with a multitude of lines of intermediate mass and iron group elements). This is produced by the interactions of γ-rays from the decays $^{56}\mathrm{Ni} \rightarrow {}^{56}\mathrm{Co} \rightarrow {}^{56}\mathrm{Fe}$ with the expanding envelope that finally degrade the γ-rays to UV–optical–infrared radiation.

Since different lines form at different depths, the pseudo-continuum does not define a clear photosphere. Nevertheless, the few strong individual P-Cygni features which are superposed to the pseudo-continuum can be used to infer the composition of the ejecta above the continuum forming regions. Thus, the fact that features of different elements show different blue shifts, indicates a layered structure of the supernova ejecta in which different elements have different expansion velocities.

A very important observational constraint for Type Ia supernova modeling is the temporal evolution of their spectra: as the ejecta expand, the matter dilutes. Consequently, the continuum forming region recedes inwards and the most prominent spectral lines change according to the composition structure in the explosion products. Early and maximum Type Ia optical spectra are dominated by a variety of features of singly ionized and a few neutral intermediate mass elements (IMEs): O, Mg, Si, S, Ca. Therefore, these elements are expected to be produced in the outer parts of the WD. At this time there is also some contribution of iron group elements (IGEs) such as Ni, Fe, and Co in weakly ionized states. The importance of these lines increases with time; at two weeks after maximum the spectrum is already dominated by Fe II, which is consistent with an IGE-rich core. At later times, >4 weeks, the ejecta become so dilute that they are completely optically thin. This is the end of the so-called "photospheric epoch". Now, the spectra become "nebular", the pseudo-continuum disappears, and strong forbidden emission lines of Fe and Co dominate the spectrum (cf. Mazzali et al. 1993). Other (allowed) lines disappear here, as their excitation energy cannot be reached any more.

Most Type Ia supernovae form a remarkably homogeneous class of objects with very similar spectral evolution, absolute magnitude, and light curve shape (Branch et al. 1993). About 70% of events belong to these so-called *normal* Type Ia supernovae (Li et al. 2010). The remaining objects are *peculiar*; the two most frequent "classes" of peculiar objects are the sub-luminous SN 1991bg-like events (Filippenko et al. 1992b; Leibundgut et al. 1993) and the bright SN 1991T-like explosions (Phillips et al. 1992), which account for 18% and >9% of observed

Type Ia supernovae, respectively (Li et al. 2010). These peculiar events differ not only significantly in their peak brightnesses, but also in their spectral evolution.

As mentioned before, due to their high luminosity and their homogeneity, normal Type Ia supernovae are used for cosmological distance measurements. But, despite their homogeneity, they are not perfect "standard candles" (with the same absolute magnitude wherever they explode): there are deviations in both maximum brightnesses and light curve shapes. Fortunately, these deviations are correlated: the brighter the explosion, the slower is the decline of the light curve (Pskovskii 1977; Phillips 1993). The maximum brightness also seems to depend on the environment: Type Ia supernovae tend to be more luminous in spiral galaxies than in ellipticals (e.g. Hamuy et al. 1995, 1996; Branch et al. 1996; Sullivan et al. 2006). But, the above correlation between the maximum brightness and the light curve shape still holds. Thus, the peak brightnesses can be determined if the light curve shape is known and therefore Type Ia supernovae are often termed "standardizable candles". Due to their extraordinary luminosity, Type Ia supernovae have successfully been used to measure cosmological parameters (e.g. Riess et al. 1998; Perlmutter et al. 1999; Astier et al. 2006). However, one should be cautious if no independent distance indicator can be found to validate the results. As long as the exact progenitor system and the explosion mechanism are not fully understood, systematic changes in total brightness with redshift (e.g. due to to a metallicity dependence of the explosion scenario) cannot be totally excluded. Thus, for more reliability of cosmological applications, it is very important to improve theoretical models of Type Ia supernovae. An overview of currently discussed models is given in the next section.

1.3. Supernova modeling

A complex light signal is the only information of a Type Ia supernova explosion that reaches an observer. Unfortunately, this does only very indirectly provide information about the explosion mechanism and progenitor star. The actual explosion only lasts for 1–2 s; then, radioactive decays and complex radiative transfer processes produce the observed light signal within several days, weeks, and months. Thus, to learn something about the "inner workings" of Type Ia supernovae, numerical explosion modeling is needed that includes all essential steps: the explosion dynamics, the nucleosynthesis, and the radiative transfer. Only if this whole modeling chain is completed, a progenitor and explosion model can be really compared to observations. In the following, the most important explosion scenarios will be reviewed.

The fundamental property of white dwarf matter that can lead to explosive burning is the degeneracy of the electron gas. Two characteristics of highly degenerate matter are crucial here: a very low heat capacity that enables nuclear reactions to heat up the matter efficiently to high temperatures, and the fact that pressure is not coupled to temperature allowing a temperature increase without

a corresponding expansion of the matter. If by external heating or compression nuclear fusion reactions are initiated under such conditions and reach a sufficient rate, they will amplify themselves due to feedback of increasing temperature and growing (highly temperature sensitive) reaction rates. Thus, a thermonuclear runaway ensues and, potentially, an explosion of the star.

There are now several models for Type Ia supernovae that differ in the nature of the binary progenitor system, the mechanism by which accretion triggers explosive burning, and the way in which the explosion propagates through the C/O WD. The quasi-standard has so far been the *Chandrasekhar-mass model*. In this scenario, a C/O WD accretes matter from a main sequence star or a red giant companion. The explosion occurs when the WD reaches the so-called Chandrasekhar mass $M_{\rm Ch} \approx 1.4\ M_\odot$.[1] Above this mass the electron pressure can no longer compensate the gravitational forces and a collapse to a neutron star is inevitable. Shortly before reaching $M_{\rm Ch}$, however, the central density increases rapidly while the heat capacity decreases. If the central density is not too high, these conditions can lead to a thermonuclear runaway and a complete disruption of the star (thus, a collapse is avoided). The Chandrasekhar-mass model has the advantage that all explosions take place at the same total mass. Thus, the homogeneity of Type Ia supernovae is naturally explained. A drawback is, however, that WDs, which have an average mass of $\sim$0.6 $M_\odot$ when they are formed (Homeier et al. 1998), have to accrete a lot of mass to reach $M_{\rm Ch}$. The details of this process are still uncertain and population synthesis calculations predict not enough suitable progenitor systems to explain all Type Ia supernova explosions with Chandrasekhar-mass explosions (Ruiter et al. 2009). Further constraints come from X-ray observations in early-type galaxies that limit the contribution of accreting WDs reaching the Chandrasekhar mass (accreting WDs are a source of soft X-rays) to the Type Ia supernova rate in these systems to only $\sim$5% (Gilfanov & Bogdán 2010).

Within the Chandrasekhar-mass model the explosion may start either as a subsonic deflagration or a supersonic detonation. Being supersonic, detonations in contrast to deflagrations do not allow the star to expand before the burning. Thus, the matter is burnt at the initial density at the onset of the detonation, allowing for a maximum degree of processing of the nuclei. In principle, detonations in C/O WDs produce an appropriate layering of burning products to match the observed spectral evolution: mostly ^{56}Ni in nuclear statistical equilibrium at high densities ($\rho \gtrsim 10^7$ g cm^{-3}), incomplete burning to IMEs at intermediate densities, and unburnt C/O at low densities. However, *pure detonations* have the problem that in the initial hydrostatic configuration of a Chandrasekhar-mass WD only a tiny fraction of the matter ($<$0.02 $M_\odot$) is at densities $<10^7$ g cm^{-3} (see the thick upper curve in Fig. 1.1 a, which shows the density profiles in radial mass coordinate for several WDs with masses in the range 0.81–1.41 $M_\odot$). Due to this dominance of high densities, the first hydrodynamic simulation of a Type Ia supernova model, a prompt detonation of a degenerate C/O core close to the Chandrasekhar mass,

[1] This value is only valid for cold non-rotating WDs.

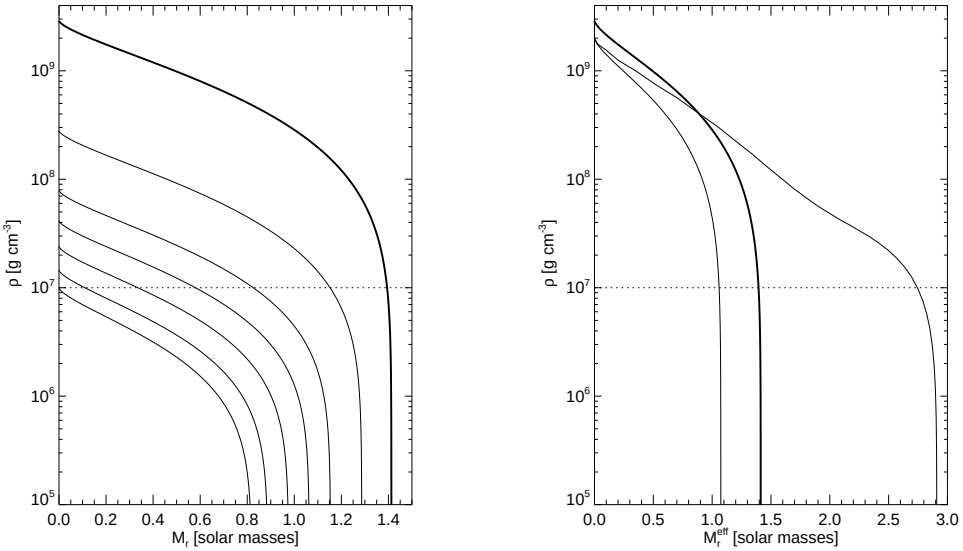

(a) no rotation (b) rapid rotation

Figure 1.1.: Hydrostatic density profiles of C/O WDs in radial mass coordinates M_r. Non-rotating WDs with masses in the range 0.81–1.41 $M_\odot$ are shown in (a). In (b) a rapidly rotating 2 $M_\odot$ WD (Model AWD3, see Table 4.1) is compared with a non-rotating Chandrasekhar-mass WD (thick curve). For the rotating model, an effective radial mass coordinate M_r^{eff} is plotted along the rotational axis (lower thin curve, $M_r^{\mathrm{eff}} = \int_0^r 4\pi z^2 \rho(z)\,\mathrm{d}z$) and perpendicular to it (upper thin curve, $M_r^{\mathrm{eff}} = \int_0^r 4\pi r'^2 \rho(r')\,\mathrm{d}r'$). In detonation burning, material above $\rho \sim 10^7\ \mathrm{g\,cm^{-3}}$ (dotted line) is converted to IGEs, whereas below, mostly IMEs are produced.

produced almost only IGEs (Ti or heavier elements, charge number $Z \geq 22$) and no significant amount of IMEs (Mg to Sc, $12 \leq Z \leq 21$) (Arnett 1969; Arnett et al. 1971). As Type Ia supernovae are believed to be a main source of metallicity, Arnett et al. (1971) already observed that this composition is in contradiction with galactic chemical evolution: the constancy of metal abundances (elements heavier than helium, $Z \geq 3$) relative to iron in stars of varying metal content (Pagel 1970) requires that a supernova model produces nearly all the elements between $6 \leq Z \leq 28$ in the proper ratios. With the identification of the prominent silicon lines and that of other IMEs in early spectra of Type Ia supernovae, the prompt detonation model could also directly be excluded.

In Type Ia supernova modeling, several ways have been proposed to avoid the total dominance of IGEs that is found in pure detonation models. The most obvious possibility is to slow down the burning and to allow for a *pre-expansion* of most of the stellar matter before it is burnt. A Chandrasekhar-mass model that explodes not in the mode of a supersonic detonation, but as subsonic *deflagration* (Nomoto et al. 1976) has the advantage of producing a significant amount of IMEs apart from the ^{56}Ni. However, this model cannot explain the whole range of observed Type Ia supernovae as it produces not enough energy for brighter explosions (Röpke et al. 2007a). More severely, the outer ejecta composition of pure deflagrations is incompatible with most observations: as the slow flame front is unstable to Rayleigh–Taylor instabilities, "fingers" of unburnt C/O are found at relatively low ejecta velocities $\sim$10 000 km s^{-1}; in observations, however, IMEs dominate above $\sim$10 000 km s^{-1}. A promising extension of the pure deflagration model is the *delayed detonation scenario*. By an assumed transition from deflagration to detonation burning at densities $\sim 10^7$ g cm^{-3} (Höflich & Khokhlov 1996), burning is accelerated and enhanced at low densities. Thus, both disadvantages of pure deflagrations can be overcome: brighter explosions are now within reach and the fingers of low velocity C/O can be supersonically burnt out by the detonation. However, the physical mechanism of a delayed detonation transition (if happening at all) is still unclear.

Another model that may also match the observations includes a departure from the Chandrasekhar-mass assumption: as illustrated in Fig. 1.1(a), a sufficient amount of IMEs may be produced in a pure detonation of a C/O WD, provided that it occurs at a total mass sufficiently below M_{Ch}. In lower mass WDs a significant fraction of material is at densities below 10^7 g cm^{-3}. Such *sub-Chandrasekhar-mass models* have the advantage of a greater frequency of potential progenitors, as less material has to be accreted, and of avoiding the need for a delayed detonation transition. However, due to the low central densities in the WD, another mechanism of triggering the explosion is needed. In the sub-Chandrasekhar scenario the ignition is assumed to occur due to the build-up and moderate heating of a degenerate shell of helium during the accretion. In analogy to classical novae, a thermonuclear runaway ensues close to the bottom of the shell, and, provided that the accreted layer is thick enough, it might turn into a detonation. In many cases (e.g., Woosley et al. 1986; Livne 1990; Woosley & Weaver 1994a; Livne & Arnett 1995) a helium

shell detonation was found to trigger a secondary detonation in the C/O core and thus a Type Ia supernova explosion. A main problem of this scenario are the IGEs that are likely produced in the helium detonation. Those are in conflict with observed early spectra that do not show high velocity IGEs, but only IMEs (Höflich & Khokhlov 1996; Nugent et al. 1997). The sub-Chandrasekhar scenario is further investigated in this thesis.

An alternative model that may also allow detonations in lower density matter is the *merger of two C/O WDs* that may occur due to emission of gravitational waves. Here, also enough material is below $\sim 10^7$ g cm^{-3}, as both WDs are below M_{Ch} and the matter in the merger is not in hydrostatic equilibrium. If the masses of both WDs are relatively equal and around $\sim 0.9\ M_\odot$, the merger was shown to be sufficiently violent to potentially trigger a detonation (Pakmor et al. 2010). If the masses are too different, however, the formation of a Chandrasekhar-mass WD of oxygen/neon composition and a gravitational collapse seem to be the most likely outcome (cf. e.g. Nomoto & Kondo 1991). The scenario of Pakmor et al. (2010) was found to be suitable to explain sub-luminous Type Ia supernovae like SN 1991bg as it produces only 0.1 $M_\odot$ of ^{56}Ni. Although the violent merger of heavier WDs could potentially produce higher ^{56}Ni masses, the progenitor systems would be to rare to explain a significant fraction of normal events.

Apart from an initial pre-expansion by deflagration burning or initially lower densities in the progenitors, a third way allowing detonations to produce more IMEs in the explosion could be *rapid differential rotation*[2] of the progenitor star when it reaches the Chandrasekhar limit. As the centrifugal force adds to the pressure force of degenerate electrons in balancing self-gravity, M_{Ch} becomes larger in the case of rapid rotation than in the static case and also depends on the applied rotation law. The area between the two thin curves in Fig. 1.1(b) illustrates the density distribution of a differentially rotating 2 $M_\odot$ WD which is close to the maximum of expected spin up (Yoon & Langer 2004; shown is Model AWD3 with parameters given in Table 4.1): rotation leads to a flattened density profile and a low density bulge in the direction perpendicular to the rotation axis. However, as seen in the figure, the mass below 10^7 g cm^{-3} is still only $\lesssim 0.1\ M_\odot$. Thus, a pure detonation of such a WD would be very bright due to the large ^{56}Ni mass, but it would most likely not produce enough IMEs. Pure deflagrations, on the other hand, have been shown to propagate extremely inefficiently perpendicular to the rotation axis of a rapidly rotating WD: in this direction, the angular momentum barrier inhibits the hydrodynamic instabilities that allow turbulent flame acceleration in non-rotating deflagration models. Thus, large fractions of the star remain unburnt and the star may not even become unbound (Pfannes et al. 2010b). Here, again the delayed detonation scenario could help out: after some pre-expansion by the deflagration, the detonation could consume the remaining unburnt fuel and, at the

[2] Only *differential* rotation, with higher angular velocities Ω in the interior than close to the surface of the WD can have significant effects here. Rigid rotation with constant Ω is restricted to relatively low values of Ω as the accretion of further matter and angular momentum is inhibited if the surface of the accreting star rotates too rapidly.

same time, produce enough IMEs. This possibility is so far unexplored, but it will be investigated as part of this work.

1.4. Objectives and organization of this thesis

All scenarios for Type Ia supernovae (except pure deflagrations) include detonations. The quality of a detonation model in the framework of global explosion simulations is therefore of crucial importance for theoretical supernova modeling. Errors in a detonation scheme due to over-simplification could easily lead to wrong conclusions about the success or the failure of a model. This work is intended to improve and analyze the capabilities of a detonation model of an existing supernova code and to study some interesting applications in Type Ia supernova models that may lead to progress in the theoretical understanding of these bright explosions; on the other hand, the shortcomings in the models may be used to figure out further improvements that are needed in the detonation scheme.

Going more into detail, this work aims at accurately and efficiently modeling the dynamics and the nucleosynthesis of detonations in the degenerate C/O and helium-rich matter of WDs. Of special importance are an accurate treatment of incomplete burning regimes and the influence of density gradients on the detonation. Also, consistency in energy release between hydrodynamic and nucleosynthesis post-processing calculations is a goal of this modeling.

The first studied application of the detonation scheme is the sub-Chandrasekhar model for Type Ia supernovae. Independent of the uncertainties of a detonation initiation in the helium shell, the impact of the nucleosynthesis in the helium detonation on spectra and light curves is of crucial importance here. In this work the influence of a multidimensional propagation of the detonation front on the detailed nucleosynthesis is studied for the first time within this scenario. In the past, the shell ejecta have always been problematic for synthetic observables. Thus, the robustness of the triggering of a secondary core detonation is explored for the lower limit of potential helium shell masses that may detonate. Investigating the influence that the helium detonation products have even in this limiting case yields important constraints on both the progenitor model and the detonation scheme.

A second application are Chandrasekhar-mass models in rapidly rotating WDs. In this context, pure detonations are tested and compared to previous simulations to probe the influence of the new detonation model. As these simulations confirm the previous problems of pure detonation models (too few IMEs at too high velocities), it is investigated whether pre-expansion by the initial deflagration phase in delayed detonation simulations can alleviate these shortcomings.

The outline of this thesis is as follows: Chapter 2 first gives an introduction into detonation theory and summarizes results of microscopical simulations of detonations in degenerate C/O and helium. Then, the simplified numerical model for detonations of this work is explained and its suitability for modeling Type Ia supernovae is analyzed on the basis of the reviewed theory.

The remainder of the thesis focuses on applications of the detonation scheme: Chapter 3 first reviews the sub-Chandrasekhar scenario, and then presents and discusses results of two-dimensional hydrodynamic double-detonation simulations with minimum helium-shell masses, including the robustness of the secondary explosion, the nucleosynthesis, and the synthetic observables. Moreover, delayed detonations in rapidly rotating WDs are explored (Chap. 4). After a short introduction into the scenario and a review of previous results, the setup of the three-dimensional hydrodynamic simulations is explained. Then, results of pure and delayed detonation simulations are presented and discussed. Chapter 5 summarizes the main results of this thesis and discusses implications on Type Ia supernova theory. Finally, possible directions for future work are suggested.

2. Modeling detonations

In this chapter, the basic concepts of detonation theory are introduced and, in this framework, the current knowledge of the microscopical properties of detonations in degenerate C/O and helium is reviewed (Sects. 2.1–2.3). This introduction into theory forms the basis for understanding the way of modeling detonations in full-star simulations in this work (see Sect. 2.4) and also the potential shortcomings. The main contribution of this work to improving detonation modeling is a method for calibrating the existing detonation scheme with a large nuclear network to ensure an accurate energy release and nucleosynthesis in incomplete burning regimes of C/O and helium detonations at low densities. This calibration is described in Sect. 2.5 and the suitability of the resulting detonation schemes for modeling Type Ia supernovae is analyzed.

2.1. The governing equations

Before discussing detonations in detail, some theoretical basics are described and relations needed later are given. First, the governing equations of reactive hydrodynamics are presented; then, they are brought to a form which is more suitable for detonation theory. Finally, shock waves, which are discontinuous solutions of these equations and essential for detonations, are introduced.

2.1.1. The reactive Euler equations

For fluids, the governing equations of explosive nuclear burning are the reactive hydrodynamic equations.[1] In the inviscid case, which is assumed here for simplicity, these are the *reactive Euler equations*:

$$\frac{\mathrm{D}\rho}{\mathrm{D}t} + \rho \boldsymbol{\nabla} \cdot \boldsymbol{u} = 0, \tag{2.1}$$

$$\frac{\mathrm{D}\boldsymbol{u}}{\mathrm{D}t} + V \boldsymbol{\nabla} p = 0, \tag{2.2}$$

$$\frac{\mathrm{D}\varepsilon}{\mathrm{D}t} + p \frac{\mathrm{D}V}{\mathrm{D}t} = 0, \tag{2.3}$$

$$\frac{\mathrm{D}\lambda_j}{\mathrm{D}t} = r_j, \quad j = 1, \ldots, N. \tag{2.4}$$

[1] The review of the basic properties of detonations in Sects. 2.1 and 2.2, mostly follows Fickett & Davis (1979).

The first three equations express the conservation of mass, momentum, and energy for the fluid, while (2.4) describes the progress of all reactions taking place. The quantities ρ, $V = \rho^{-1}$, $\boldsymbol{u}$, p, and ε are the fluid density, specific volume (volume per unit mass), velocity, pressure, and specific internal energy, respectively. Along the path of fluid elements the total time derivative takes the following form:

$$\frac{\mathrm{D}f}{\mathrm{D}t} = \frac{\partial f}{\partial t} + (\boldsymbol{u} \cdot \boldsymbol{\nabla})\, f, \tag{2.5}$$

with $f = f(x, y, z, t)$ being a function of position and time, as are all dependent variables in the reactive Euler equations. This derivative is also called the *substantial derivative*. The reactions powering the detonation are in general not evolving independently. For a simplified theoretical discussion, all reactions are represented here by an independent set of N formal reactions with progress variables λ_j, which evolve from an initial value of 0 to a final equilibrium value $\lambda_j^{\text{equil.}}$ at a formal rate r_j. In terms of the progress variables, the mass fractions of all species, X_i, can be expressed as

$$X_i = X_i^0 + \sum_{j=1}^{N} \nu_{ji} \lambda_i, \tag{2.6}$$

with ν_{ji} being the stoichiometric coefficients of the reactions and $X_i^0 = X_i(t = 0)$.

For the remaining discussion, it is sufficient to consider only the special case of one-dimensional (planar) flow and a single reaction with a progress variable λ evolving from 0 to 1 at a reaction rate r. Now, the reactive Euler equations take the form:

$$\frac{\mathrm{D}\rho}{\mathrm{D}t} + \rho \frac{\partial u}{\partial x} = 0, \tag{2.7}$$

$$\frac{\mathrm{D}u}{\mathrm{D}t} + V \frac{\partial p}{\partial x} = 0, \tag{2.8}$$

$$\frac{\mathrm{D}\varepsilon}{\mathrm{D}t} + p \frac{\mathrm{D}V}{\mathrm{D}t} = 0, \tag{2.9}$$

$$\frac{\mathrm{D}\lambda}{\mathrm{D}t} = r. \tag{2.10}$$

To close the system of equations, the equation of state and the reaction rate law have to be provided in the following form:

$$\varepsilon = \varepsilon(p, V, \lambda), \tag{2.11}$$

$$r = r(p, V, \lambda). \tag{2.12}$$

2.1.2. Relating changes in p, ρ, and λ

For the discussion below, a few more relations are needed. The differential relation for the equation of state,

$$\mathrm{d}\varepsilon = \left(\frac{\partial \varepsilon}{\partial p}\right)_{V,\lambda} \mathrm{d}p + \left(\frac{\partial \varepsilon}{\partial V}\right)_{p,\lambda} \mathrm{d}V + \left(\frac{\partial \varepsilon}{\partial \lambda}\right)_{p,V} \mathrm{d}\lambda,$$

can be used to eliminate $\frac{\mathrm{D}\varepsilon}{\mathrm{D}t}$ from (2.9). This yields a relation between the changes of p, ρ, and λ in a fluid element:

$$\frac{\mathrm{D}p}{\mathrm{D}t} = -\rho^2 c_\mathrm{f}^2 \frac{\mathrm{D}V}{\mathrm{D}t} + \rho c_\mathrm{f}^2 \frac{\mathrm{D}\lambda}{\mathrm{D}t} = c_\mathrm{f}^2 \frac{\mathrm{D}\rho}{\mathrm{D}t} + \rho c_\mathrm{f}^2 \sigma r, \tag{2.13}$$

where the velocity c_f and the dimensionless coefficient σ are defined by

$$c_\mathrm{f}^2 \equiv V^2 \frac{p + \left(\frac{\partial \varepsilon}{\partial V}\right)_{p,\lambda}}{\left(\frac{\partial \varepsilon}{\partial p}\right)_{V,\lambda}} = \left(\frac{\partial p}{\partial \rho}\right)_{s,\lambda}, \tag{2.14}$$

$$\sigma \equiv \frac{1}{\rho c_\mathrm{f}^2} \left(\frac{\partial p}{\partial \lambda}\right)_{\varepsilon,V}. \tag{2.15}$$

For a non-reactive medium, the sound speed c is the speed at which small perturbations in the state variables propagate away from the point of their creation. For an ideal fluid, c is given by

$$c = \sqrt{\left(\frac{\partial p}{\partial \rho}\right)_s} = \sqrt{\gamma \left(\frac{\partial p}{\partial \rho}\right)_T}, \tag{2.16}$$

with s being the specific entropy and $\gamma = c_p/c_V$ being the ratio of the specific heats at constant pressure and at constant volume. In the case of a reactive medium with reactions taking place on a time scale τ, a dispersion of the velocity of sound occurs. High-frequency perturbations with frequencies $\nu \gg \tau^{-1}$ propagate with the *frozen sound speed* c_f that is evaluated at constant λ (Eq. 2.14; "frozen" refers to the fixed composition). For low-frequency perturbations with $\nu \ll \tau^{-1}$, λ will vary, as the reaction equilibrium will follow the changes in the state variables. This results in a propagation with the lower *equilibrium sound speed* $c_\mathrm{e} < c_\mathrm{f}$.

The last term in (2.13), $\rho c_\mathrm{f}^2 \sigma r$, quantifies the deviation of the evolution in p–ρ space due to reactions. For a positive value of σr (called *thermicity* or *thermicity product*), the pressure change for a given change in the density is larger than it would be without reactions ($r = 0$). The thermicity is a measure for the rate at which energy released by the reaction is transformed to thermal and kinetic energy of the flow.

2.1.3. Shock waves

The differential form of the Euler equations (2.1)–(2.3) allows only continuous solutions. In the more general integral form of the equations, however, discontinuous solutions (also called *weak solutions*) are possible. Across a discontinuity surface, several state variables may have jumps. An important class of weak solutions are *shock waves* in which both the pressure p and the density ρ jump at the so-called shock front. To ensure the conservation of mass, momentum, and energy at the front, the integral form of the hydrodynamic equations can be applied to a small

volume around this surface. This yields the *Rankine–Hugoniot conditions* (see e.g. Landau & Lifschitz 1991 for the details; reactions are not considered here):

$$\rho_0 D = \rho u, \tag{2.17}$$

$$p_0 + \rho_0 D^2 = p + \rho u^2, \tag{2.18}$$

$$\varepsilon_0 + \frac{1}{2}D^2 + p_0 V_0 = \varepsilon + \frac{1}{2}u^2 + pV. \tag{2.19}$$

A shock wave moves with velocity D into matter which is at rest. The above equations are, however, written in the shock frame: unshocked matter streams in with velocity $u_0 = D$ and the shocked material flows out at velocity u relative to the front (in the frame of the initial state, u would have to be replaced by $D - u$). Quantities with index 0 refer to the state before the shock (upstream), whereas quantities without an index refer to the state after the shock (downstream). If ρ_0, p_0, and D are given, the shocked state ρ, p, u can be uniquely determined. This becomes obvious when rearranging the equations:

$$-\rho_0^2 D^2 = \frac{p - p_0}{V - V_0}, \tag{2.20}$$

$$\varepsilon_0 - \varepsilon + \frac{1}{2}(V_0 - V)(p_0 + p) = 0, \tag{2.21}$$

$$(D - u)^2 = (p - p_0)(V_0 - V). \tag{2.22}$$

Equations (2.20) and (2.21) both describe curves in the p–V plane, termed the *Rayleigh line* $\mathcal{R}$ and the *shock* or *Hugoniot adiabat* $\mathcal{H}$, respectively (see Fig. 2.1). These curves have the common starting point (p_0, V_0). The Rayleigh line $\mathcal{R}$ contains all possible final states for which mass and momentum conservation hold (if the downstream velocity is calculated from Eq. 2.22). According to (2.20), the slope of $\mathcal{R}$ is determined by the shock speed D: for larger values of D, $\mathcal{R}$ declines steeper. Given the equation of state, $\varepsilon = \varepsilon(p, V)$, the Hugoniot adiabat $\mathcal{H}$ contains all final states for which the energy is conserved. The second point of intersection of $\mathcal{R}$ and $\mathcal{H}$ apart from the starting point (p_0, V_0) is the unique post-shock state. For almost all known equations of state, the adiabatic compressibility $-(\partial V/\partial p)_s$ decreases with increasing pressure:

$$\left(\frac{\partial^2 V}{\partial p^2}\right)_s > 0. \tag{2.23}$$

If this condition holds, it can be shown with a stability analysis (see Landau & Lifschitz 1991) that (p, V) has to lie on the upper branch of $\mathcal{H}$. Thus, a shock wave compresses the matter behind it:

$$\rho > \rho_0,\ p > p_0. \tag{2.24}$$

Furthermore, independent of the equation of state

$$D > c_0,\ u < c \tag{2.25}$$

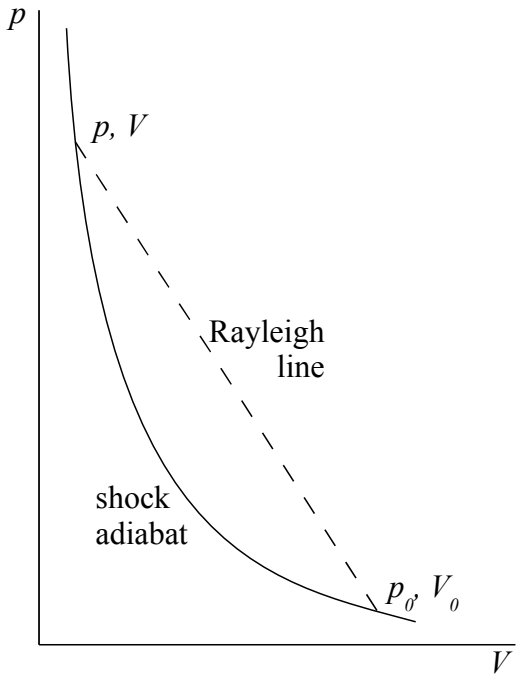

Figure 2.1.: A shock wave in the p–V plane.

holds. This means that shock fronts propagate *supersonically* into the upstream medium, but are *subsonic* with respect to the downstream state. Consequently, a shock wave cannot influence the state ahead of it, as small perturbations occurring at the front propagate slower than the front itself. But, perturbations from behind might disturb the shock front.

2.2. The structure of detonations

Having the governing equations of explosive burning in fluids at hand, now, the nature of detonations can be explained. In a detonation wave, the burning spreads by a shock wave that compresses and heats the matter behind it sufficiently to ignite it. Real detonations have a complex multidimensional structure, however, on average they can be described relatively well by one-dimensional theories. Therefore, the ZND theory of planar detonations powered by a simple exothermic reaction is outlined first (Sect. 2.2.1). Afterwards, a more realistic theory that includes more complex reactions and multidimensional effects is qualitatively explained (Sect. 2.2.2). Based on the theoretical background, finally, the structure of detonations in degenerate C/O and helium, which is relevant for Type Ia supernova models, is described by briefly reviewing previous numerical studies.

2.2.1. The ZND theory

To explain the various complex properties of real detonations, it is important to first outline the basic concept. The *Zel'dovich–von Neumann–Doering* or *ZND model* has been developed in the early 1940s and is described here following Fickett & Davis (1979). It is valid for planar detonations with simple monotonic exothermic reactions.

Basic assumptions

The ZND theory is based on the following simplifying assumptions:

1. The detonation wave is planar and can therefore be described by one-dimensional equations.
2. All transport effects such as heat conduction, radiation, diffusion, and viscosity can be neglected. Hence, the leading shock is a discontinuous jump.
3. There is only one irreversible reaction with a monotonic heat release.
4. All thermodynamic variables apart from the abundances of the species involved in the reaction are in thermodynamic equilibrium everywhere.

Steady structure

If these assumptions are valid, the one-dimensional reactive Euler equations (2.7)–(2.12) and the Rankine–Hugoniot jump conditions (2.20)–(2.22) are appropriate to describe the continuous flow and the leading shock wave, respectively. For a constant initial state, a steady (time-independent) solution exists for the detonation wave in the frame of the shock. The basic structure of a planar detonation wave is shown schematically in Fig. 2.2(a) giving the pressure p as a function of the spatial coordinate x in propagation direction. First, the unburnt matter on the right is compressed by the leading shock, causing a jump in p. Then, the burning sets in and completes within a certain region behind the shock—the *reaction zone*. The length of this zone defines the *detonation width* and the point marking its end is termed *final state*. The final state and the flow upstream of it are time-independent, whereas the downstream structure is in general time-dependent. In the ZND theory, the flow downstream of the final state can have two different structures depending on the rear boundary conditions (see Fig. 2.2): in the unsupported case (a) a time-dependent rarefaction wave follows the final state; in the overdriven case (b), where the detonation is supported by a driving piston, the following flow is a time-independent constant state. Importantly, the rear boundary conditions also influence the detonation speed D at which the shock moves into the unburnt initial state (see Sect. "Dependence on the rear boundary conditions" on page 26).

For now, the value of D and with it the strength of the shock are assumed to be known (D can also be treated as a parameter). Given D, the structure of the

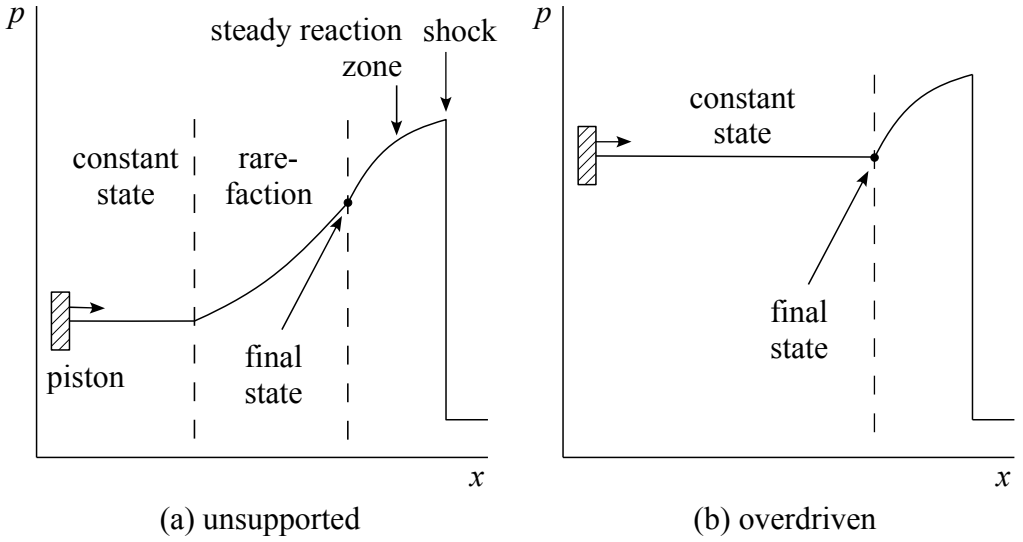

Figure 2.2.: Schematic detonation structure: (a) unsupported case, (b) supported or overdriven case.

steady reaction zone is determined by the equations of motion. Dropping the time derivatives in (2.7)–(2.10) leads to the following system of ordinary differential equations:

$$u\frac{\mathrm{d}\rho}{\mathrm{d}x} + \rho\frac{\mathrm{d}u}{\mathrm{d}x} = 0, \tag{2.26}$$

$$\rho u\frac{\mathrm{d}u}{\mathrm{d}x} + \frac{\mathrm{d}p}{\mathrm{d}x} = 0, \tag{2.27}$$

$$u\frac{\mathrm{d}\varepsilon}{\mathrm{d}x} + pu\frac{\mathrm{d}V}{\mathrm{d}x} = 0, \tag{2.28}$$

$$u\frac{\mathrm{d}\lambda}{\mathrm{d}x} = r. \tag{2.29}$$

Here, u is the velocity in the shock frame. To eliminate the dependence on the internal energy ε, the above derived relation (2.13) is used instead of (2.28). After dropping all terms with time derivatives, it becomes:

$$u\frac{\mathrm{d}p}{\mathrm{d}x} = c_\mathrm{f}^2 u\frac{\mathrm{d}\rho}{\mathrm{d}x} + \rho c_\mathrm{f}^2 \sigma r. \tag{2.30}$$

By forming linear combinations, the system (2.26), (2.27), (2.29), and (2.30) can

be easily decoupled:

$$\frac{\mathrm{d}\rho}{\mathrm{d}x} = -\frac{\rho}{u}\frac{\sigma r}{1-u^2/c_\mathrm{f}^2} \equiv -\frac{\rho}{u}\frac{\sigma r}{\eta}, \tag{2.31}$$

$$\frac{\mathrm{d}p}{\mathrm{d}x} = -\rho u\frac{\sigma r}{\eta}, \tag{2.32}$$

$$\frac{\mathrm{d}u}{\mathrm{d}x} = \frac{\sigma r}{\eta}, \tag{2.33}$$

$$\frac{\mathrm{d}\lambda}{\mathrm{d}x} = \frac{r}{u}. \tag{2.34}$$

The *sonic parameter* $\eta = 1 - u^2/c_\mathrm{f}^2 \equiv 1 - \mathrm{Ma}^2$, with Ma being the Mach number, changes from a positive to a negative sign if the flow becomes supersonic.

Given the constant upstream state ρ_0, p_0, $\lambda_0 = 0$, and $u_0 = D$ (at $x < 0$), the shocked state ρ, p, λ, and u (at $x = 0$) can be determined from the Rankine–Hugoniot conditions (2.20)–(2.22) (λ stays zero, as the reactions only start with some delay after the shock). Now, (2.31)–(2.34) can be integrated to determine the whole steady reaction zone structure at $x > 0$. Instead of integrating (2.33), the velocity u can be directly calculated from the density and the pressure by evaluating (2.22). Note that if the state variables ρ, p, and λ are known at x, the rate $r = r[p(x), \rho(x), \lambda(x)]$ and the quantities c_f and σ that depend on the equation of state $\varepsilon = \varepsilon[p(x), \rho(x), \lambda(x)]$ are all given.

The discontinuity approximation

When deriving the Rankine–Hugoniot conditions (2.20)–(2.22), the volume of integration can in principle be arbitrarily extended. Therefore, they are valid to be applied to any two states of a one-dimensional flow and express that nothing is lost in the flow in between. Given the detonation velocity D and the final value of the progress variable ($\lambda = 1$, for the simple monotonic reaction considered here), the final state of the detonation can thus be directly determined from the Rankine–Hugoniot conditions. This state does not depend on any of the intermediate states in the reaction zone.

As the solution of the reaction zone is stationary and its width is often negligible when compared with the characteristic length scales of the global problem (like a supernova explosion), it is in many cases appropriate to assume the limit of instantaneous reaction. In this case, which is called the *Chapman–Jouguet (CJ) model* or the *discontinuity approximation*, the shock and the reaction zone visible in Fig. 2.2 are collapsed into a single jump discontinuity (Fig. 2.3 b). Thus, the detonation wave can be described as a discontinuity solution of the hydrodynamic equations similar to a shock wave, that has to fulfill the same equations for mass and momentum conservation, (2.20) and (2.22), but a modified version of the energy conservation relation (2.21): it has to be taken into account that the reaction energy q is released when passing the discontinuity and that, due to the change in

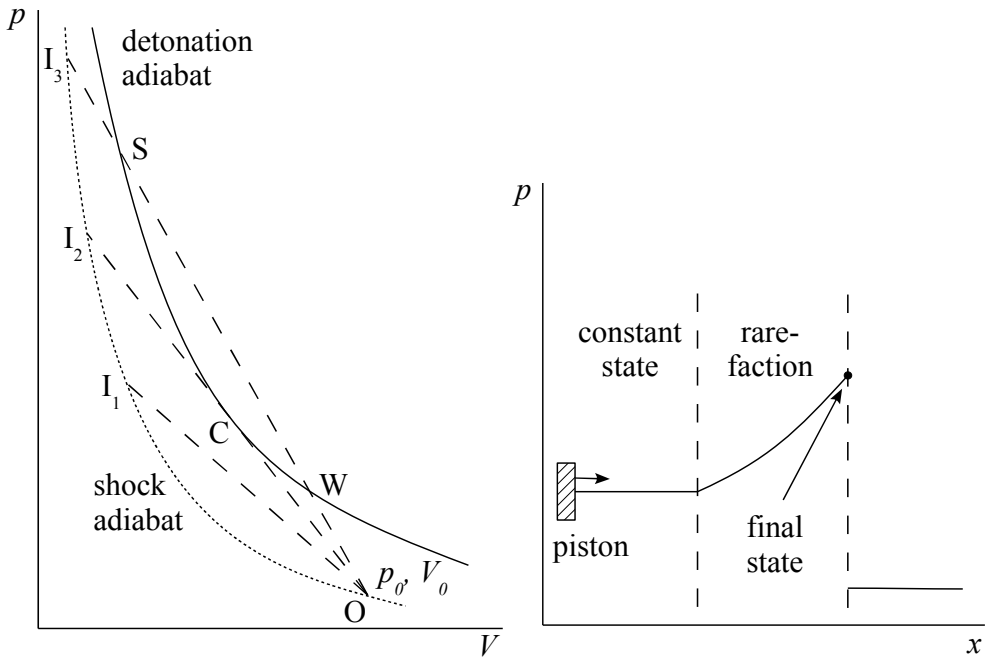

Figure 2.3.: Structure of a detonation wave in the limit of instantaneous reaction (the discontinuity approximation): (a) structure in the p–V plane, (b) spatial structure.

composition, the equation of state of the matter is modified (this is accounted for by the λ dependence of $\varepsilon = \varepsilon(p, V, \lambda)$):

$$\varepsilon_0 + q - \varepsilon + \frac{1}{2}(V_0 - V)(p_0 + p) = 0. \tag{2.35}$$

For nuclear reactions, the energy release, or *q-value*, is defined as the change in the mean specific binding energy $\bar{\varepsilon}_\mathrm{b}$:

$$q = \bar{\varepsilon}_{\mathrm{b},0} - \bar{\varepsilon}_\mathrm{b}, \tag{2.36}$$

$$\bar{\varepsilon}_\mathrm{b} = \sum_k \varepsilon_{\mathrm{b},k} X_k, \tag{2.37}$$

with $\varepsilon_{\mathrm{b},k}$ being the specific binding energy of a nucleus k with mass fraction X_k.

When plotting the detonation in the p–V plane (Fig. 2.3 a) there are significant changes compared to shock discontinuities (Fig. 2.1) due to the reaction: the Hugoniot adiabat shifts to higher pressures due to the energy release of the burning and due to the changes in composition its shape may also differ. All points on this *detonation adiabat* $\mathcal{H}_\mathrm{D}$ are potential final states of the detonation wave. The

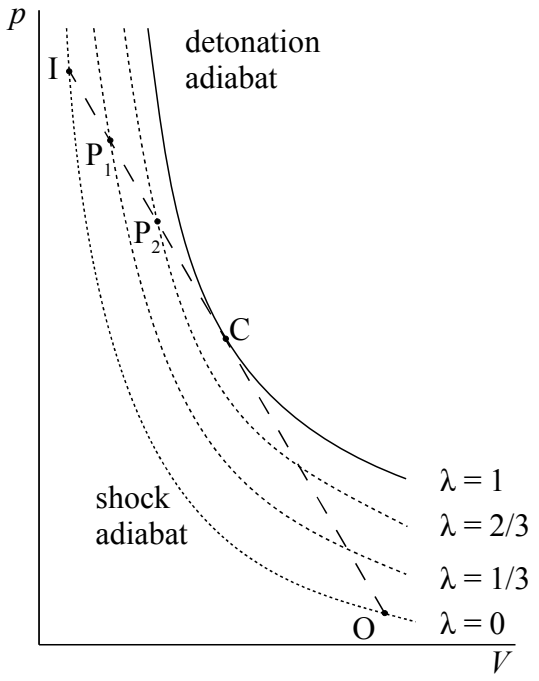

Figure 2.4.: Partial reaction adiabats of a detonation in the p–V plane.

solution is determined by the intersection with the Rayleigh line $\mathcal{R}$. The slope of $\mathcal{R}$ depends on the detonation speed D: OI_1, OI_2, and OI_3 in Fig. 2.3 are three examples for increasing values of D with 0, 1, and 2 possible solutions for the final state, respectively. The significance of these cases is explained below after the discussion of more properties of the p–V evolution.

Partial reaction adiabats

Going back to the more general ZND theory, the jump conditions for the discontinuity approximation are still valid and link the upstream with the final state variables. However, one can additionally define *partial reaction adiabats* in between the shock adiabat $\mathcal{H}$ and the detonation adiabat $\mathcal{H}_\mathrm{D}$ that link the upstream variables with that of the intermediate states of the reaction zone when intersected with the Rayleigh line $\mathcal{R}$ (see Fig. 2.4). Here, λ and $q(\lambda)$ of the partially burnt state have to be used in (2.35). As a monotonic heat release of the reaction is assumed, going from $\lambda = 0$ to $\lambda = 1$ will produce a continuous series from $\mathcal{H}$ to $\mathcal{H}_\mathrm{D}$. This resembles the steady solution structure seen in Fig. 2.2(a): from the constant initial state O the shock drives the system to point I. Then, the reactions set in and, while the energy is released, the system evolves down $\mathcal{R}$ towards lower pressure crossing the partial reaction adiabats for $\lambda = 1/3$ and $\lambda = 2/3$ in the points P_1 and P_2 and eventually reaches the final state in point C with $\lambda = 1$. There, all reactions cease.

The Rayleigh line must never be left, as mass and momentum must be conserved for all intermediate states.

The detonation speed

Now, the possible values of the detonation speed D are discussed. As detonations are shock-driven, the leading shock must fulfill (2.25) and propagates supersonically into the unburnt matter. Depending on D, the number of solutions for the final state of the detonation varies (see the three Rayleigh lines $\mathcal{R}$ in Fig. 2.3 a):

- For $D < D_{\min}$, $\mathcal{R}$ does not intersect the detonation adiabat $\mathcal{H}_{\mathrm{D}}$, thus, no solutions for the final state do exist.
- For $D = D_{\min} \equiv D_{\mathrm{CJ}}$, $\mathcal{R}$ is tangential to $\mathcal{H}_{\mathrm{D}}$. There is one unique solution for the final state. This case is called *Chapman–Jouguet detonation*. A detonation of this type propagates at minimum speed D_{CJ} into the unburnt medium (point C).
- For faster propagating detonations, $D > D_{\min}$, which can occur in the overdriven case, there are two potential solutions (points S and W): one *strong branch* solution at a higher pressure than in the Chapman–Jouguet case, and one *weak branch* solution at a lower pressure than in the Chapman–Jouguet case.

The Chapman–Jouguet case is very important, as it is often realized for detonations that are formed and supported only by the burning itself. Here, the velocity profile in the reaction zone has the following properties: according to (2.25), the state directly behind the shock is subsonic with respect to the front ($u < c$). Following the Rayleigh line in Fig. 2.3(a) from I_2 to C, the reactions proceed while the pressure decreases. Eliminating the volume dependency from (2.20) and (2.22) yields:

$$u = D - \frac{V_0}{D}(p - p_0). \tag{2.38}$$

Thus, along $\mathrm{I}_2\mathrm{C}$ with decreasing pressure, the downstream flow velocity with respect to the front increases. It can be shown that for the Chapman–Jouguet point the velocity reaches exactly the sonic value (see Landau & Lifschitz 1991):

$$u_{\mathrm{CJ}} = c_{\mathrm{f}}. \tag{2.39}$$

In other words, there is a *sonic point* at the end of the reaction zone of a Chapman–Jouguet detonation, while the rest of the reaction zone is subsonic. Hence, the whole reaction zone is in sonic contact with the front and can power the leading shock. Points behind the sonic point cannot power or disturb the front.

Assuming again (2.23), it can be shown that for final states on the detonation adiabat $\mathcal{H}_{\mathrm{D}}$

$$\frac{\mathrm{d}}{\mathrm{d}p}\left(\frac{u}{c_{\mathrm{f}}}\right) < 0 \tag{2.40}$$

holds (see Landau & Lifschitz 1991). Therefore, final states on the strong branch above C are subsonic and final states on the weak branch below C are supersonic with respect to the front.

In the case of strong branch solutions, the whole reaction zone is subsonic and contains no sonic point. Like in the Chapman–Jouguet case, all parts of the reaction zone can thus power the leading shock. However, disturbances from behind the reaction zone can now also reach the shock. Concerning their stability properties, strong detonation fronts therefore differ significantly from those of the Chapman–Jouguet case.

With their supersonic final states, weak detonation fronts cannot be reached by disturbances from behind. However, within the assumptions of the ZND theory weak branch solutions cannot be realized: during the burning the state has to evolve along the Rayleigh line $\mathcal{R}$ starting e.g. from point I_3 in Fig. 2.3(a) until the final state is reached. To reach the weak final state W, however, the segment SW would have to be passed. Due to (2.24), a shock wave from the higher density state S to the lower density state W is impossible. Thus, the segment SW could only be passed by appropriate chemical or nuclear reactions. The segment, however, corresponds to partial reaction adiabats at higher energies than available by the assumed simple reaction and thus cannot be crossed. Therefore, weak detonations are not possible within the ZND theory. However, in Sect. 2.2.2 below, it will be shown that complex reactions with non-monotonic heat release can really allow for reaching the weak branch.

Dependence on the rear boundary conditions

Whether a ZND detonation is of Chapman–Jouguet type propagating at the minimum speed D_{CJ} or if it is of the strong type propagating at a faster speed $D > D_{\mathrm{CJ}}$ is determined by the rear boundary conditions:

- *Unsupported* case (see Fig. 2.2 a): there is no driving piston behind the burning front and the reaction zone, or in general, the speed of a driving piston is less than the speed of the final state of the reaction zone. Here, the detonation is of the Chapman–Jouguet type, $D = D_{\mathrm{CJ}}$, and the steady reaction zone is followed by a time-dependent rarefaction wave slowing down the matter from the speed of the final state to that of the driving piston (or to zero).

- *Supported* case (see Fig. 2.2 b): the driving piston is faster than the final state velocity of the Chapman–Jouguet detonation. The detonation is strong or *overdriven*, $D > D_{\mathrm{CJ}}$ (with D/D_{CJ} being the *overdrive factor*). The overdrive factor adjusts such that the final state velocity of the reaction zone matches that of the driving piston (from Eq. 2.40, it can be seen that the final state velocity $D - u$ in the laboratory frame is faster for strong branch solutions than for the Chapman–Jouguet case). This leads to a continuum of possible detonation velocities above D_{CJ}. As a consequence of the larger

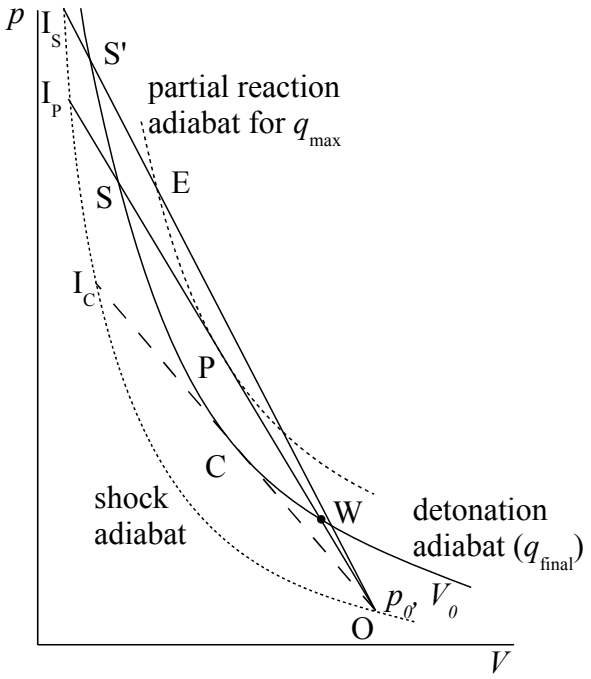

Figure 2.5.: Structure of a pathological detonation in the p–V plane.

detonation speed, overdriven detonations have a stronger leading shock and a shorter reaction zone length than Chapman–Jouguet detonations. Behind the reaction zone there is no rarefaction wave, but only a constant state due to the equal velocities of the final state and the piston.

2.2.2. More realistic theory

Effects that allow weak detonations

Departing from the simplifying assumptions of the ZND theory in most cases opens up a path to reach weak branch solutions. As a first example, *non-monotonic heat release* is discussed. Consider an exothermic reaction that is accompanied by a much slower endothermic reaction: the q-value monotonically increases from zero, reaches a maximum value $q_{\max}$, and then monotonically drops to the final value $q_{\text{final}} < q_{\max}$. Continuing the above discussion, now the segment SW can be crossed by the reaction (see Fig. 2.5): first the shock leads from point O to point I_P, then, the exothermic reaction takes place in between the points I_P and P. At P the maximum energy release $q_{\max}$ is reached. Finally, the endothermic reaction leads the system from point P to the weak branch solution point W that corresponds to the total energy release q_{final}. The Rayleigh line $\mathcal{R}$ along which the detonation takes place, OI_P, has to be tangent to the partial reaction adiabat

representing $q = q_{\max}$. If $\mathcal{R}$ was not tangent and there was an intersection, e.g. along $\mathrm{OI_S}$, this would lead the system to states with higher energy release than $q_{\max}$ on the way to the weak branch, in contradiction to the assumptions. Thus, $\mathcal{R}$ cannot decline steeper than $\mathrm{OI_P}$ and the detonation velocity cannot be higher than the value corresponding to the point P ($D = D_{\mathrm{P}}$). On the other hand, D can also not be smaller, as $q_{\max}$ would not be reached in that case. The value of D is therefore uniquely determined. It depends on details of the reaction like $q_{\max}$ and the shape of the according partial detonation adiabat and thus also on the equation of state of the matter in this partial reaction state. Therefore, one really has to integrate the equations of the reaction zone structure using detailed reaction rates of all reactions to determine D and the final state. This is not the case for Chapman–Jouguet detonations. There, the final state and D can be determined independent of the reaction zone structure and only the final q-value and composition are needed (which are known in advance in many cases).

The weak branch solution of the detonation problem corresponding to the path in the p–V diagram that was just discussed is termed *eigenvalue detonation* or *pathological detonation* and P is called *pathological point*. In P not only the sign of the energy release changes, but P has to be also a sonic point relative to the detonation front. This becomes clear as P is the analog to the Chapman–Jouguet point C with $\mathcal{R}$ being tangential to $\mathcal{H}_{\mathrm{D}}$ if one considers only the initial monotonic exothermic reaction part and assumes the reactions to stop there. If the reaction proceeds beyond P, the pressure decreases further and, due to (2.38), the velocity u in the shock frame becomes supersonic. Thus, the part of the reaction zone behind the sonic point P is not in sonic contact with the front and cannot contribute to driving the detonation (only the energy released between $\mathrm{I_P}$ and P can drive the leading shock). Hence, it becomes physically clear why internal details of the reaction zone are import for determining the detonation speed in the weak branch solution case: only the q-value of an intermediate reaction state powers the detonation propagation. For a numerical simulation to realistically describe such a detonation, it is therefore essential to spatially resolve the reaction length scales of the leading reaction parts that are in sonic contact with the flame.

Now, conditions under which weak branch solutions become possible are discussed in general. To this end, the p–V evolution according to the equations for the steady reaction zone, (2.31)–(2.34) is analyzed. The evolution crucially depends on the sign of the term $\frac{\sigma r}{\eta}$, where σr is the thermicity product, which is sometimes also denoted as ϕ (see Sect. 2.1.2), and η is the sonic parameter $\eta = 1 - u^2/c_{\mathrm{f}}^2$. According to (2.31) and (2.32), the system state moves down $\mathcal{R}$ if $\frac{\sigma r}{\eta} > 0$ and up if $\frac{\sigma r}{\eta} < 0$. Due to (2.25), the flow is always subsonic ($\eta > 0$) directly behind the shock (e.g. points $\mathrm{I_P}$ and $\mathrm{I_S}$ in Fig. 2.5) in the frame co-moving with the front. Therefore, the state moves down $\mathcal{R}$ for $\sigma r > 0$ (e.g. for an exothermic reaction) and up for $\sigma r < 0$ (e.g. for an endothermic reaction). Due to (2.38), u increases and thus η decreases for a system moving down $\mathcal{R}$. If η becomes zero at a critical

sonic point x_c, i.e.,

$$u(x_c) = c_f(x_c), \tag{2.41}$$

a singularity occurs in the equations of the reaction zone. A necessary condition for the derivatives in (2.31)–(2.33) to remain finite and thus for the continuation of the solution is:

$$\sigma(x_c)r(x_c) = 0. \tag{2.42}$$

For the case of the pathological detonation above ($\mathcal{R} = \mathrm{OI_P}$), both (2.41) and (2.42) hold in P. Therefore, the solution can be continued and, as both σr and η change sign, $\frac{\sigma r}{\eta}$ stays positive and the system proceeds downwards to the weak branch point W.

The above discussion makes clear that the evolution of the thermicity product σr determines the nature of the solution. The generalized (necessary) condition for reaching weak branch solutions is that σr has to become negative somewhere in the reaction zone. Roughly speaking, σr determines how the reactions taking place affect the flow in a reactive medium. According to Fickett & Davis (1979), a positive value of σr means a transfer of (chemical or nuclear) binding energy to the flow, and a negative value means the reverse. In general, σr is the sum of two terms, one proportional to the reaction enthalpy, and another proportional to the volume change. Hence, an *increase in specific volume* during a reaction has a similar effect as a positive heat release. On the other hand, a decrease in specific volume acts in an "endothermic" way and can lead to a negative thermicity product and thus a weak branch solution even for a single exothermic reaction. Another channel for reaching weak branch solutions opens up if *dissipative effects* like viscosity are included. In the thermicity product they also act like an endothermic reaction contribution.

To recapitulate, two of the simplifying assumptions of the ZND theory have been abandoned, namely, the monotonicity of the heat release (third assumption) and the absence of transport effects like dissipation (second assumption). In both cases weak branch solutions become possible. Now, a departure from the first assumption (a one-dimensional flow) is discussed. Again, it can be shown that weak branch solutions can be reached. Consider a detonation with a weakly *curved front*, e.g. a spherically diverging detonation at a radius that is large in comparison to the reaction length scales. By a change of coordinates, the governing reactive Euler equations can be written in a quasi-one-dimensional approximation (Yao & Stewart 1996; Sharpe 2001). This adds an additional curvature-dependent term to the thermicity product σr. For a convexly curved detonation front this term is negative and therefore analogous in its effect to a dissipative term. If this term is large enough, σr can become negative and allow for a weak branch solution with a detonation velocity that depends both on the reaction details and on the amount of curvature.

Note here also, the important influence of *overdrive*. Overdrive effects, i.e. the steepening of the detonation shock caused by a driving piston or by the presence of strong density gradients (see Sect. "Density gradients" on page 35), change the

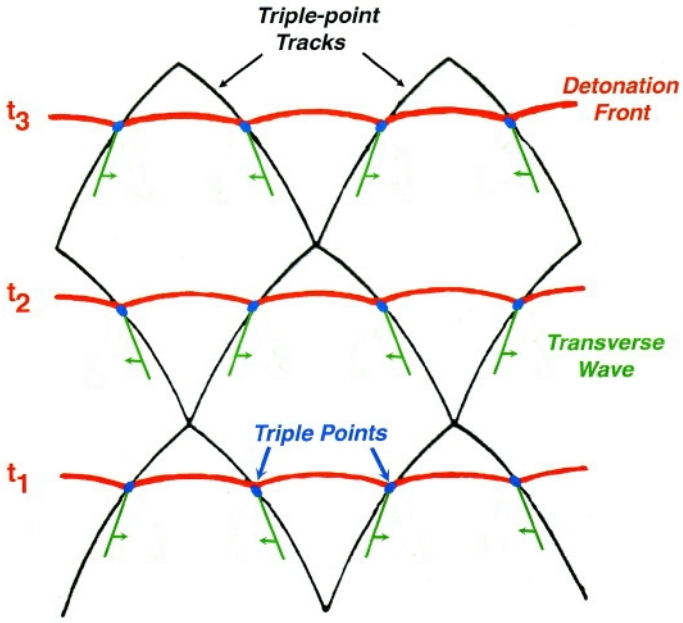

Figure 2.6.: The cellular structure of a detonation (slightly modified version of a figure from Timmes et al. 2000).

evolution in the p–V plane significantly. Initially, the evolution down $\mathcal{R} = \mathrm{OI_S}$ is similar to the unsupported case ($\mathrm{OI_P}$) until the sign of σr changes in point E. There, however, the flow is still subsonic ($\eta > 0$) and $\frac{\sigma r}{\eta}$ becomes negative. Thus, the system has to evolve again upwards $\mathcal{R}$ and *cannot reach the weak branch.* Finally, the *strong* point S′ is reached.[2]

In summary, for the realistic simulation of (quasi) one-dimensional detonations, in general, the reaction zone structure has to be integrated and the details of the reactions, dissipation effects, and curvature have to be taken into account. Both detonation speeds and final compositions are influenced by these properties.

Multidimensional effects

Real detonations are subject to instabilities that make them intrinsically three-dimensional. The (quasi) one-dimensional theory that has been discussed so far applies to the three-dimensional case only in an average sense. In reality, detonations can have a cellular structure: the structure that is shown in Fig. 2.6 arises from transverse perturbations in the reaction zone, e.g. in the density. It can be intuitively understood as the product of a series of aligned spherical micro-detonations: shock waves of adjacent detonations collide with each other and form a front that is composed of curved incident shocks (red line at time t_1) and

[2]The change of sign of σr also causes a non-monotonicity in the state variables in the reaction zone: both p and ρ pass through a minimum in E.

transverse shocks behind them (shown in green) that are periodically reflected from each other. The front and the transverse shocks intersect in so-called triple points (blue ellipses) that have a higher pressure than the rest of the front. Figure 2.6 shows three snapshots (at $t = t_1$, t_2, and t_3) of the detonation front as it moves from the bottom to the top. Over time, the triple-point trajectories, which follow the movement of the transverse shocks, form a cellular structure. A cell is closed when two transverse shocks collide. As they are reflected from each other, a new cell opens up. The distance between two transverse waves that move in the same direction is equivalent to the width of the cells. According to Sharpe (2001), the width is on the order of 10–100 reaction zone lengths of the one-dimensional steady detonation. Due to the higher compression close to the cell boundaries, for temperature-sensitive reactions the matter is more processed than near the cell centers. Accordingly, the interior parts of the cells form pockets of less processed material. Apart from this effect on the final composition, the cellular instability also influences the mean detonation speed, which is generally a bit lower than that of a corresponding planar detonation. But, according to Timmes et al. (2000), the average speed is only 1–2% lower. The slower speed is a consequence of the convex curvature of the incident shocks (between two triple points in Fig. 2.6): thus, the front surface that has to be driven by the energy released behind it is increased compared to the planar case.

2.2.3. Detonations in white dwarf matter

White dwarf stars that are suitable as progenitors of Type Ia supernovae consist of a mixture of degenerate carbon and oxygen. Potentially, an accreted shell of degenerate helium might also be involved. Therefore, in the following, the main properties of detonations in both degenerate C/O mixtures and degenerate helium that have so far been published are described. First, the the C/O case is considered, then the helium case.

C/O detonations

Planar detonation structure In detonation waves in degenerate C/O matter, the reactions take place in three distinct layers. First, *carbon burning* takes place on a time scale much shorter than that of the succeeding reactions. This is followed by a much more extended layer of *oxygen burning* (also called nuclear statistical quasi-equilibrium relaxation). In this burning phase intermediate mass elements (IMEs) are produced, of which ^{28}Si is the most abundant nucleus. Finally, *silicon burning* (or nuclear statistical equilibrium relaxation) occurs. On much longer time and length scales than in the oxygen burning case, nuclear statistical equilibrium (NSE) is established there, producing iron group elements (IGEs). In NSE, which occurs at sufficiently high densities and temperatures, all strong reactions are in balance and the abundances are not determined by reaction rates, but by the binding energies of the nuclei and the local thermodynamic state. In summary, for

the structure of reactions in C/O detonations

$$l_{\mathrm{C}} \ll l_{\mathrm{O}} \ll l_{\mathrm{Si}} \tag{2.43}$$

holds (Khokhlov 1989), where l_i denotes the length scale of a burning phase i.

Now, the energy release of the different phases is considered. Both carbon and oxygen burning are exothermic at all upstream densities, and silicon burning is also exothermic at low densities. In NSE, however, the mean binding energy of matter becomes lower with increasing temperature due to photo-disintegration reactions. Thus, above some density $\rho_{\mathrm{endoth.}} \sim 2 \times 10^7\ \mathrm{g\,cm^{-3}}$, silicon burning becomes endothermic (Imshennik & Khokhlov 1984; Khokhlov 1989; Gamezo et al. 1999; Sharpe 1999) and the overall energy release becomes *non-monotonic*. At higher densities, self-sustained detonations are therefore no longer of Chapman–Jouguet, but of *pathological* type (see Sect. 2.2.2). Thus, they have a propagation velocity $D_{\mathrm{P}} > D_{\mathrm{CJ}}$, a sonic point in the reaction zone (where the sign of $\frac{\mathrm{d}q}{\mathrm{d}x}$ changes), and a supersonic final state.

Imshennik & Khokhlov (1984) and Khokhlov (1988) have calculated the structure and parameters of steady planar Chapman–Jouguet detonations in degenerate C/O matter, whereas Khokhlov (1989) additionally investigated the consequences of the silicon reaction becoming endothermic. Khokhlov (1989) determined the structure of overdriven detonations in that regime and the subsonic part of the reaction zone of the self-sustained, pathological case. However, he could not determine the supersonic part of the reaction zone in that case, due to problems with the integration beyond the singularity that corresponds to the sonic point. The whole structure was then calculated by Sharpe (1999) by carefully analyzing the nature of the solutions near the sonic point.

According to Fig. 2.7 that has been taken from Gamezo et al. (1999), above $\rho \sim 10^8\ \mathrm{g\,cm^{-3}}$, D_{P} is ∼3–4% greater than D_{CJ}. The reason for this is a larger effective q-value that drives the detonation in the pathological case as shown in the figure. In the pathological regime of C/O detonations above $\rho_{\mathrm{endoth.}} \sim 2 \times 10^7\ \mathrm{g\,cm^{-3}}$, the final endothermic parts of silicon burning are not in sonic contact with the front and thus a more energetic intermediate reaction state corresponding to $q_{\mathrm{P}} > q_{\mathrm{CJ}}$ determines the detonation speed.

Overdrive strongly influences the structure and final composition of a detonation wave above $\rho_{\mathrm{endoth.}}$: the detonation lengths for overdriven C/O detonations found by Sharpe (1999) are a few times shorter than their self-sustained counterparts. This means that for self-sustained detonations the transition to incomplete burning that is discussed below occurs at higher densities than for the corresponding overdriven cases. Additionally, there are differences in the final composition: overdriven detonations have hotter and denser final states than self-sustained ones. The latter therefore have less IME contributions in their cooler NSE final state composition (Sharpe 1999).

In all the studies mentioned so far, detonation parameters have been calculated using the *steady state* assumption. A prerequisite for this to be appropriate is that

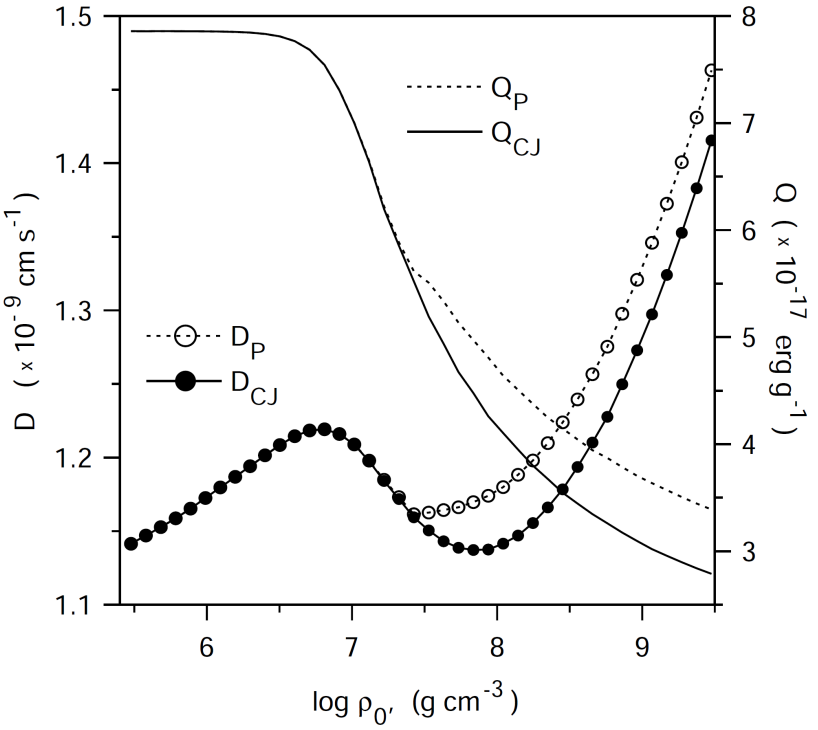

Figure 2.7.: Detonation velocities as a function of the upstream density for both the Chapman–Jouguet (D_{CJ}, filled circles) and the pathological case (D_{P}, open circles). Corresponding (effective) reaction q-values are also given (solid and dotted lines). This plot was taken from Gamezo et al. (1999). (Note that after NSE is established in the final state of the detonation in a Type Ia supernova at high enough densities, matter recombines to some degree during the expansion of the explosion products. Thus, the q-values shown in this figure do not correspond to those of the final explosion yields.)

the upstream state does not change on the timescale of the reactions taking place. An equivalent condition is that the detonation thickness ξ_{det} must be less than the characteristic length scale of changes of density and pressure L:

$$\xi_{\mathrm{det}} < L. \tag{2.44}$$

A similar consideration yields a lower boundary on the density needed for the formation of NSE, ρ_{NSE}: if ξ_{det} exceeds the size of the whole C/O-WD core $L_{\mathrm{WD}} \sim 10^8$ cm, the NSE relaxation cannot be established any more. As a result, IMEs are the final products of the non-steady detonation. Imshennik & Khokhlov (1984) and Khokhlov (1989) have estimated:

$$\rho_{\mathrm{NSE}} \approx 10^7 \ \mathrm{g\,cm^{-3}}. \tag{2.45}$$

Below this threshold the so-called *incomplete burning regime* applies. For example, the results shown in Fig. 2.7 are no longer valid in the context of a supernova explosion below ρ_{NSE}. Both the q-value and the detonation speed will be lower than shown there (see the results of the detonation calibration in Sect. 2.5 and Fig. 2.10).

Curvature effects Especially at low densities it matters that the front of a detonation wave is not plain, but usually has some curvature. An important quantity needed in the following discussion is the effective detonation length. It denotes the extent of the reactive area behind the front that drives the detonation shock by its energy release. This can be either the whole reaction zone length, or, if there is a sonic point in the reaction zone, it is the length between the shock and the (first) sonic point behind it. Curvature of the detonation front now has an important impact, as it causes the sonic point to move closer to the front and the effective detonation length to be shortened. This leads to a decrease of the detonation speed. As at low densities the detonation length becomes large, the amount of curvature needed to influence the burning is comparatively low. Therefore, according to Sharpe (2001), self-sustained C/O detonations in Type Ia supernovae are always pathological, at high densities due to endothermic silicon burning, and at low densities due to curvature effects. Sharpe (2001) finds that the effective burning length decreases by several orders of magnitude compared to the planar case, as the sonic point moves from the end of silicon burning to the end of oxygen burning. At the same time, however, the silicon burning length increases by several orders of magnitude owing to the lower detonation speeds and temperatures. This leads to an increase in ρ_{NSE} and the amount of IMEs that are expected to be produced in Type Ia supernovae due to incomplete burning.

Cellular instability If one considers multidimensional cellular instabilities, the transition to incomplete burning is again changing: Gamezo et al. (1999) use a partial resolution approach and show that for C/O detonations there is a "cells-within-cells-within-cells" structure, as the individual burning phases are subject

to the cellular instability independently and on very well separated length scales. In an average sense the main effect of the cellular instability is an increase in the reaction length scales. The carbon and oxygen burning lengths both are increased by a factor of 1.6, and the silicon burning length is increased by a factor of 1.3 (Gamezo et al. 1999). The latter means that the incomplete burning regime is shifted to higher densities and more IMEs are produced in Type Ia supernovae. Cellular instabilities also cause fluctuations in the nucleosynthetic yields and the final velocities of the burnt matter. These might become relevant at densities below 10^7 g cm^{-3}, where the inhomogeneities should occur on macroscopic scales. Gamezo et al. (1999) speculate that, if some of them survived, they could influence supernova spectra and also be responsible for the weak polarization detected. Both the inhomogeneities in the energy release and the increased reaction lengths should also have an impact on the extinction of the detonation, and thus, the range of expansion velocities of the processed ejecta (Gamezo et al. 1999; Sharpe 2001). Implications of the cellular instabilities on Type Ia supernovae also have been studied by Boisseau et al. (1996) and Timmes et al. (2000), who found the average detonation speed at an upstream density of 10^7 g cm^{-3} to be only ∼1–2% less than the Chapman–Jouguet value.

Density gradients Detailed studies of the effects of density gradients on detonations in Type Ia supernovae have not been published yet. If the effective detonation length is much smaller than the length scale of the density gradients, the structure of the reaction zone and the properties of the leading shock do not change. The detonation wave has time to adjust to the local density and propagates like in the steady self-sustaining case. When the length scales of the density gradient become comparable to the effective detonation length, as will be the case in the incomplete burning regime at low densities, the gradient will most likely lead to an increased detonation speed. But, additionally, the reaction zone structure will change and the problem will become time-dependent (Sharpe 2001). However, most studies cited above consider only steady solutions.

Density gradients, however, can also influence steady detonations. In steep density gradients, like in the outer layers of WDs, shocks that propagate towards lower density are strengthened. In the case of the incident shock of a detonation propagating down a density gradient, this leads to more steeply declining Rayleigh lines in Fig. 2.3(a) and thus to a higher detonation velocity. Assume that the initial shocked state of the detonation corresponds to point I_2 in the p–V plane (the Chapman–Jouguet case). If a density gradient strengthens the leading shock, the initial shocked state will evolve with time to reach point I_3.[3] This also means that the reaction zone structure changes with time, the pressure of the final state increases (while moving from C to S), and the detonation becomes more and more overdriven.

[3]Strictly speaking, the discussion here is only valid in a dimensionless p–V diagram, as the initial state will also move to lower densities and pressures.

A major difficulty for studying density gradient effects in Type Ia supernovae is that many of the "non-ZND" effects discussed in Sect. 2.2.2 become also important and influence each other at low densities:

- The cellular instability is important as the (largest) cell sizes become comparable to the characteristic scales of the problem.
- Due to the relatively large detonation length, curvature effects can become relevant, which shorten the effective detonation length and thus reduce the influence of density gradients (Sharpe 2001).

Summary C/O detonations have been studied extensively in degenerate WD matter, at least for the steady regimes. This may be a consequence of their importance for the currently favored delayed detonation models for Type Ia supernovae that include C/O detonations at all density regimes. Much less has been published on detonations in degenerate helium. This might be due to less interest of the supernova community or due to the lower complexity of their reaction kinetics. The general properties that have been published about helium detonations so far are discussed in the following.

Helium detonations

The nuclear reaction kinetics of helium detonations differs significantly from that of C/O detonations (see Khokhlov 1984 and Khokhlov & Érgma 1985, who investigate helium burning at constant density and temperature). In the regions of the T–ρ plane relevant for helium detonations, one can distinguish between two consecutive phases: an *initial helium burning phase* and, after helium exhaustion, an *NSE relaxation phase*. The leading reaction of helium burning (at least in pure helium detonations) is the triple-α reaction: $3\,{}^4\mathrm{He} \rightarrow {}^{12}\mathrm{C}$. Above $T \sim 5 \times 10^8$ K its time scale, $\tau_{3\alpha}$, varies only slowly with temperature, but it scales with ρ^{-2} (see, e.g., Khokhlov 1989). After the formation of a ^{12}C nucleus, a series of α-capture reactions process this "seed" towards higher mass numbers. The time scale τ_A for α-captures on a nucleus with mass number A decreases rapidly with temperature, but it increases toward higher mass numbers A. The reason for this behavior is the core Coulomb barrier that the α-particles have to pass. This barrier increases with charge and thus with mass number of the nucleus. Since initially $\tau_A \ll \tau_{3\alpha}$, α-captures on a ^{12}C seed nucleus are much faster than the formation of new seeds by the triple-α reaction. Therefore, the matter is rapidly processed to some maximum mass number A^* that is determined by the Coulomb barrier and the temperature. The contribution of nuclei with $A < A^*$ is small, but at low densities some unburnt ^{4}He might remain. Depending on the maximum temperatures and densities achieved in the detonation shock, A^* can have values between 12 and 56 (Khokhlov & Érgma 1985). Above $A = 56$, photo-disintegration reactions (γ, α) become important and prevent mass numbers $A > 56$ to become most frequent. Thus, detonations with high post-shock temperatures do not reach mean mass

numbers $\bar{A}$ that are above 56, but they might have contributions of $A > 56$ after the helium burning phase that surpass those in NSE (Khokhlov & Érgma 1985).

NSE is the next burning stage that is encountered. For $\rho \gtrsim 5 \times 10^6$ g cm^{-3} the time scale for NSE formation is shorter than the helium burning time scale τ_{He} (see Khokhlov 1989, and their estimates for the corresponding length scales in their Fig. 9). Therefore, after ^{4}He exhaustion NSE sets in immediately. At densities $\rho \lesssim 5 \times 10^6$ g cm^{-3} an extended NSE relaxation layer follows the helium burning layer. In the shell detonations considered in this work, however, the hydrodynamic expansion time scales are too short to allow for the establishment of NSE.

It is very important to notice that in the helium case the NSE state consists of IGEs with $\bar{A} \simeq 56$. Thus, after helium burning ceases with $\bar{A} \simeq 56$ (at densities $\rho \gtrsim 5 \times 10^6$ g cm^{-3}), the NSE relaxation just leads to shifts within the abundances of the iron group and not to a noticeable energy release. Contrary to the C/O case, the energy release therefore is monotonic within the whole reaction zone for all upstream densities. This means that *steady plain detonations in helium are always of the Chapman–Jouguet type* (Khokhlov 1989).

A table of the Chapman–Jouguet parameters for helium detonations containing thermodynamic variables for the final state, q-values, and detonation speeds for $10^6 \leq \rho \leq 10^9$ g cm^{-3} was published by Khokhlov (1988). Values for the speed of detonations and other regimes of burning in helium can also be found in Timmes & Niemeyer (2000). The structure of a helium detonation at $\rho = 5 \times 10^6$ g cm^{-3} has been calculated by Khokhlov (1989), who also gives estimates for the detonation thickness as a function of fuel density.

Finally, it should be mentioned that, unlike for C/O detonations, studies on the multidimensional stability and the influence of curvature on helium detonations are still missing. Only Sharpe (2001) mentions briefly that the cellular instability might be crucial for the "edge-lit" detonation case of the sub-Chandrasekhar model for Type Ia supernovae (see Sects. 3.1.1 and 3.1.3). In this scenario, a detonation in an accreted helium shell causes a secondary detonation in a C/O-WD core when the helium detonation shock hits the core–shell interface. Due to the cellular instability, shock speeds and thus strengths can be at times much higher than in the steady detonation case. Also, the transverse waves of a helium detonation wrapping around the core could collide directly with the core and heat and compress the edge of the C/O core stronger than in the plain detonation case.

2.3. Detonation initiation

So far, the discussion was focused almost exclusively on well-developed stationary detonations. A question that was left out is the initiation of detonations. This topic is briefly reviewed here following Seitenzahl et al. (2009). Basically, there are two different ways of detonation initiation:

- *Direct initiation* by an external shock wave that enters an inflammable matter at a velocity above of its self-supporting detonation speed.

- *Spontaneous initiation* caused by a hot spot in the fuel from which the temperature decreases with a suitable gradient.

Direct initiation produces an overdriven detonation structure that can under suitable conditions relax to a self-supported detonation. This mechanism might be relevant for the just mentioned edge-lit sub-Chandrasekhar supernova scenario. Most likely, however, the mechanism will only work for massive helium shells that are ignited at an altitude above the base of the shell (see Sect. 3.1.1). For the thin shell detonation models presented in Sect. 3.2, the maximum helium fuel densities and also the maximum densities reached in the shocked layers at the core boundaries are much lower. Thus, the remainder of this section neglects direct initiation and focuses on the spontaneous initiation case.

Spontaneous initiation can occur due to the Zel'dovich gradient mechanism (Zel'dovich et al. 1970). If there is a hot spot in the fuel that has a small gradient in temperature, then matter will start burning asynchronously. First, the burning will start at the temperature peak. Then, it will proceed outwards. The *induction time* τ_{ind}, i.e. the time until a thermonuclear runaway is initiated, depends on the local temperature. If there is only a small temperature gradient, the induction times will be very similar. Thus, the phase velocity $v_{\mathrm{ph}} = \mathrm{d}x/\mathrm{d}\tau_{\mathrm{ind}}$ of the ensuing reaction wave will be fast. This wave initiates a detonation if its velocity becomes equal to the self-supporting detonation speed of the matter. A more general theory to describe spontaneous detonation initiation than the one outlined here is that of "shock wave amplification by coherent energy release" (SWACER) behind the shock (Lee et al. 1978).

The length scales at which the detonation initiation occurs are usually not resolvable in multidimensional simulations of global supernova explosion models. Such simulations therefore rely on the results of off-line one-dimensional hydrodynamic calculations that resolve the relevant length scales and calculate critical quantities for detonation initiation from a hot spot. These critical masses or volumes, densities, and temperatures can be understood by a somewhat simplified analytical estimate of Woosley & Weaver (1994b): "The burning must accelerate in a time comparable to the duration of the compressed state. A lower limit is the sound crossing time in the hot region ...". (An even weaker and non-sufficient condition for detonation initiation is that the burning time scale at a location must be shorter than the local dynamical time scale.) Thus, for a given mass or volume of matter at constant density, a critical minimum temperature can be calculated to ensure fast enough burning time scales. On the other hand, for a given temperature, a critical mass or volume that needs to have the same temperature can be derived.

Published critical quantities are, however, calculated in a more general way by hydrodynamic simulations that are probing the SWACER for a given parametrization of the temperature profile of the hot spot. Niemeyer & Woosley (1997), e.g., assume a hot spot with a radial temperature distribution that decreases linearly with mass coordinate and that has constant density. For a given temperature peak and density, they determine the critical masses needed for detonation initiation.

Table 2.1.: Critical masses for detonations at given density and temperature according to Niemeyer & Woosley (1997).

ρ [g cm^{-3}]	T_c [10^9 K]	M [g]	R [m]
2×10^9	2.8	2.0×10^{15}	0.7
10^8	3.2	2.0×10^{15}	2
3×10^7	3.2	2.0×10^{19}	50

Table 2.2.: Critical temperatures for detonations at given density and mass according to Röpke et al. (2007b). Detonation initiation is impossible for $\rho \leq 1 \times 10^6$ g cm^{-3}.

ρ [g cm^{-3}]	T_c [10^9 K]	M [g]	R [km]
10^7	2.8	2.5×10^{23}	2
10^7	2.0	2.0×10^{25}	8
10^7	1.9	1.5×10^{27}	30
3×10^6	2.3	2.0×10^{28}	120

Table 2.1 presents an excerpt of their results for high density matter with equal mass fractions of carbon and oxygen. Röpke et al. (2007b) use the same code and setup to determine critical temperatures for lower densities (Table 2.2). They find detonation initiation to be impossible for $\rho \lesssim 10^6$ g cm^{-3}. Both tables are applied in the double-detonation sub-Chandrasekhar simulations of Sect. 3.2 to decide when to trigger a core detonation.

A more general approach is taken by Seitenzahl et al. (2009): using similar hydrodynamic simulations they additionally investigate the dependence on the functional form of the temperature gradient, the background temperature, the geometry (planar/spherical), and multidimensional effects (cellular detonations). Drawbacks of using simplified criteria for spontaneous detonation initiation are discussed in Sect. 3.2.1.

2.4. Simulating detonations in full-star simulations

The simulation of detonations in white dwarf matter in general requires solving the hydrodynamic equations together with the kinetic equations of nuclear burning (see Sect. 2.1.1). In the context of modeling full-star Type Ia supernova explosions this is, however, not feasible: the range of scales that needs to be covered on a numerical grid is far too wide, ranging from the WD diameter of $\sim 10^9$ cm down to the carbon burning length that can be as small as 10^{-2} cm (see Khokhlov 1989, for density-dependent detonation widths). Thus, in full-star simulations, in general, the reaction zone cannot be resolved. Without a special treatment for the burning, this leads to artificially spread numerical detonation waves that can have wrong propagation speeds, final states, and therefore also nucleosynthesis (Sharpe 2001).

To get reliable results, in this work, the flame propagation and the hydrodynamics of the flow are treated separately. The hydrodynamic evolution is calculated on a grid that does not resolve the microphysical structures that are responsible for nuclear burning. On this grid, the detonation propagation is modeled in a parametrized way that mimics the behavior of the microscopic processes, ensuring the correct large-scale explosion dynamics. A model that is physically rigorous on these scales is the discontinuity approximation for the detonation flame (see Sect. 2.2.1).

As the reaction zone is not resolved, the detonation velocity and also the energy release and the final composition have to be provided as external parameters. By means of an operator split approach the flame propagation and the burning can be decoupled from the remaining parts of the flow equations and can be treated separately in the numerical scheme.

The calculation of synthetic observables of supernova explosions requires the determination of detailed elemental abundances. To this end, a nucleosynthesis post-processing step is performed after the hydrodynamic simulation: a large nuclear network is solved for the density and temperature evolution determined in the simulation.

In this section, the numerical methods to model detonation burning in global Type Ia supernova simulations are described. After the hydrodynamic model and its discretization (Sect. 2.4.1), the parametrized treatment of nuclear burning is explained (Sect. 2.4.2). Finally, the nucleosynthesis post-processing scheme is discussed (Sect. 2.4.3).

2.4.1. Hydrodynamics

To model the flow of material in white dwarf stars, in general, the Navier-Stokes equations have to be solved. For the global supernova problem, the discretization of the equations on an Eulerian grid simplifies the problem significantly: as viscous effects only play a role on scales that are much smaller than those resolved on the grid in full-star simulations, it is sufficient to use the simpler Euler equations.

As mentioned before, by means of an operator splitting the hydrodynamics of the flow and the propagation of the detonation flame are calculated separately. Therefore, the problem is reduced to the solution of the Euler equations as given in (2.1)–(2.3) together with an equation of state for white dwarf matter (2.11). The latter includes contributions from an arbitrarily degenerate and arbitrarily relativistic electron gas, a photon gas, electron-positron pairs, and nuclei with a Maxwell-Boltzmann distribution.

To take into account self-gravity, appropriate source terms have to be added to the equations of momentum and energy conservation:

$$\frac{\mathrm{D}\boldsymbol{u}}{\mathrm{D}t} + V\boldsymbol{\nabla}p = -\boldsymbol{\nabla}\Phi_\mathrm{g}, \tag{2.46}$$

$$\frac{\mathrm{D}\varepsilon}{\mathrm{D}t} + p\frac{\mathrm{D}V}{\mathrm{D}t} = -\rho\,\boldsymbol{u}\cdot\boldsymbol{\nabla}\Phi_\mathrm{g}, \tag{2.47}$$

where Φ_g is the gravitational potential that is determined by Poisson's equation:

$$\Delta\Phi_g = 4\pi\mathcal{G}\rho. \tag{2.48}$$

The latter is solved using the monopole approximation in the simulations of Sect. 3.2 and with a multipole solver in the asymmetric rotating models of Chap. 4 (see Sect. 4.4.2).

The straightforward finite difference discretization of the Euler equations, in which derivatives are replaced by difference quotients, is non-conservative and tends to smear out shocks. Instead, a *finite volume method* is applied, which is conservative by construction: for a certain time interval, the fluxes of mass, momentum, and energy between the individual grid cells are calculated; then, the mean values of each cell are updated accordingly. The foundation of such schemes is the integral form of the Euler equations.

To determine the fluxes in his scheme, Godunov (1959) assumed a constant state in every cell and solved a Riemann shock tube problem at the (hypothetical) discontinuity between two given cells. Apart from the conservativity, this scheme has the advantage of a shock-capturing property by construction. Higher order schemes of the *Godunov type* are similar, but they calculate the input states of the Riemann problems—the state variables at the cell interfaces—by higher order interpolation from the values at the cell centers. This way, they are more accurate and less diffusive than the original scheme, but also more computationally demanding. As they allow for a certain accuracy already at lower grid resolution, they are however preferred in multidimensional simulations.

In this work, the *Piecewise Parabolic Method* (PPM) of Colella & Woodward (1984) is applied, which is a Godunov type scheme that uses parabolas to reconstruct the interface states. The hydrodynamics code used for all simulations is based on the PROMETHEUS implementation (Fryxell et al. 1989) of PPM and applies the exact Riemann solver of Colella & Glaz (1985). To avoid solving multidimensional Riemann problems, directional splitting is used in two- and three-dimensional calculations. The integration time step is calculated according to the Courant-Friedrichs-Lewy criterion (see e.g. Courant & Friedrichs 1948) and further reduced by multiplication with a Courant factor of 0.8, to ensure numerical stability. A more detailed description of the computer code can be found in Reinecke (2001).

2.4.2. Simplified treatment of detonations

For most density regimes that are relevant for the dynamics of Type Ia supernova explosions, the detonation width is much shorter than the characteristic length scales of the WD. While the detonation propagates through a WD in hydrostatic equilibrium, the upstream densities only change on time scales that are much longer than those of nuclear burning. Thus, the initial states in the unburnt fuel can be approximated as constant and the solutions for the reaction zone structure are quasi-steady.

As the detonation structure can be assumed to be thin and steady, the discontinuity approximation (see Sect. 2.2.1) is a suitable model for most parts of the WD. To correctly model the explosion hydrodynamics of detonations in Type Ia supernova explosions, it is therefore sufficient to propagate the reactive discontinuity (also called burning front or flame in the following) at the appropriate speed with the fast reactions happening spontaneously at its passage and only the density-dependent products, but no reaction rates being calculated. To this end, a simplified scheme for nuclear reactions and a front tracking method based on level sets are applied (see Stewart 1998, for an alternative scheme used for detonations in solids).

The applied scheme, also requires that the detonation speed, the energy release, and the final composition are known as function of the local state of the fuel. For low density incomplete burning regimes, however, q-values and nucleosynthetic yields are not available and in general problem-dependent (see the discussion at the beginning of Sect. 2.5). Therefore, in this work these quantities are determined with a large nuclear network in an iterative calibration scheme (see Sect. 2.5). In the following, the simplified detonation scheme is explained in detail (for potential restrictions of the method see Sects. 2.5.3 and 2.5.4).

Simplified scheme for nuclear reactions

To simulate the dynamics of a detonation in a full-star supernova simulation, it is sufficient to use a strongly simplified scheme for nuclear reactions as in Reinecke et al. (2002a). In order to approximate the energy release in the fast reactions driving the detonation and the mean molecular weight of fuel and ashes, only a few species are needed: for each group of elements that is involved, a representative species is chosen with a binding energy and mass typical for the group. In total there are five species, namely helium, carbon, oxygen, IMEs ($A = 30$), and IGEs ($A = 56$). Their mass fractions can be summarized in the following array:

$$\boldsymbol{X}^{\mathrm{red}} = (X^{\mathrm{red}}_{^4\mathrm{He}}, X^{\mathrm{red}}_{^{12}\mathrm{C}}, X^{\mathrm{red}}_{^{16}\mathrm{O}}, X^{\mathrm{red}}_{\mathrm{IME}}, X^{\mathrm{red}}_{\mathrm{IGE}}). \tag{2.49}$$

All the reactions taking place are represented by transitions within this reduced set of species. When the flame front crosses a grid cell, the volume fraction of the cell occupied by the burnt state is instantaneously converted into ash by updating the above mass fractions and releasing the appropriate reaction q-value according to (2.36) and (2.37). To this end, the post-detonation abundances of these species have been tabulated with respect to the density of the unburnt state in both C/O and helium fuels. Details of the calibration of this table using the large post-processing network (see Sect. 2.4.3) are explained in Sect. 2.5. The main results are displayed in Figs. 2.8 and 2.9.

At densities above ρ_{NSE} (see Eq. 2.45), the final state of the detonation will be in NSE. This state is represented by a temperature- and density-dependent mixture of ^{56}Ni and ^{4}He in the model. In order to distinguish the ^{4}He in the helium shell from that produced in NSE, both are treated as different species in the code. With decreasing densities the ^{4}He in NSE finally recombines to ^{56}Ni. This

is the only slow reaction included in the simulations. A NSE data table provided by H.-Th. Janka (private communication) is used to determine the appropriate NSE states.

The level set technique

The propagation of the detonation flames is modeled with the *level set technique* (Osher & Sethian 1988) in the implementation of Golombek & Niemeyer (2005), which in turn is based on the deflagration flame model of Reinecke et al. (1999b). In this scheme the the flame front Γ is implicitly represented by the zero level set of a signed distance function G:

$$\Gamma(t) \equiv \{\boldsymbol{r} \,|\, G(\boldsymbol{r}, t) = 0\}\,, \tag{2.50}$$

$$|\boldsymbol{\nabla} G| \equiv 1. \tag{2.51}$$

Information on whether matter has already been burnt is encoded in the sign of G, which is negative in the fuel and positive in the ashes. The absolute value of G yields the distance to the front in every point.

In the following derivation, the normal vector $\boldsymbol{n}$ to the flame front is needed:

$$\boldsymbol{n} = -\frac{\boldsymbol{\nabla} G}{|\boldsymbol{\nabla} G|}. \tag{2.52}$$

It is defined to point towards the unburnt material.

At every time step the flame propagation is performed in two steps: first, given that the detonation speed is known as a function of the local state, G is updated according to a simple differential equation derived below; then the roots of G are calculated to find the new location of the flame on the grid.

Now, the differential equation for the time evolution of G is constructed: consider a point P that is attached to the flame front Γ, i.e.

$$G(\boldsymbol{r}_\mathrm{P}, 0) = 0 \quad \text{and} \quad \frac{\mathrm{d}G(\boldsymbol{r}_\mathrm{P}, t)}{\mathrm{d}t} = 0. \tag{2.53}$$

The flame front is advected with the underlying flow at a velocity $\boldsymbol{v}$ and it propagates relative to the flow at velocity D in normal direction (here, both velocities are evaluated on the unburnt side of the front; in general, both velocities have to be determined on the same side of the front). Thus, the velocity of P must be as follows:

$$\boldsymbol{v}_\mathrm{P} = \boldsymbol{v} + D\boldsymbol{n}. \tag{2.54}$$

Now the time evolution of G can be determined using (2.53):

$$\frac{\mathrm{d}G(\boldsymbol{r}_\mathrm{P}, t)}{\mathrm{d}t} = \frac{\partial G(\boldsymbol{r}_\mathrm{P}, t)}{\partial t} + \boldsymbol{v}_\mathrm{P} \cdot \boldsymbol{\nabla} G(\boldsymbol{r}_\mathrm{P}, t) = 0. \tag{2.55}$$

With (2.54) and (2.52) and when omitting the dependency on $\boldsymbol{r}_\mathrm{P}$ this yields:

$$\frac{\partial G}{\partial t} = -\left(\boldsymbol{v} + D\boldsymbol{n}\right)\left(-\boldsymbol{n}|\boldsymbol{\nabla} G|\right) = \left(\boldsymbol{v} \cdot \boldsymbol{n} + D\right)|\boldsymbol{\nabla} G|. \tag{2.56}$$

This so-called "G-equation" is only valid for points at the front since only here D is physically defined. In all other points, another prescription for $\partial G/\partial t$ has to be found, or an appropriate prescription for the propagation velocity has to be used. In this work, for simplicity, in every grid cell the velocity D a potential detonation front would have there is calculated and the evolution of G is integrated according to (2.56). Afterwards, however, in all points that are more than a certain distance away from the front the property of G as a distance function (2.51) has to be restored in a so-called re-initialization step (for details, see Sussman et al. 1994; Reinecke 2001) because this property is not automatically preserved in hydrodynamic advection.

The propagation of the level set function according to the G-equation consists of two parts: the advection with the flow and the self-propagation by burning, respectively. By means of an operator splitting approach, the advection of G can be treated in the same way as that of a passive scalar in the hydrodynamic scheme (Mulder et al. 1992; Reinecke et al. 1999b,a). The burning part is accounted for by (Reinecke 2001)

$$\left(\frac{\partial G}{\partial t}\right)_{\text{burn}} = D|\boldsymbol{\nabla} G|.$$

Flame/flow coupling

Between two time steps of the finite-volume hydrodynamics scheme, as described above, the detonation flame is propagated and in cells intersected by the front the species are updated in the burnt volume fraction and an appropriate amount of reaction energy is released. In intersected cells, this however leads to a mixture of fuel and ashes. Expressed e.g. for the density this means:

$$\rho = \alpha\rho_{\text{u}} + (1-\alpha)\rho_{\text{b}}, \tag{2.57}$$

where α is the volume fraction of the cell occupied by the unburnt state, and subscripts 'u' and 'b' refer to quantities on the unburnt and the burnt side of the front, respectively.

To propagate the flame according to (2.56), both flow and burning velocities (and thus the state) are needed of the unburnt part of such intersected cells. The unburnt density ρ_{u} is also required to determine the abundances of the burning products and the q-value in the simplified scheme for nuclear reactions.

With the so-called "complete coupling" scheme (Smiljanovski et al. 1997; Reinecke et al. 1999b) the two partial states can be reconstructed from the mixed state at every time step. This enables the separate treatment of the flow of burnt and unburnt material over the grid boundaries ("flux splitting") and avoids numerical mixing of fuel and ashes. While a complete coupling scheme has been implemented for two-dimensional small-scale deflagration flame simulations in white dwarf matter (Röpke et al. 2003, 2004a,b), numerical obstacles prevent its application in full star simulations up to now (the main problem is the extreme behavior of the equation of state for white dwarf matter at low temperatures).

Here, a scheme similar to the "passive implementation" of Reinecke et al. (1999b) is applied and the mixed state is used to advect G (this assumes that the jump in the velocity across the burning front is small compared to the burning velocity). For the determination of D and the final burning yields, however, some techniques have been implemented to get at least an approximation for both the burnt and the unburnt state of a cell that is intersected by the front. These are explained in the following.

Due to their supersonic propagation, detonation waves cannot influence the state of the matter ahead of them (see Sect. 2.1.3, where this behavior is discussed for shocks). Thus, if the detonation takes place in a WD that is initially in hydrostatic equilibrium and the grid is static, the initial density of each cell can be saved and used as exact value for ρ_u:

$$\rho_\mathrm{u} = \rho(0). \tag{2.58}$$

This scheme is applied in all helium shell detonations of this work and also in the calibration runs described in Sect. 2.5.

Provided that density gradients are small, the states of neighboring unburnt cells (in an environment U) can also be used to approximate ρ_u. For the smeared out structure of the flame on the hydrodynamic grid, it is found to be appropriate to define ρ_u as the minimum density of a cell in U for which at least 80% of the fuel is still unburnt. The minimum is taken to avoid the von Neumann peak, which is the peak of the reaction zone seen in Fig. 2.2. Analogously, ρ_b (the density of the final state in Fig. 2.2) can be defined as the minimum density of a cell in U for which less than 80% of the fuel is still unburnt. Expressed in formulas these definitions read:

$$\rho_\mathrm{u} = \min_{\substack{\boldsymbol{r}\in U \\ X_\mathrm{fuel}(\boldsymbol{r})\geq 0.8}} \rho(\boldsymbol{r}), \tag{2.59}$$

$$\rho_\mathrm{b} = \min_{\substack{\boldsymbol{r}\in U \\ X_\mathrm{fuel}(\boldsymbol{r})\leq 0.8}} \rho(\boldsymbol{r}), \tag{2.60}$$

where, U is the environment not further away than four cells from the current cell (as four is approximately the width of smeared out discontinuities in the hydrodynamic scheme). The mass fraction X_fuel refers to the amount of unburnt fuel that is still present in a grid cell. If needed, approximations for all other state variables of the unburnt and the burnt state can also be determined: they can simply be read out from the same cells as ρ_u and ρ_b in (2.59) and (2.60).

Detonation velocities

With the density and the other state variables being available in the fuel and the ash state, the detonation velocity can be determined. For the helium detonation the Chapman–Jouguet case is assumed and the burning speed relative to the ashes

is the local sound speed. Combining equations (2.16) and (2.39) yields:

$$(D-u)_{\mathrm{He}} = \sqrt{\gamma_{\mathrm{b}} \left(\frac{\partial p_{\mathrm{b}}}{\partial \rho_{\mathrm{b}}}\right)_T} = \sqrt{\frac{\gamma_{\mathrm{b}} p_{\mathrm{b}}}{\rho_{\mathrm{b}}}}, \tag{2.61}$$

with u being the final state velocity in the frame where the fuel state is at rest. When expressed relative to the ashes, the velocity (2.54) of a point P on the flame front becomes

$$\boldsymbol{v}_{\mathrm{P}} = (\boldsymbol{v} + u\,\boldsymbol{n}) + (D-u)\boldsymbol{n} \equiv \boldsymbol{v}' + (D-u)\boldsymbol{n},$$

with $\boldsymbol{v}'$ being the background flow velocity behind the front. Thus, when applying (2.61), $\boldsymbol{v}'$ should be used instead of $\boldsymbol{v}$ for the advection of G. But, due to the passive implementation of the level set scheme, only a mixed state velocity $\bar{\boldsymbol{v}}$ in between $\boldsymbol{v}'$ and $\boldsymbol{v}$ is available. This leads to a somewhat too low resulting front velocity when prescribing the detonation velocity relative to the ash state as in (2.61); on the other hand, the resulting detonation velocity is somewhat too high when using a prescription relative to the fuel state.

In C/O, self-sustained detonations are of pathological type above $\rho \sim 2 \times 10^7\ \mathrm{g\,cm^{-3}}$ (see Sects. 2.2.2 and 2.2.3) and of Chapman–Jouguet type below. For the burning speed relative to the fuel the values of Gamezo et al. (1999) are used above $10^7\ \mathrm{g\,cm^{-3}}$ (see Fig. 2.7):

$$D_{\mathrm{C/O}} = f_{\mathrm{Gamezo}}(\rho_{\mathrm{u}}), \quad \rho > 10^7\ \mathrm{g\,cm^{-3}}. \tag{2.62}$$

Below, the table of Gamezo et al. (1999) is no longer valid, as it does not account for the burning becoming incomplete in WDs at $\rho \lesssim 10^7\ \mathrm{g\,cm^{-3}}$ (see Sect. 2.2.3). In this regime, the Chapman–Jouguet velocities are taken from a table that has been calculated relative to the fuel during the iterative detonation calibration as described in Sect. 2.5.2 (see Fig. 2.10):

$$D_{\mathrm{C/O}} = f_{\mathrm{calib.\,table}}(\rho_{\mathrm{u}}), \quad \rho < 10^7\ \mathrm{g\,cm^{-3}}. \tag{2.63}$$

Here, in principle, the above scheme for the helium detonation could be used, which is easy to calculate. However, changing from (2.62) to (2.61) at $10^7\ \mathrm{g\,cm^{-3}}$ causes a significant jump in the resulting front velocity that was found to be problematic in the iterative abundance calibration of Sect. 2.5.1. This jump is a consequence of the usage of the mixed advection velocity $\bar{\boldsymbol{v}}$: the error in the advection velocity is discontinuous and changes sign at $10^7\ \mathrm{g\,cm^{-3}}$. By using (2.63) this is avoided.

2.4.3. Post-processing

As it is prohibitively expensive to include a large nuclear network in a full-star hydrodynamic simulation in multiple dimensions (due to time step constraints), the simplified scheme for nuclear reactions combined with the detonation front tracking technique of the last section are applied to allow for an approximately correct energy release and mean molecular weight during the explosion. Consequently, the

resulting density, temperature, and velocity evolution should also be realistic and can be used to calculate detailed nucleosynthesis in a post-processing step.

A very convenient way to do this is to determine a "Lagrangian representation" of the explosion. Initially the star is divided into an ensemble of fluid elements with given masses. Then in every such element a virtual *tracer particle* is placed. Roughly speaking, a tracer particle is a coordinate that is propagated with the velocity field of the flow during the simulation to record the evolution of the enclosing fluid element. The state variables at the tracer positions are determined by linear interpolation on the Eulerian grid of the hydrodynamic simulation. Recording the density and temperature trajectories of all tracer particles with a certain sampling rate yields a Lagrangian representation of the supernova.

For every tracer particle it is now possible to independently calculate detailed nucleosynthesis from its temperature and density evolution using a large nuclear network. Due to the Lagrangian nature, no matter exchange with other particles has to be considered during the calculation. If needed, temperature and density values at additional time steps can be determined by linear interpolation in between the recorded tracer time steps.

The tracer particle setup and the large nuclear network used in this work are similar to those of Travaglio et al. (2004). The network includes 384 species ranging from protons, neutrons, and α-particles to ^{98}Mo. A description of the code used to solve the nuclear network can be found in Thielemann et al. (1990), Thielemann et al. (1996), and Iwamoto et al. (1999). The reaction rate libraries adopted are the same as in those references, however, newer tables for weak reaction rates (Langanke & Martinez-Pinedo 2000) were used as described in Travaglio et al. (2004).

In the two-dimensional double-detonation sub-Chandrasekhar simulations of Sect. 3.2 a number of $n_{\mathrm{core}} = 80 \times 160 = 12\,800$ tracer particles is placed equidistant in radial mass coordinate and $\cos\theta$ in the WD core such that each particle represents the same mass. An offset is added to the coordinates such that each particle has a random initial position within its corresponding fluid element. To spatially resolve the nucleosynthesis in the thin helium shell despite its lower total mass, the same number of $n_{\mathrm{sh}} = n_{\mathrm{core}}$ tracer particles is placed there. With this distribution, particles in the core and in the shell represent masses of $M_{\mathrm{core}}/n_{\mathrm{core}}$ and $M_{\mathrm{sh}}/n_{\mathrm{sh}}$, respectively.

As the rotating WD models of Chap. 4 are not spherically symmetric, a simple mass coordinate (M_r) cannot be defined. Therefore, a tracer particle placement on a certain number of mass shells as done for the sub-Chandrasekhar simulations mentioned above is not possible. Instead, a rejection method (see e.g. Press et al. 2007) is applied to determine a random tracer particle distribution that represents the density profile of the star: a random position (x^*, y^*, z^*) is determined in the WD; a tracer particle is then placed at this position with a probability of

$$P = \frac{M^*}{M} \times \frac{\overline{\Delta V}}{\Delta V^*}, \quad \overline{\Delta V} = V_{\mathrm{grid}}/n_{\mathrm{grid}}, \tag{2.64}$$

otherwise the position is rejected; further random positions are determined and either chosen or rejected, until a number of $n_{\mathrm{tr}} = 100\,000$ particles is reached. Here, M is the total mass of the star and M^* and ΔV^* denote the mass and the volume of the grid cell in which the randomly picked point lies, respectively. $\overline{\Delta V}$ is the average volume of a cell on the grid which has a total volume V_{grid} and consists of n_{grid} cells. The first factor in (2.64) simply means that the probability scales with the mass of the cell. The second term is needed to correct for the increased likelihood of cells with a volume larger than the average volume $\overline{\Delta V}$ of being picked by the random position determination. Each randomly placed tracer particle now represents an equal mass of M/n_{tr}.

2.5. Iterative calibration of the detonation scheme

To determine accurate nucleosynthetic yields from the tracer information with the post-processing technique, the accurate amount of energy must be released in the hydrodynamic simulation. As mentioned in Sect. 2.4.2, no nuclear network is solved in the code to determine the burning products. Instead, a prescription is used that allows the determination of the final energy release and composition as a function of the local fuel density in front of the flame. Therefore, the burning yields have to be known as a function of ρ_{u}.

In previous studies (Fink et al. 2007) a sharp transition between burning to NSE and incomplete burning at a certain estimated density was assumed in the C/O detonation. Additionally, burning was stopped below a roughly estimated minimum fuel density. Therefore, the total amount of IGEs and IMEs produced was relatively uncertain. In this work, a table is applied that contains the final abundances of all burning regimes as a function of the upstream density. This data describes the transitions between the regimes much more accurately than the old scheme.

The supernova explosion simulations of this work include significant contributions of the low density incomplete burning regime in C/O detonations ($\rho \lesssim 10^7$ g cm^{-3}). All of the helium detonations take place in a low density incomplete regime ($\rho \lesssim 10^6$ g cm^{-3}). For these regimes, q-values and final state compositions are not available, as almost all published studies are restricted to steady state detonations. In the case of helium detonations, there is not much information published at all (see Sect. 2.2.3).

In unsteady regimes and close to extinction, the detonation outcomes are in general problem-dependent and are influenced e.g. by the dynamical expansion behind the front. Therefore, it makes sense to calibrate the tables in hydrodynamic simulations that are similar to the supernova models in which these tables shall be applied, as the simulations correctly treat all expansion effects.

Note, that in the unsteady regimes also the thin flame approximation might become problematic and the maximum temperatures could be somewhat overestimated due to the instantaneous energy release behind the front. But, as no better

scheme is available yet, the following calibration can still be used to improve the previous abundance tables and, in the helium case, to produce such tables for the first time.

2.5.1. Calibration of nucleosynthetic abundances

In the following, a prescription for the density-dependent detonation yields in terms of the reduced set of species $\boldsymbol{X}^{\mathrm{red}}$ (see Eq. 2.49) that is part of the simplified scheme for nuclear reactions (see Sect. 2.4.2) shall be determined. This is achieved by refining an initial guess for $\boldsymbol{X}^{\mathrm{red}}(\rho_{\mathrm{u}})$ in an iterative scheme that includes a series of hydrodynamic simulations of fiducial detonations in a WD and corresponding post-processing calculations.

Iteration scheme

An iteration step can be performed according to the following list of instructions:

- given is a guess for $\boldsymbol{X}^{\mathrm{red}}(\rho_{\mathrm{u}})$ from the previous iteration step that corresponds to a (slightly) too large q-value (as initial guess the production of pure ^{56}Ni is a suitable choice);
- carry out a hydrodynamic simulation of the fiducial detonation including tracer particles that record $\rho(t)$, $T(t)$, and the upstream density $\rho_{\mathrm{u}} = \rho(t = 0)$ at which the detonation wave has reached them;
- post-process the tracer trajectories and find detailed abundances $\boldsymbol{X}(\rho_{\mathrm{u}})$ that now correspond to a more realistic q-value (the overestimation of q should be lower, the reason is explained below);
- sum up the groups on nuclei in $\boldsymbol{X}(\rho_{\mathrm{u}})$ to determine the improved reduced set of species $\boldsymbol{X}^{\mathrm{red}}(\rho_{\mathrm{u}})$.

The reason why the post-processing abundances in the scheme above should yield a more realistic q-value are now discussed. An overestimation of the reaction q-value released behind the detonation front of the simplified detonation scheme will produce higher maximum temperatures and pressures, but the densities during the main parts of the burning will be unmodified. The higher pressures will cause a somewhat faster expansion, but most likely only at later times. Thus, importantly, the density evolution can be assumed to be approximately correct. Obviously, if a certain q-value is released in the hydrodynamic scheme, the reactions in the post-processing will not produce a final state that corresponds to a larger q-value. But, if the local density is too low to be consistent with the currently assumed q-value (as all the reactions considered here depend on density), the post-processing reaction network will rather produce a lower q-value. Therefore, as the densities are approximately correct, the above iteration scheme will finally produce abundances $\boldsymbol{X}^{\mathrm{red}}(\rho_{\mathrm{u}})$ that correspond to consistent reaction q-values.

For completeness, now, the scheme to determine $\boldsymbol{X}^{\mathrm{red}}(\rho_{\mathrm{u}})$ from $\boldsymbol{X}(\rho_{\mathrm{u}})$ (fourth point of the above list) is given. The abundances of the five "reduced" species,

$$\boldsymbol{X}^{\mathrm{red}} = (X^{\mathrm{red}}_{^4\mathrm{He}}, X^{\mathrm{red}}_{^{12}\mathrm{C}}, X^{\mathrm{red}}_{^{16}\mathrm{O}}, X^{\mathrm{red}}_{\mathrm{IME}}, X^{\mathrm{red}}_{\mathrm{IGE}}),$$

can be determined from the 384 post-processing mass fractions,

$$\boldsymbol{X} = (X_{\mathrm{p}}, X_{\mathrm{n}}, X_{^4\mathrm{He}}, X_{^6\mathrm{He}}, \ldots, X_{^{97}\mathrm{Mo}}, X_{^{98}\mathrm{Mo}}),$$

by summing up the represented groups of nuclei (shown are the formulas for the C/O detonation case):

$$X^{\mathrm{red}}_{^4\mathrm{He}} = 0, \tag{2.65}$$

$$X^{\mathrm{red}}_{^{12}\mathrm{C}} = X_{\mathrm{C}}, \tag{2.66}$$

$$X^{\mathrm{red}}_{^{16}\mathrm{O}} = X_{\mathrm{O}} + X_{\mathrm{Ne}}, \tag{2.67}$$

$$X^{\mathrm{red}}_{\mathrm{IME}} = \sum_{j=\mathrm{Na}}^{\mathrm{Sc}} X_j, \tag{2.68}$$

$$X^{\mathrm{red}}_{\mathrm{IGE}} = \sum_{j=\mathrm{Ti}}^{\mathrm{Mo}} X_j + X_{\mathrm{He}}. \tag{2.69}$$

For brevity, elemental abundances,

$$X_{\mathrm{El}} = \Sigma_{A=A_{\mathrm{min}}}^{A_{\mathrm{max}}} X_{^A\mathrm{El}},$$

are used here as a short notation for the sum over all isotopes of an element 'El'. NSE is represented only by IGEs in $\boldsymbol{X}^{\mathrm{red}}(\rho_{\mathrm{u}})$. Thus, in (2.69) X_{He} is added to the IGE abundance. As mentioned in Sect. 2.4.2, a better representation of NSE, a temperature and density-dependent mixture of ^{56}Ni and ^{4}He, is calculated with an NSE data table in a different module of the code. For the helium detonation case, the helium term in (2.69) is removed and added to the right hand side of (2.65).

Application to the C/O and the helium detonation case

The above scheme was applied to calibrate the detonation scheme presented in Sect. 2.4.2 by iteratively determining $\boldsymbol{X}^{\mathrm{red}}(\rho_{\mathrm{u}})$ for both detonations in degenerate C/O and helium. As fiducial explosion scenario detonations were centrally ignited in a WD with a central density of 5×10^7 g cm^{-3}, a constant temperature of 3×10^7 K and a total mass of 0.83 $M_\odot$. The central density was chosen to lie somewhere in the middle of those of the sub-Chandrasekhar model series of Sect. 3.2. White dwarfs with lower central densities have the advantage that a greater fraction of their mass is located in the relevant low density regime, which is thus easier to resolve. A number of $n_{\mathrm{tr}} = 101$ tracer particles was placed along the r-axis of the cylindrical grid. The particles were distributed to resolve the whole relevant $\log \rho$ range.

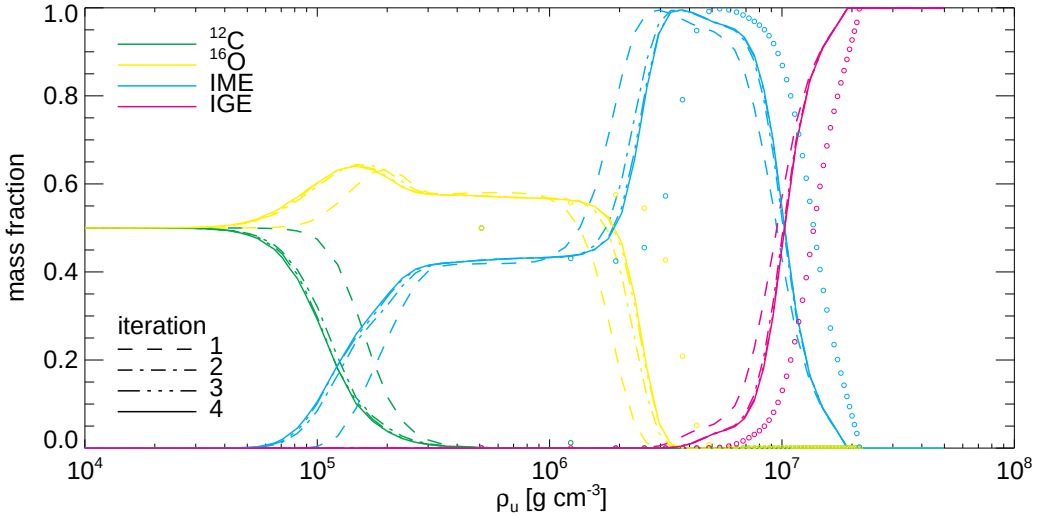

Figure 2.8.: Mass fractions of the species in the C/O detonation table plotted against the density of the unburnt fuel ρ_u. The fractions of ^{12}C, ^{16}O, IMEs, and IGEs are plotted in green, yellow, blue, and magenta, respectively. Dashed, dot-dashed, dot-dot-dot-dashed, and solid lines are used to distinguish between the four iteration steps in ascending order. Empty circles show the results of a one-dimensional detonation simulation of S. E. Woosley (private communication).

As starting point, the production of pure ^{56}Ni was assumed at all fuel densities:

$$\boldsymbol{X}^{\mathrm{red}}(\rho_u) = (0, 0, 0, 0, 1).$$

After four iterations the tables $\boldsymbol{X}^{\mathrm{red}}(\rho_u)$ seemed to be converged well enough. Figures 2.8 and 2.9 show the resulting sequences of tables for both the C/O and the helium detonation case. The dashed, dot-dashed, dot-dot-dot-dashed, and solid lines mark the successive iteration results after post-processing the first, second, third, and the final fourth hydrodynamic simulation. Together with F. K. Röpke a table for C/O deflagrations was determined in an analogous way. The fact that the mass fractions as functions of ρ_u do no longer change suggests that a *self-consistent solution* has been reached. This means that the yields of the hydrodynamic simulation $\boldsymbol{X}^{\mathrm{red}}$ and the post-processing $\boldsymbol{X}$ are consistent in terms of nucleosynthesis and energy release. For the C/O detonation, the results are found to agree reasonably well with those of one-dimensional detonation simulations of S. E. Woosley (private communication, see the open circles in Fig. 2.8). However, the transition of the burning phases are all shifted to slightly lower densities in the table of this work.

In the C/O detonation table shown in Fig. 2.8 all major burning phases are visible: carbon burning, oxygen burning, and silicon burning. Above densities of about 2×10^7 g cm^{-3}, NSE is reached (represented here only by IGEs). Helium

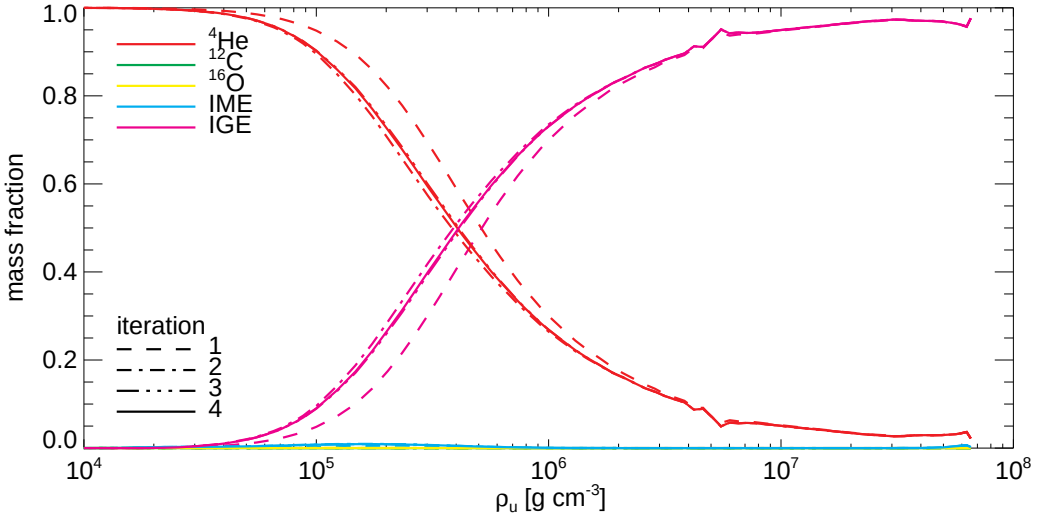

Figure 2.9.: Mass fractions of the species in the helium detonation table against ρ_u. For details see the caption of Fig. 2.8.

burning (Fig. 2.9) produces mainly IGEs and only a small amount of IMEs at the low densities $\rho \lesssim 10^6$ g cm^{-3} that are relevant in the minimum shell-mass models of Sect. 3.2. A high fraction of the initial helium is left unburnt.

The two calculated tables (Figs. 2.8 and 2.9) are used in all the simulations presented in this work and ensure a consistent energy release and molecular weight in the hydrodynamic simulations. Although the calibration procedure does not account for potential changes in the detonation strength and expansion time scales in realistic simulations, it still provides a reasonable approximation (this will be shown in Sect. 2.5.3).

2.5.2. Calibration of the detonation speed

In the above calibration scheme the detonation speed D is assumed to be known as a function of density. If this is not the case, however, it can be determined in the course of the above iteration, provided that the detonation is of the Chapman–Jouguet type.

Iteration scheme

As explained in Sect. 2.2.2, D_CJ does not depend on internal details of the reaction zone, but only on the final state composition and the corresponding q-value (Eq. 2.36). Given these quantities, the detonation adiabat $\mathcal{H}_\mathrm{D}$ (2.35) can be determined and by finding the Rayleigh line $\mathcal{R}$ that is tangential to $\mathcal{H}_\mathrm{D}$, D_CJ can be calculated from (2.20). Note, that here q and the final composition are assumed to be constant at least in an environment around the Chapman–Jouguet point O in Fig. 2.3(a).

As the nucleosynthetic yields and the q-value depend on D (which determines the strength of the leading shock), a solution can only be found iteratively. For a given value of $\boldsymbol{X}^{\mathrm{red}}(\rho_{\mathrm{u}})$ in the iteration scheme of the last section, also $q(\rho_{\mathrm{u}})$ is known. Thus, an according function $D_{\mathrm{CJ}}(\rho_{\mathrm{u}})$ can be determined and used together with $\boldsymbol{X}^{\mathrm{red}}(\rho_{\mathrm{u}})$ in the next iteration step. To start an iteration, $D_{\mathrm{CJ}}(\rho_{\mathrm{u}})$ corresponding to the production of pure nickel is used.

A simple numerical scheme is applied to calculate D_{CJ} from $\boldsymbol{X}^{\mathrm{red}}$ and q at a given ρ_{u}. On $\mathcal{H}_{\mathrm{D}}$, the specific volume V can be determined for a given pressure p by performing a standard bisection search: $V = V_{\mathcal{H}_{\mathrm{D}}}(p)$. Calculating D_{CJ} from the Rayleigh line with minimum slope, is now equivalent to the following minimization problem:

$$D_{\mathrm{CJ}}\left(\rho_{\mathrm{u}}\right) = \min D(p) \overset{(2.20)}{=} \min V_{\mathrm{u}} \sqrt{\frac{p - p_{\mathrm{u}}}{V_{\mathrm{u}} - V_{\mathcal{H}_{\mathrm{D}}}(p)}}. \tag{2.70}$$

Note, that in this section ‘u’ is used instead of ‘0’ as subscript for the upstream state of the detonation. To find the minimum value of D, it is first bracketed with a triplet of points $p_a < p_b < p_c$, such that $D(p_b) < D(p_a)$ and $D(p_b) < D(p_c)$. Then, a “golden section search” is performed as described in Press et al. (2007).

Application to the C/O detonation

For the C/O detonation at $\rho > 10^7$ g cm^{-3}, the detonation velocity is available relative to the unburnt fuel (Eq. 2.62). Below, it can be calculated easily as the sound speed relative to the ashes. However, to avoid the numerical problems at this transition that were described in Sect. “Detonation velocities” on page 45, the above iteration scheme is applied to tabulate the detonation speed for $\rho < 10^7$ g cm^{-3} relative to the fuel and as a function of ρ_{u}.

Figure 2.10 shows the resulting functions $D(\rho_{\mathrm{u}})$ for all iteration steps. The dotted line corresponds to the production of pure ^{56}Ni and marks the start of the iteration. When taking into account more realistic abundances in later iteration steps, the velocities decrease significantly. Even at the highest density, $\rho = 10^7$ g cm^{-3}, the lower velocities show that the burning is already in the incomplete regime. Towards lower density, the speed decreases further. The two “steps” that are visible in the curves correspond to the extinction of oxygen and carbon burning. Like in the case of the abundances (see Fig. 2.8) the iteration scheme for the detonation velocity converges quickly: the results of the third and the fourth iteration step are already indistinguishable in Fig. 2.10.

It is important to note that the scheme described here is only valid for low density detonations that do not reach NSE in their final states because the abundances and q-values determined from the post-processed tracer trajectories are all “freeze out” values. This means that they do not represent the NSE in the final state of the detonation (with a high percentage of lighter nuclei because of photo-disintegration reactions), but the recombined state after expansion. Due to recombination, the mass numbers and q-values become again larger during the freeze-out from NSE.

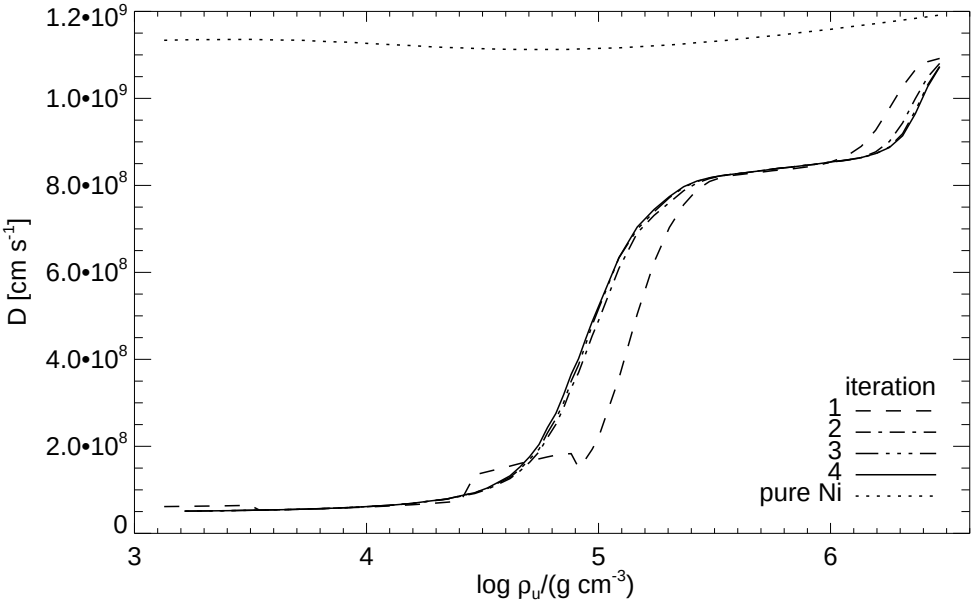

Figure 2.10.: Chapman–Jouguet detonation speeds D_{CJ} as a function of the unburnt density ρ_{u} for the low density incomplete burning regime of the C/O detonations. The speeds have been derived from the tangents to the detonation adiabats using abundances and q-values from the calibration iteration runs. The dotted line marks the pure ^{56}Ni production case, whereas the other lines mark the different iteration steps as explained in Fig. 2.8.

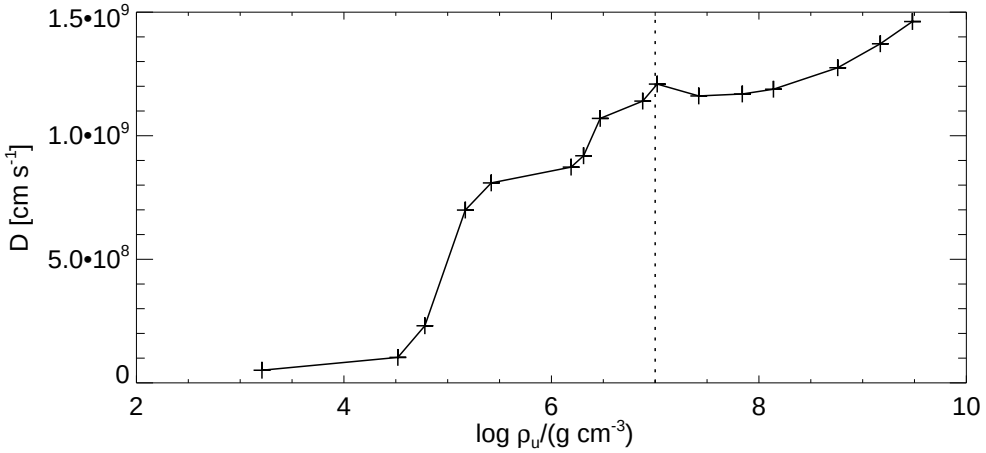

Figure 2.11.: Detonation speed table used in all hydrodynamic supernova simulations of this work including both a self-calculated part ($\rho < 10^7$ g cm^{-3}, see Fig. 2.10) and values from Gamezo et al. (1999) ($\rho \geq 10^7$ g cm^{-3}).

Therefore, for densities higher than $\sim 5 \times 10^6$ g cm^{-3}, where the photo-disintegration sets in (see Fig. 2.7), the values of Gamezo et al. (1999) have to be used. Figure 2.11 shows the entire detonation speed table, including both the self-calculated values ($\rho < 10^7$ g cm^{-3}) and the data from Gamezo et al. (1999) ($\rho > 10^7$ g cm^{-3}). It is used in all following hydrodynamic supernova simulations.

Note, that the calculation of D that is performed here for C/O detonations at low densities does not only have the advantage of avoiding numerical problems. It is also believed to be more reliable than the method applied in the helium case. There, the calculation of the sound speed in the ash state can be achieved by evaluating (2.61) and should automatically account for changes of the q-value. But, the determination of the detonation final state in the ashes is problematic in the framework of the applied detonation scheme: ash and fuel are intermixed in cells intersected by the detonation front and the front is also smeared out over several cells. Therefore, it is difficult to determine the correct location of the final state on the grid (see Eq. 2.60). Also, it is not clear if the final state is correctly represented anywhere on the grid due to the smeared out discontinuity and—at the same time—the presence of density gradients. As the upstream state can be determined more reliably, it might be advantageous to calculate detonation velocities as function of the unburnt state also in the helium burning case in future studies.

2.5.3. Consistency check

In the following, the suitability of the tables calculated in the last two sections for modeling detonations in hydrodynamic supernova simulations shall be investigated.

To this end, in the sub-Chandrasekhar simulations of Sect. 3.2, the density ρ_u is saved for every tracer particle just before the arrival of the detonation wave. Then, the reduced abundances that are determined by (2.65)–(2.69) from the post-processing are compared for all tracer particles with the calibration curves of Figs. 2.8 and 2.9 resulting in Figs. 2.12 and 2.18. This is done to probe the consistency of the calibrated mapping $\rho_\mathrm{u} \rightarrow \boldsymbol{X}^\mathrm{red}$ for the whole spectrum of simulations of this work.

C/O detonation

Figure 2.12 shows the reduced tracer abundances of the C/O-core detonations of a series of sub-Chandrasekhar models with increasing C/O-core mass (in these models the C/O detonations are ignited off-center and then spread radially outwards). The good agreement of the tracer abundances with the calibration curves gives evidence for an overall consistency of the C/O detonation scheme. However, more careful analysis shows that the more massive a model and the lower the density in ρ_u-space are, the more broadened is the tracer distribution towards lower densities. This means that there are still IGEs or IMEs produced at lower densities than in the calibration tables.

This behavior can clearly be attributed to the overdrive effect that is introduced by density gradients in the WDs (see Sect. 2.2.3), and becomes stronger at lower densities, as the strengthening of the leading shock of the detonation increases (the deviations in the plot arise from density gradients that are different from those in the calibration run). The overdrive effect is more prominent in the more massive models (for model parameters see Table 3.1) due to steeper density gradients. This is illustrated in Fig. 2.13 that shows the radial density decrease between $\rho = 10^7$ and 10^6 g cm^{-3} in the hydrostatic initial models.

The spread of the mass fractions with ρ_u is found to be an asymmetry effect that is caused by the off-center C/O ignition of the sub-Chandrasekhar supernova simulations. Detonation waves with different propagation directions traverse different path lengths with decreasing density (or even some with increasing density) before their extinction. Thus, the shock strengthening is anisotropic. Figure 2.14 illustrates this by showing the IME abundance of tracers for Model 3 with a color coding that indicates the angular position of the particles in the initial model (the detonation ignition point is shown in the little figure to the left as thick black dot). Clearly, the particles that are initially in the northern hemisphere burn to IMEs already at lower ρ_u than those in the south, as the detonation shock has a longer way to strengthen before it reaches a particle there.

Helium detonation

The helium detonation results are in general less consistent than those of the C/O detonation (see Fig. 2.18). This is due to significant differences in the setup of the supernova shell detonations from the fiducial spherical explosion in the

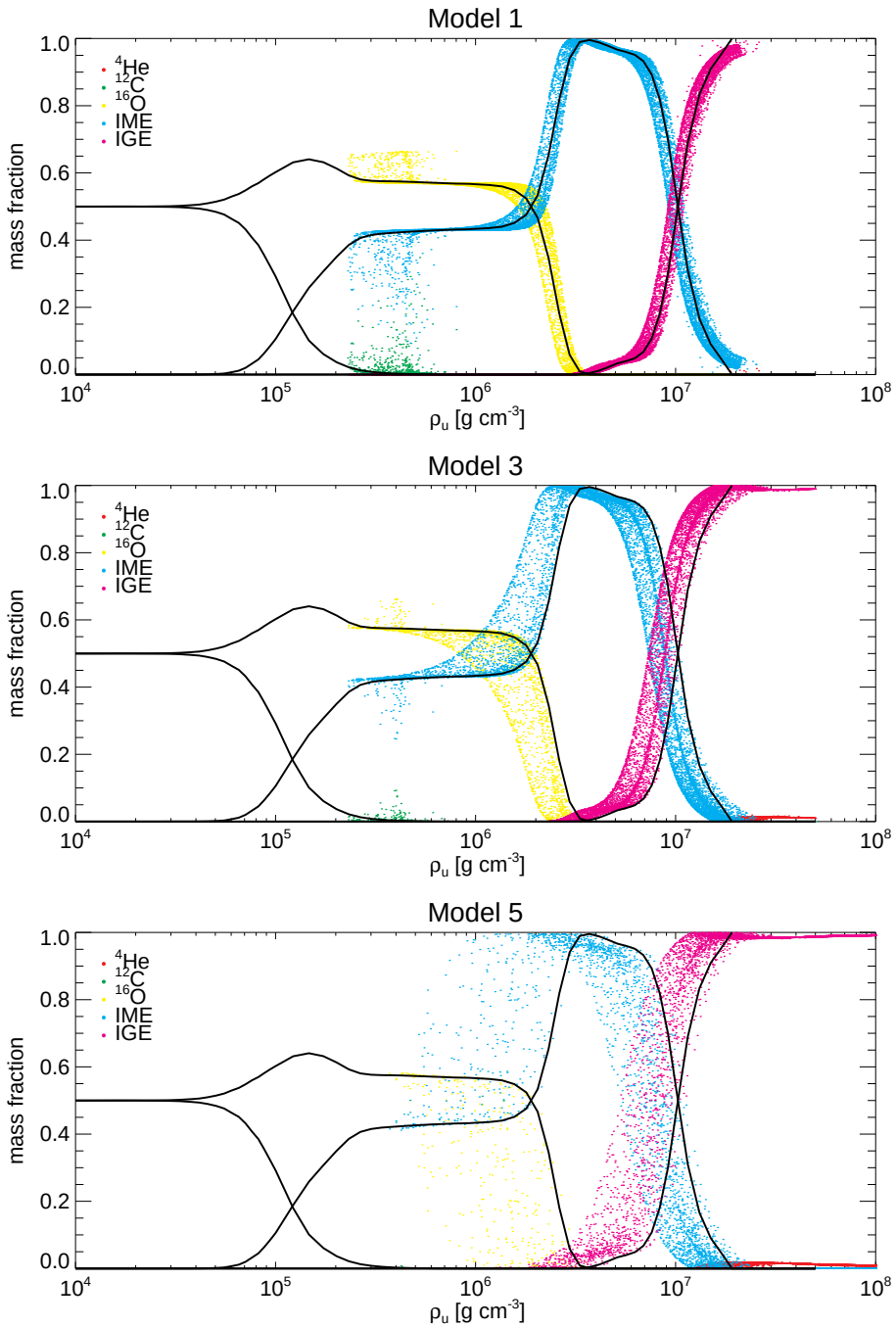

Figure 2.12.: Final post-processing abundances of all tracer particles versus fuel density ρ_u in the C/O detonations of Models 1, 3, and 5 of Sect. 3.2. The abundances have been reduced according to (2.65)–(2.69). Black solid lines show the mass fractions of the calibration table (see Sect. 2.5.1).

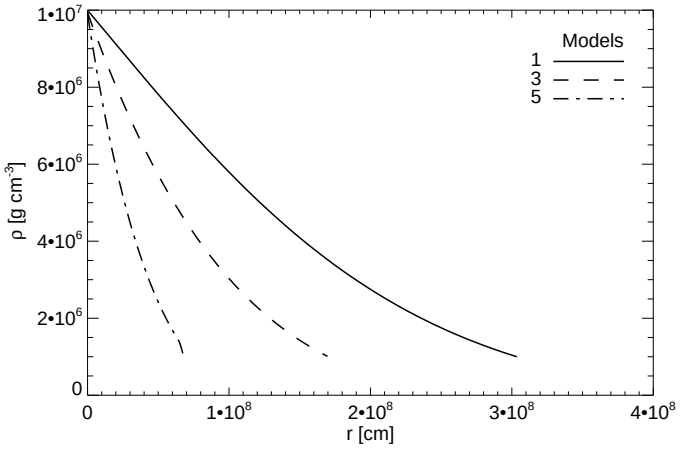

Figure 2.13.: Radial density decrease between $\rho = 10^7$ and 10^6 g cm^{-3} in the initial configuration of Models 1, 3, and 5.

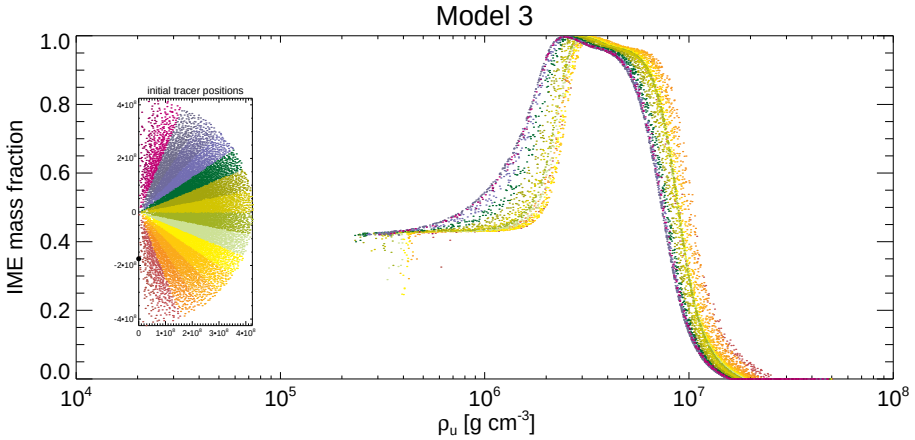

Figure 2.14.: Final IME abundances of Model 3 as in Fig. 2.12. The colors indicate the angular position in the initial tracer distribution (little plot on the left). The ignition point of the C/O detonation is indicated in the initial distribution as thick black dot.

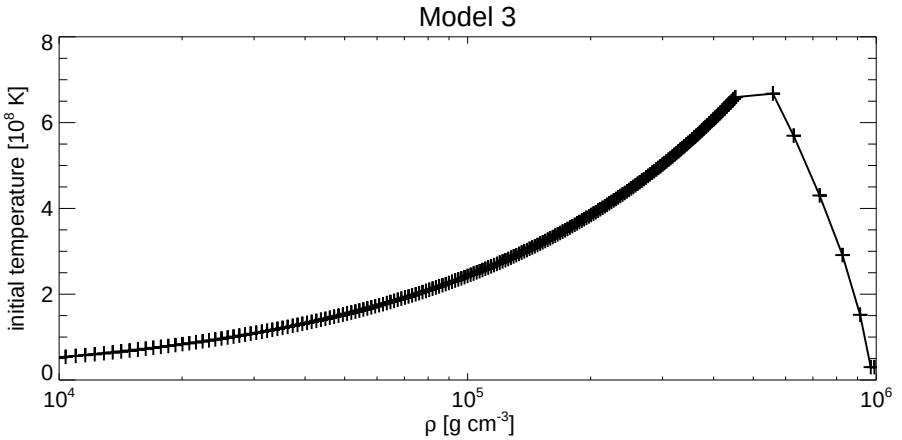

Figure 2.15.: Initial radial temperature distribution in the shell of Model 3. Crosses indicate the grid cells (the shape at the maximum is due to the abrupt density decrease at the core–shell interface).

calibration runs of Sect. 2.5. While the shell detonations of the models are ignited in a single point and then propagate in lateral direction around the core, the fiducial detonation spreads radially outwards. Moreover, the temperatures in the accreted shells of the models are much higher (6.6–7.1 $\times$ 10^8 K at maximum, see Fig. 2.15, showing the temperature in the shell of Model 3) than those in the cold fiducial WD (3×10^7 K).

To analyze the influence of the above differences separately, in a numerical experiment, the effects of the high temperatures have been suppressed in the post-processing of Model 3. To this end, the nuclear network calculations were only started at the arrival of the detonation shock. From then on, the initial temperature does not play a role anymore. Results are shown in Fig. 2.16: the burnt amount of helium and thus the q-value are roughly consistent with the tabulated values; only at the highest ρ_u, somewhat less material is burnt and the q-value will be lower than in the calibration results. However, apart from the overall consistency in the amount of burnt matter, at all densities lower mass numbers seem to be produced, shifting some of the IGEs in the calibration table to the IME group. Since roughly the same amount of α-particles are processed, the amount of triple-α reactions must have been increased on cost of the number of α-captures on the carbon seed nuclei.

The above change in nucleosynthesis can be attributed to the dynamics of the single-point ignited helium shell detonation, which differs significantly from that of the fiducial spherical detonation. Contrary to the spherical case, the strength of the leading shock wave does not increase, when it propagates in the lateral direction at approximately constant density. Thus, both maximum densities and temperatures are significantly lower than in the spherical calibration runs (see

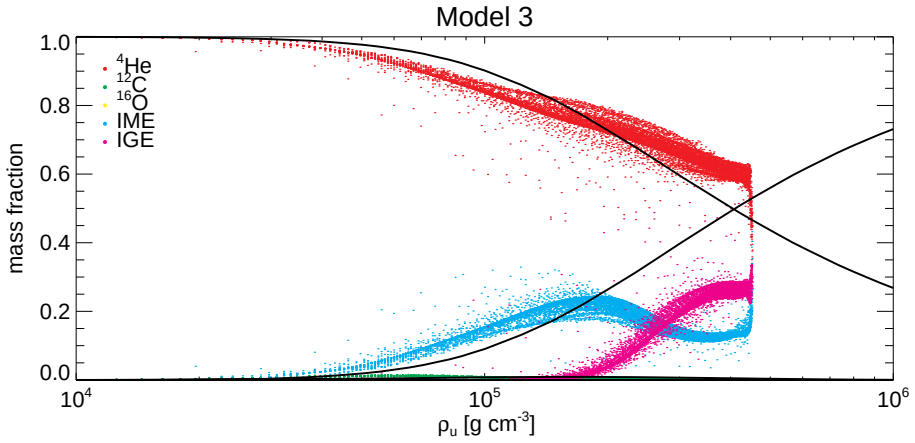

Figure 2.16.: Final tracer abundances of the helium detonation in Model 3 with suppressed initial triple-α volume burning in the post-processing. For details see the caption of Fig. 2.12.

Fig. 2.17). As discussed in Sect. 2.2.3, at $T \gtrsim 5 \times 10^8$ K the triple-α rate depends only weakly on T and declines proportional to ρ^{-2}. Contrary to this, the α-capture rate declines very rapidly with decreasing T and is proportional to ρ^{-1}. Thus, the α-capture rate will decrease more than the triple-α rate when compared with the calibration run, just as needed to explain the above nucleosynthesis results (cf. also Fig. 1 of Khokhlov 1984).

A secondary effect in this context is that spherically and laterally propagating detonations have different expansion dynamics behind the front. This may also have some influence on the details of the nucleosynthesis as the steady detonation widths are already macroscopic ($\gtrsim 10^8$ cm; Khokhlov 1989) at the low densities $<10^6$ g cm^{-3} in the helium shells.

Now, the high temperatures of the accreted shells shall be taken into account in the post-processing. This leads to an increase of mass numbers above $\rho \sim 10^5$ g cm^{-3} (where $T \gtrsim 2 \times 10^8$ K) and makes the results more consistent with the calibration tables there (see Fig. 2.18, middle panel). These changes originate from an initial triple-α volume burning that takes place before the arrival of the detonation wave. At the highest densities, however, this volume burning effect leads to a significant overproduction of IGEs with respect to the calibration table. Much more helium is burnt there reaching at maximum even complete consumption of the fuel.[4] This also corresponds to a significantly higher q-value, leading to some inconsistencies between the post-processing and the hydrodynamic simulations that do not take into account the volume burning.

Regarding the whole series of models in Fig. 2.18, the lighter Model 1 with a

[4] A larger number of carbon seeds and a smaller number of remaining α-particles reduces the triple-α rate and changes the reaction balance again in favor of more α-captures.

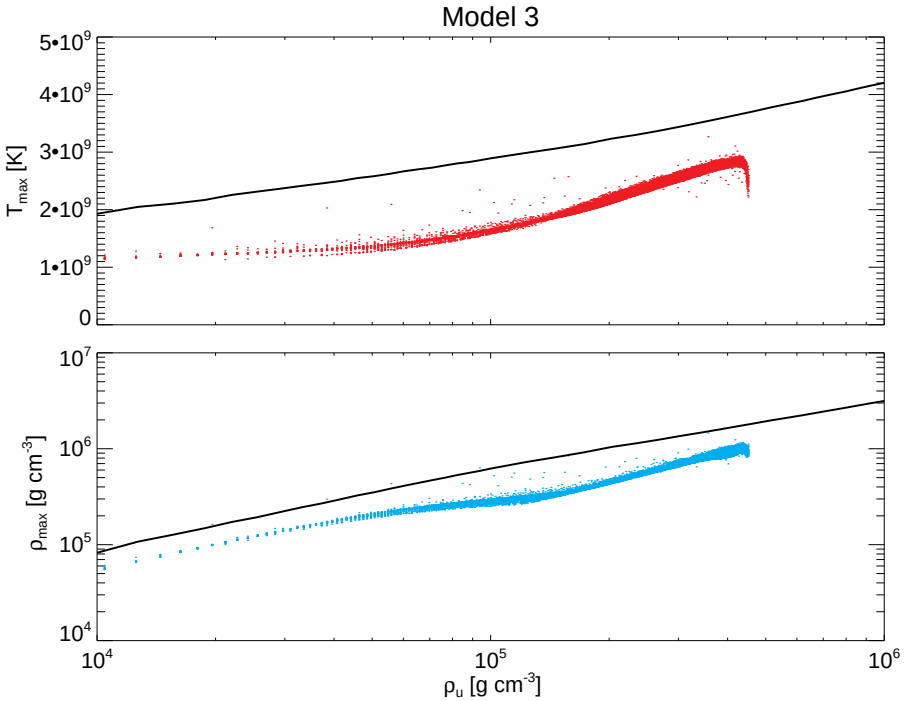

Figure 2.17.: Maximum tracer temperatures and densities in the helium detonation of Model 3 (points) and in the final calibration run of Sect. 2.5.1 (solid lines).

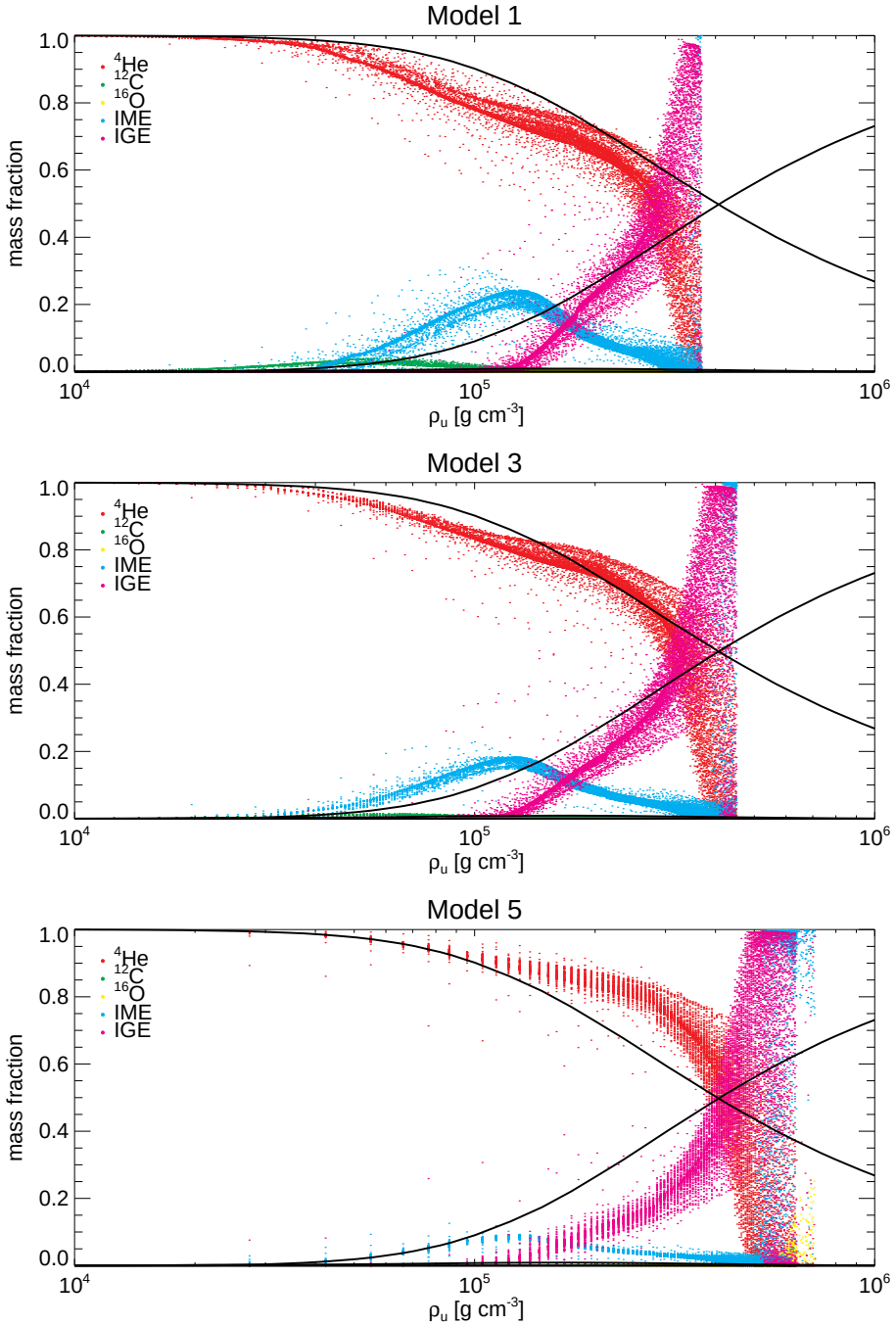

Figure 2.18.: Final tracer abundances of the helium detonation in Models 1, 3, and 5 with initial triple-α volume burning in the post-processing. For details see the caption of Fig. 2.12.

more massive shell and the heavier Model 5 with a less massive shell show results that are qualitatively similar to Model 3. However, if the inner part, where volume burning dominates, is excluded, there is a slight trend to a lower degree of burning towards the more massive models. This is seen in the increase in unburnt helium and can be explained by faster expansion (or shorter dynamical time scales) of the thinner shells. The dynamical time scale is defined by

$$t_{\mathrm{dyn}} = \frac{H}{c_{\mathrm{f}}}, \tag{2.71}$$

where $H = P/\rho g$ is the pressure scale height and $g = \mathcal{G}M_r/r^2$ is the gravitational acceleration at radius r for an enclosed mass M_r (cf. Bildsten et al. 2007). Within the series (see Table 3.1) the core mass increases at decreasing core radius, while ρ, p, and the sound speed c_{f} at the base of the shell are roughly constant. Therefore, the gravitational acceleration g at the base of the shell becomes stronger and H and thus t_{dyn} decrease.

2.5.4. Concluding remarks

In the last section it was shown that the calibration of the simplified scheme of Sect. 2.4.2 allows for consistently modeling detonations, although there remain some problems especially in the case of the helium detonation. Therefore, some possibilities for improving the current scheme are discussed here.

For the helium detonation, it would be advantageous in future studies to depart from the discontinuity approximation and to include a (small) nuclear network in the hydrodynamics code. At the low shell densities of the currently favored sub-Chandrasekhar models, the detonation structure would be resolvable. Such a scheme would ensure a correct energy release and could help to consistently treat volume burning effects in hot shells, changes of the shock strength, and expansion behind the front. Due to resolving the reaction zone structure, also the potential overestimation of temperature peaks that might be caused by the instantaneous energy release of the current scheme would be avoided. Most of these changes may lead to somewhat lower temperatures and thus IGEs in the helium detonation.

Preliminary, also a calibration of the current scheme to more realistic initial compositions (with carbon intermixed to the helium) could improve the helium detonation model. This would allow for taking into account the above mentioned triple-α volume burning in a more consistent way. The calibration of future helium detonation tables should, however, be performed with laterally propagating setups, to avoid the above overestimation of the shock strength. Such an overestimation may be a problem in general in one-dimensional simulations.

Finally, when considering the approximately correct q-values in the detonation tables and the fast convergence behavior of the iterative calibration calculations of Sect. 2.5, the simplified detonation schemes for C/O and also helium are believed to efficiently produce sensible results in all following simulations.

3. Double-detonations of sub-Chandrasekhar-mass white dwarfs with minimum helium shell masses

In the double-detonation sub-Chandrasekhar model, a detonation in an accreted helium shell causes a secondary detonation of a C/O-WD core. This happens at a total mass below the Chandrasekhar limit and can lead to a wide range of possible explosion strengths. As mentioned before, this scenario may explain Type Ia supernovae in a pure detonation model because at the low densities in sub-M_{Ch} WDs a significant amount of IMEs can be produced (see Fig. 1.1 a). However, the IGEs arising from the helium shell detonation have found to be in conflict with observed early spectra (Höflich & Khokhlov 1996; Nugent et al. 1997). Therefore, in this study, the robustness of the triggering of a secondary core detonation is explored in two-dimensional hydrodynamic simulations for *minimum helium shell masses that may detonate* (Sect. 3.2). Since in all models core detonations are triggered robustly and successful explosions ensue, synthetic observables could be calculated by Kromer et al. (2010) and the influence of the shell explosion products can be studied even for the minimum mass case (Sect. 3.3). All results are summarized and discussed in Sect. 3.4. Before the simulations and their outcomes are described, in the following section, the sub-Chandrasekhar scenario is briefly reviewed, including also a motivation of the used minimum helium shell masses (see Sect. "Degenerate helium donors" on page 69).

3.1. The sub-Chandrasekhar scenario

In the following, the sub-Chandrasekhar scenario is reviewed starting with the physical processes that are involved in the scenario (Sect. 3.1.1). Then, the potential progenitor systems in which the scenario might be realized are listed (Sect. 3.1.2). Finally, numerical simulations that have been carried out on sub-Chandrasekhar explosions previously are briefly summarized (Sect. 3.1.3).

3.1.1. Physical processes involved in the explosion

Accretion process

All sub-Chandrasekhar scenarios consist of binary systems in which a C/O-WD primary accretes matter from a less massive donor star. The accreted material can either be helium or hydrogen, which is converted to helium by nuclear burning

once it is accreted. In both cases a helium-rich shell is formed around the C/O-WD core. This shell is heated by the liberation of gravitational potential energy at a rate (cf. e.g. Iben & Tutukov 1989)

$$\dot{E}_{\rm grav} \propto \frac{\mathcal{G} M_{\rm core} \dot{M} h}{R_{\rm core}^2}, \tag{3.1}$$

where $\mathcal{G}$ is the gravitational constant, $M_{\rm core}$ and $R_{\rm core}$ are the mass and the radius of the C/O-WD core, $\dot{M}$ is the (effective) helium accretion rate, and h is the thickness of the accreted shell. Note, that the heating rate increases with both the core mass $M_{\rm core}$ and the accretion rate $\dot{M}$. Another heating source is nuclear burning as soon as the temperatures become high enough. Part of the energy is lost by heat conduction into the core. This is particularly important for low accretion rates and thus low gravitational heating.

Shell flashes

At very high accretion rates, helium is stably converted to carbon at the surface of the accretor. However, below $\dot{M} \sim 10^{-6}\ M_\odot\,{\rm yr}^{-1}$ helium burning becomes unstable due to degeneracy effects (Iben & Tutukov 1989). Here, a certain mass of helium, $M_{\rm ign}$, has to be accreted and compressionally heated before burning starts at the hottest region. Due to the helium becoming degenerate, a thermonuclear runaway, called *shell flash*, occurs. As in degenerate matter pressure is not coupled to temperature, a temperature increase can occur without a corresponding expansion of the matter. At the same time, thermonuclear reaction rates are highly sensitive to temperature. A temperature increase therefore leads to higher nuclear reaction rates which again increase the temperature, this way causing a runaway. The flash ends when the temperature becomes high enough to lift the degeneracy and the shell expands.

Given $M_{\rm core}$ and $\dot{M}$, the mass at which a shell flash ignites, $M_{\rm ign}$, can be estimated. Using a simple one-zone model, Iben & Tutukov (1989) find

$$M_{\rm ign} = 0.0177\ M_\odot \left(\frac{R_{\rm core}}{4\times10^8\ {\rm cm}}\right)^{3.75} \left(\frac{M_{\rm core}}{M_\odot}\right)^{-0.30} \left(\frac{\dot{M}}{10^{-8}\ M_\odot\,{\rm yr}^{-1}}\right)^{-0.57}. \tag{3.2}$$

They estimate $M_{\rm ign}$ as the amount of accreted mass when the nuclear energy flux first becomes as large as the energy flux by gravitational heating. This estimate is not very accurate, but the dependence on the binary parameters is qualitatively correct: contrary to the heating rate (3.1), $M_{\rm ign}$ becomes smaller both for more massive cores and for higher accretion rates.

Detonation in the helium shell

Depending on $M_{\rm ign}$ of a shell flash, the burning can be more or less violent. In very massive shell flashes the burning takes place as a detonation. For $M_{\rm ign}$ of more than

0.1–0.2 $M_\odot$ a detonation was found to be initiated successfully by Woosley et al. (1986) and Woosley & Weaver (1994b), who performed one-dimensional simulations with their Lagrangian hydrodynamics code KEPLER. In the multidimensional case, however, smaller masses could potentially detonate already, e.g., due to initiation in the lateral direction, where density and temperature gradients could be very small (see Sect. 2.3 for the physics of detonation initiation). Also, inhomogeneities in the accretion stream could create localized hot spots in an otherwise cooler accreted shell (see Guillochon et al. 2010, who consider, however, a case of dynamically unstable accretion).

Detonation of the C/O core

Provided that a detonation of the helium is successfully initiated, there are three possibilities for the further development of the system:

1. The helium detonation *directly* triggers a secondary detonation of the C/O core when it hits the surface of the latter.
2. A core detonation is only triggered in a *delayed* manner, after shock convergence close to the center.
3. The core does not detonate at all and a short and faint "transient phenomenon" ensues.

If the helium detonation wave is strong enough when hitting the core–shell interface, it might initiate an overdriven C/O detonation there that can relax to a self-supported detonation (see Sect. 2.3). This so-called *edge-lit detonation* scenario has an increased likelihood if the helium detonation is initiated at some altitude above the base of the shell which is found to be plausible in several accretion studies: Nomoto (1982), e.g., find a temperature maximum at some altitude above the base in the shell of a model accreting at $\dot{M} = 3 \times 10^{-8}\ M_\odot\,\mathrm{yr}^{-1}$. They explain this by the gravitational compressional heating rate being higher near the surface than at the base of the shell. For their models with lower accretion rates, $\dot{M} \leq 3 \times 10^{-9}\ M_\odot\,\mathrm{yr}^{-1}$, however, they do not find this temperature inversion any more as the time scale of heat transport into the core becomes shorter than the time scale of compressional heating. In these models the temperature decreases monotonically with radius and any explosive burning will start at the base of the shell.

If no direct core ignition occurs, which is likely for thin shell explosions, the core is still shocked by the shell detonation. A *delayed detonation initiation* can ensue, when shock waves from different directions converge somewhere close to the center or slightly off-center. This was shown to work for many (however always rotationally symmetric) shell ignition geometries by Fink et al. (2007). In the small volume of convergence, the shock strength strongly increases due to surface reduction of the shrinking, approximately spherical shock front. Consequently, a hot spot develops and a detonation is likely to be initiated (cf., e.g., Livne &

Glasner 1990). This mechanism is also found to work in the simulations presented in Sect. 3.2 and is discussed there more in detail.

The third possible outcome of a helium shell detonation is the *failure of any core ignition*. In this case, no "proper" Type Ia supernova would be observed, but a fainter explosion evolving on shorter time scales (Bildsten et al. 2007; Shen & Bildsten 2009; Shen et al. 2010). These events have been termed *".Ia" supernovae* (Bildsten et al. 2007) as they are roughly one tenth as bright as normal Type Ia supernovae for one tenth of the time. It has been discussed that this scenario might be more likely if the core is an oxygen/neon (O/Ne) WD (Shen et al. 2010), as these are harder to detonate than C/O WDs due to lower reaction q-values.

3.1.2. Potential progenitor scenarios

As was already discussed in Chap. 1, Type Ia supernovae are believed to be thermonuclear explosions of C/O WDs. Oxygen/neon WDs can be excluded for the Chandrasekhar-mass scenarios, as they tend to collapse, rather than explode (cf. Nomoto & Kondo 1991). In the context of sub-Chandrasekhar-mass explosions, however, one could speculate that electron captures are not yet important at the low core densities and a collapse could be avoided. Thus, they could be candidates for Type Ia progenitors, provided that future studies prove that a detonation can form in them following a helium shell detonation. In this work, however, only the more standard C/O-WD case is considered.

Given a C/O WD, there are several possible scenarios how a helium shell could be built up and detonate:

- accretion scenario:
  - helium accretion:
    - non-degenerate helium donors (i)
    - degenerate helium donors (ii)
  - hydrogen accretion (iii)
- "merger" scenario (dynamically unstable accretion) (iv).

First, dynamically stable helium accreting scenarios are considered. They could be closely related to the so-called *AM Canum Venaticorum (AM CVn) binaries*. These are binaries with very short orbital periods ($\lesssim$70 min) in which a WD primary is believed to accrete matter from a helium-rich donor star. The donor can be a helium WD, a non-degenerate helium core-burning star, or an evolved main sequence star that after mass-loss has uncovered its helium-rich core (see Nelemans 2005, for a recent review).

(i) Non-degenerate helium donors

The systems that have traditionally been investigated in numerical studies of the double-detonation scenario are accretors with non-degenerate helium donors.

According to binary population synthesis calculations, ∼10% of the AM CVn binaries contribute to this channel (Ruiter et al. 2010). The relatively large separations between accretor and donor lead to low typical accretion rates $\dot{M} \lesssim 2 \times 10^{-7}\ M_\odot\,\mathrm{yr}^{-1}$ and to correspondingly high shell flash ignition masses $M_\mathrm{ign} \gtrsim 0.2\ M_\odot$ that are likely to detonate (see Shen & Bildsten 2009, who provide a brief review on flash ignition masses of helium accretors).

(ii) Degenerate helium donors

Bildsten et al. (2007) showed that considerably lower shell masses might already detonate in systems with fully degenerate helium-WD donors. These donor stars are expected in ∼90% of AM CVn binaries (Ruiter et al. 2010). Due to the compactness of the helium WD, these systems reach very close orbits (by gravitational wave emission) and short periods before the accretion sets in and the initial mass transfer rate is high ($\dot{M} \gtrsim 10^{-6}\ M_\odot\,\mathrm{yr}^{-1}$, see Shen & Bildsten 2009). These high accretion rates allow for significantly smaller ignition masses for shell flashes (cf. Eq. 3.2) than in the non-degenerate donor case: $M_\mathrm{ign} \lesssim 0.1\ M_\odot$. Therefore, helium burning proceeds unstably in a *series of flashes*. In the course of the mass transfer the donor mass decreases, the orbit widens, and the accretion rate decreases. Thus, more and more mass needs to accumulate on the accretor before temperatures at the base of the shell become high enough for a flash. This naturally leads to an increase in the strength of these outbursts until a *final flash* occurs (because the donor mass becomes too small for a further one). Bildsten et al. (2007) calculated these final flash masses to be between 0.02 and 0.1 $M_\odot$, and also derived minimum flash masses $M_\mathrm{ign}^\mathrm{min}$ that lead to dynamical burning and potential detonation during a flash. They found that for accretor masses $\gtrsim$0.8 $M_\odot$ flash masses reach or surpass $M_\mathrm{ign}^\mathrm{min}$ before the donor mass is depleted. This is illustrated in Fig. 3.1: the hatched region shows the last and therefore maximum flash ignition masses as a function of the mass of the WD core. The upper solid line gives $M_\mathrm{ign}^\mathrm{min}$. Flashes may initiate detonations wherever the shaded region reaches above the upper solid line.

A critical point to mention here is that the $M_\mathrm{ign}^\mathrm{min}$ values were determined by Bildsten et al. (2007) as the minimum masses of accreted shells that reach high enough temperatures at their base for the burning to become *dynamical*. The criterion for this is

$$t_\mathrm{nuc} = t_\mathrm{dyn}, \tag{3.3}$$

where t_nuc and t_dyn are the time scales of nuclear burning and dynamical expansion at the base of the shell, where it is hottest in the models of Bildsten et al. (2007). Criterion (3.3) is necessary, but *not sufficient* for the initiation of a detonation (see Sect. 2.3). Also, effects of heat conduction into the core have been neglected. Therefore, the real minimum shell masses that can detonate will most likely be somewhat larger.

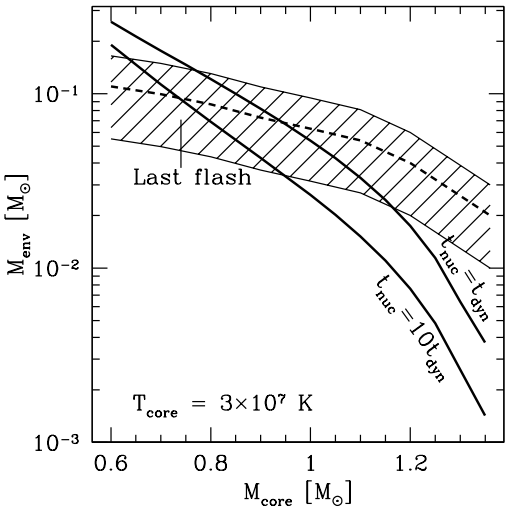

Figure 3.1.: Minimum flash masses $M_{\rm ign}^{\rm min}$ that reach dynamical burning and might detonate as a function of the WD-core mass $M_{\rm core}$ (line labeled with $t_{\rm nuc} = t_{\rm dyn}$). Also shown is the last and therefore maximum flash ignition mass (dashed line with an assumed uncertainty of 50% above and a factor of two below). This plot was taken from Bildsten et al. (2007).

(iii) Hydrogen accretion

Instead of helium accretion, hydrogen accretion might also lead to the formation of helium flashes, if hydrogen is processed to helium directly when accreted or in a series of mild hydrogen flashes. This, of course, provides an additional heating source in the shell and therefore can lead to smaller helium flash $M_{\rm ign}$. According to Piersanti et al. (2000), for accretion rates in the range of 4–10 $\times$ 10^{-8} $M_\odot\,{\rm yr}^{-1}$ hydrogen burns steadily. Due to the high temperatures of the helium shell reached by diffusive heating from the hydrogen burning shell, helium flashes have found to be triggered at low masses and to be non-dynamical (Cassisi et al. 1998).

At somewhat lower accretion rates of 1–4 $\times$ 10^{-8} $M_\odot\,{\rm yr}^{-1}$ hydrogen burns in recurrent mild flashes. According to Piersanti et al. (2000), there exists a parameter region in this regime where the effects of hydrogen burning on the temperature at the base of the helium shell below are negligible and with characteristics as if pure helium was accreted. The reason for this behavior is that at these low effective helium accretion rates (which equal the hydrogen accretion rates in the temporal average) the helium flash $M_{\rm ign}$ are quite large and the thick buffer of helium "insulates" its own base from energy injection by the hydrogen burning (Piersanti et al. 1999).

For a relatively low C/O-core mass of 0.48 $M_\odot$ and an accretion rate of 2 $\times$ 10^{-8} $M_\odot\,{\rm yr}^{-1}$, Piersanti et al. (1999) find a helium flash mass of $\sim$0.26 $M_\odot$ and

predict the flash to become a detonation by comparing the setup to the simulations of Woosley & Weaver (1994b). Studies of the possible parameter range of hydrogen accretors that can be candidates for sub-Chandrasekhar supernova models have not been published to date. Piersanti et al. (2002), however state (in their Fig. 3) that the parameters should be roughly: $\dot{M} \sim 1\text{–}2 \times 10^{-8}\ M_\odot\,\mathrm{yr}^{-1}$ and $M_{\mathrm{core}} \sim 0.5$–$0.75\ M_\odot$, but they do not give further evidence for this. As in the non-degenerate helium donor case, relatively large helium flash masses $\gtrsim$0.2 $M_\odot$ should be produced in this region and the core densities might be too low to produce significant nickel masses.

(vi) "Merger" scenario (dynamically unstable accretion)

Merger scenarios of C/O with helium WDs allow for totally different dynamics of helium accretion. Guillochon et al. (2010) have recently investigated a new potential progenitor scenario that might lead to a sub-Chandrasekhar-mass explosion: they consider C/O-WD primaries in dynamically unstable systems with helium-rich secondaries. The secondary can either be a helium WD or a He–C/O hybrid WD. In three-dimensional hydrodynamic simulations they simulate the accretion which occurs in form of a direct impact stream with rates as large as $10^{-5} - 10^{-3}\ M_\odot\,\mathrm{s}^{-1}$. This leads to a rapid accumulation of a torus of helium on the surface. Hot spots in this torus are then caused by shear instabilities in the accretion stream that is deflected and wraps around the accreted helium torus before the material settles down in the torus. Applying approximate detonation initiation criteria Guillochon et al. find helium shell detonations to be triggered in two of their systems with different donors. In one system 0.097 $M_\odot$ of helium ignite on top of a 0.9 $M_\odot$ C/O-WD, in the other 0.050 $M_\odot$ of helium ignite also on top of a 0.9 $M_\odot$ C/O-WD.

Thus, apart from the double-degenerate AM CVn systems (ii), dynamically unstable accretion in this WD merger scenario could be a second possibility that may allow for relatively low helium-shell detonation masses $\lesssim$0.1 $M_\odot$. The progenitor systems could, however, be less frequent (see next section).

Expected rates

Assuming that the above scenarios produce Type Ia supernovae one can try to predict potential contributions to the overall rate of these explosions by performing population synthesis calculations. However, as they have not been favored until recently, sub-Chandrasekhar models have not been investigated by such studies to much detail. Ruiter et al. (2009) predict Galactic rates of helium accreting C/O WDs in AM CVn systems that lead to sub-Chandrasekhar explosions up to $\sim 10^{-3}\ \mathrm{yr}^{-1}$. They only count WDs with masses of at least 1 $M_\odot$ as potential contributors, as less massive explosions could not produce enough ^{56}Ni and might be too faint. It is clear, however, that the above channels (i) and (ii) could significantly contribute to the Galactic Type Ia supernova rate of $4 \pm 2 \times 10^{-3}\ \mathrm{yr}^{-1}$ (Cappellaro et al. 1999, assuming a Milky Way-type spiral galaxy with a blue

luminosity of 2×10^{10} $L_{\odot}$).

The other two channels, (iii) and (iv), have never been taken into account by population synthesis studies. However, in both cases a significant contribution to the Type Ia supernova rate seems very unlikely. The hydrogen accretion scenario (iii) only works for a very restricted range of accretion rates and produces massive helium detonations on relatively low-mass C/O-WD cores. It is unclear whether these explosions would be bright enough to be observed as Type Ia supernovae and if the accretion rates could be maintained for long enough to accrete more than $\sim$0.2 $M_{\odot}$. Finally, in the merger scenario (iv) the dynamically unstable accretion relies on the ratio between donor and accretor mass being not too small (see Paczyński 1967). As the C/O WDs have to be more massive than $\sim$0.8 $M_{\odot}$ to produce at least some ^{56}Ni when they explode, also relatively massive helium WDs are needed. Guillochon et al. (2010) therefore merge their C/O WDs with 0.45 $M_{\odot}$ helium-WDs, which have the maximum of possible masses for such stars, and with a 0.6 $M_{\odot}$ He–C/O hybrid WD. Therefore, these models are not likely to be very frequent as the donor stars should be very rare.

3.1.3. Previous numerical simulations

Almost all previous numerical studies of the double-detonation sub-Chandrasekhar supernova scenario have assumed the explosion of relatively massive helium shells that would be the outcome of the non-degenerate helium accretion scenarios (i) and possibly the hydrogen accretion scenario (iii). The merger scenario (iv) that could allow for low mass helium detonations has only been investigated by Guillochon et al. (2010), but they did not find a secondary core detonation to be triggered. It is, however, still to be verified if this was only due to low resolution in their simulation. The minimum cell size of the study was 18 km; however, it is not clear if the C/O core was that well resolved as an adaptive mesh refinement scheme was used. A finer grid was needed to sufficiently resolve the hot spots in the cores of the study of Sect. 3.2.

The significantly smaller shell detonation ignition masses suggested by the degenerate helium accretion scenario (ii) have not been investigated yet. This is one of the main parts of this work and is presented in Sect. 3.2. Before, the main results of the work that has been done on massive shell detonations are summarized.

Of crucial importance is the mechanism of the C/O-core detonation initiation. Apart from several one-dimensional simulations, e.g. Woosley et al. (1986), successful direct ignitions of the core by the shell detonation wave have been found in the following studies in two-dimensions: Dgani & Livio (1990); Livne & Glasner (1990, 1991); Livne (1997); Arnett (1997); Wiggins & Falle (1997); Wiggins et al. (1998); and in three-dimensions using smoothed particle hydrodynamics (SPH): Benz (1997); García-Senz et al. (1999).

Delayed core ignitions by shock convergence were also found in some cases where the direct ignition did not work. Livne (1990) and Woosley & Weaver (1994b)

performed one-dimensional calculations and found perfect convergence, which is not surprising given the artificial symmetry imposed in their setup. However, the shock convergence mechanism was also shown to work in two-dimensional rotationally symmetric models where the helium detonation was initiated from a single point (Livne & Glasner 1990, 1991; Livne & Arnett 1995). It has been argued that single point ignition should occur more likely than whole shell ignition (e.g. Livne 1990; Arnett 1997).

As a summary, one can say that different ignition mechanisms seem to work in different parts of the ($M_{\rm core}$, $M_{\rm ign}$ or $\dot{M}$) parameter space. Direct core ignitions seem to be possible for spherical shell detonations if they start at some altitude above the base of the shell and if the cores are rather massive. According to Livne (1997), in two-dimensional simulations of point ignition scenarios there are three further possibilities. There, the helium detonation wraps around the core in the lateral direction and at its passage sends oblique shock waves into the core (see Fig. 2 of Livne & Glasner 1990). As the detonation wave has enough time to develop while moving in the lateral direction this oblique shock can grow strong enough to directly ignite the core. If the shock does not grow strong enough after the helium detonation is fully developed, it can still become stronger when the surface detonation converges at the opposite side of its starting point (see also Forcada et al. 2006; Forcada 2007) and cause a core ignition there. Due to the surface reduction of the leading front, the helium detonation can become overdriven. Consequently, the oblique shock that is sent into the core is also amplified.

However, direct ignition scenarios have not been shown to be very robust in numerical simulations: Livne & Arnett (1995), e.g., find the critical conditions for C/O detonations (see Sect. 2.3) to be only marginally met and Benz (1997) report a resolution dependency in their direct detonation initiations. Thus, it might be that all such direct ignition scenarios fail. In this case, the off-center convergence of the shocks sent into the core still can create a hot spot there. Fink et al. (2007) recently found that for generic 1 $M_\odot$ models with shell masses of 0.1 and 0.2 $M_\odot$ performed in rotational symmetry and different helium ignition geometries this mechanism triggers a secondary C/O-core detonation extraordinary robustly, provided that the core is resolved well enough. Therefore, here, this scenario is further investigated for a series of models with significantly smaller helium shell masses $\lesssim$0.1 $M_\odot$.

3.2. Minimum shell mass models

The double-detonation sub-Chandrasekhar scenario hinges on two critical points—first the formation of a detonation in the helium shell and second whether a successful detonation of the helium shell can detonate the core. Here, the second question is investigated. In the simulations presented in the following, the minimum helium shell masses, $M_{\rm ign}^{\rm min}$, calculated by Bildsten et al. (2007) are used. These shell masses are significantly smaller than in previous studies. Since it may still

Table 3.1.: Parameters of the initial models. $\rho_{\mathrm{c},7}$ denotes the central density in units of 10^7 g cm^{-3}, $\rho_{\mathrm{b},5}$ is the density at the base of the helium shell in units of 10^5 g cm^{-3}, and $T_{\mathrm{b},8}$ is the temperature at the base of the shell in units of 10^8 K; M_{tot}, M_{core}, and M_{sh} are the masses of the WD, the C/O core, and the helium shell, respectively. All masses are given in solar masses.

Model	1	2	3	4	5	6
M_{tot}	0.936	1.004	1.080	1.164	1.293	1.3885
M_{core}	0.810	0.920	1.025	1.125	1.280	1.3850
M_{sh}	0.126	0.084	0.055	0.039	0.013	0.0035
$\rho_{\mathrm{c},7}$	1.45	2.4	4.15	7.9	28	140
$\rho_{\mathrm{b},5}$	3.7	4.0	4.5	6.1	6.4	8.7
$T_{\mathrm{b},8}$	6.6	6.7	6.7	6.8	6.95	7.1

lead to a core detonation even for shocks too weak for the edge-lit case, the above mentioned delayed mechanism for core ignition is examined in the models. This section describes the explosion scenario (Sect. 3.2.1), the setup, and the results of the numerical simulations (Sects. 3.2.2 and 3.2.3), and finally discusses some key observational aspects of the models and also some uncertainties (Sect. 3.2.4).

3.2.1. Explosion scenario

Initial models

The initial models of this study are WDs with a composition of ^{12}C and ^{16}O (equal parts by mass) with minimum accreted helium shell mass $M_{\mathrm{sh}} = M_{\mathrm{ign}}^{\mathrm{min}}$ that *may* lead to a detonation, as calculated by Bildsten et al. (2007) (see "(ii) Degenerate helium donors" on page 69). They were constructed as follows: given the central density ρ_{c}, the constant core temperature $T_{\mathrm{core}} = 3 \times 10^7$ K, and the density and temperature at the base of the helium shell, ρ_{b} and T_{b}, at the instant when burning becomes dynamical (provided by Bildsten and Shen, private communication), hydrostatic equilibrium was integrated using the same equation of state as in the hydrodynamics code (see Sect. 2.4.1). The equation of state differs slightly from Bildsten et al. (2007), e.g. it does not include Coulomb corrections to the ion pressure. Therefore, the core and shell masses differ slightly from that used by Bildsten et al., but this should not change the main properties of the explosion dynamics.

The most important parameters of the initial models are given in Table 3.1. Any potential enhancements of the chemical composition due to the metallicity of the progenitors are neglected. In the shells an adiabatic temperature decrease towards the outer layers is assumed (see Fig. 2.15). The core masses M_{core} range from $\sim$0.8 $M_\odot$ for Model 1 to nearly the Chandrasekhar mass for Model 6. As already mentioned, the shell masses M_{sh} are set to $M_{\mathrm{ign}}^{\mathrm{min}}$. The density at the base of the

shell varies only moderately between 3.7 and 8.7×10^5 g cm^{-3}.

Detonation initiation

In all models, the helium shell is ignited in a single point at its base. As the simulations are carried out in two-dimensional rotational symmetry, the ignition spot is placed on the positive z-axis of the cylindrical coordinate system. This one-point ignition scenario introduces an asymmetry which makes it harder to trigger a core detonation than in symmetric shell-ignited models (Fink et al. 2007). But, as mentioned before, it has been argued that the one-point ignition configuration is more probable (see Sect. 3.1.3).

The detonations in the helium shell and in the WD core are tracked with two separate level set functions (see Sect. 2.4.2). The helium detonation is started by hand by setting the first level set function to positive values in a volume of choice at the base of the shell. Since dynamical burning is a necessary but not sufficient criterion for the initiation of a detonation, the formation of the helium detonation is a fundamental assumption in the models.

After shell ignition, the WD core is scanned for "hot spots" arising from the shock exerted on the core by the helium detonation. If a sufficiently large volume becomes hot and dense enough, a C/O detonation is initiated by setting the second level set function to positive values in this whole volume. To prevent grid geometry effects on the flame, every hot cell initiates a burning bubble with a radius of three cells around it. To decide when to initiate the detonation, critical densities and temperatures given in literature are used (Niemeyer & Woosley 1997; Röpke et al. 2007b; see Tables 2.1 and 2.2 and Sect. 2.3). These detonation initiation criteria, which are based on the assumption of spherically symmetric linear temperature gradients extending into unburnt fuel, are limited by some inherent uncertainties. Seitenzahl et al. (2009), e.g., point out that the functional form of temperature and density gradients of the hot spot significantly affects the critical detonation initiation conditions. Furthermore, the process depends on the composition of the fuel, the background temperature and local velocity fields[1]. Since the critical length scales pertinent to detonation initiation are generally much smaller than the grid resolution, addressing these details is currently impossible in full-star simulations. However, the detonation initiations in this work are fairly robust: the applied critical temperatures and densities are significantly exceeded (see Table 3.2). Fully resolved calculations of the detonation initiation conditions are expected to only moderately change the critical conditions. Thus, the conclusions of this study should hold despite these uncertainties.

[1] For such effects, volume burning behind the converging shock wave would have to be accounted for, but this is not yet implemented in the code.

3.2.2. Numerical simulation

Numerical simulations are carried out in two dimensions with the Eulerian hydrodynamics code and the level-set based scheme for modeling detonations described in Sect. 2.4. As mentioned before, two separate level-set functions are used to model helium and C/O detonations independently (see Golombek & Niemeyer 2005). After a hydrodynamic simulation, more accurate nucleosynthetic yields are calculated in a post-processing step (see Sect. 2.4.3).

In order to track the expanding WD during the explosion, a co-expanding uniform grid as in Röpke & Hillebrandt (2005), and Röpke (2005) is used. The expansion of a fixed mass shell is followed. To resolve the shock convergence arising from the helium detonation, for Models 1–3 the grid is kept static until the end of helium burning and for Models 4–6 it is kept static until the onset of C/O detonation. In some of the simulations (Models 4–6) exponentially growing cell sizes (see e.g. Reinecke et al. 2002b; Röpke et al. 2006) are used in the outer parts of the grid in order to keep a sufficiently high resolution in the C/O WD during the helium shell detonation and successive shell expansion. All models are carried out on a 1024×2048 grid assuming rotational symmetry.

3.2.3. Simulation results

In this section the main simulation results are presented. All the models behave in a characteristically similar manner. Therefore, the discussion focuses on Model 2 ($M_{\mathrm{core}} = 0.92$, $M_{\mathrm{sh}} = 0.084\ M_{\odot}$) as a detailed example, but the other models are also discussed where appropriate.

Explosive evolution

Starting from the ignition point (see top-left panel of Fig. 3.2), the helium detonation surrounds the whole core until it converges at the "south pole" at $t \sim 1.3$ s. While the detonation moves along the base of the shell, an oblique shock wave propagates into the core, converging off-center at a point on the negative z-axis at $t \sim 1.8$ s (cf. Livne & Glasner 1990; Fink et al. 2007)[2]. As can be seen in Fig. 3.2, this resembles the self-similar problem of a spherically or cylindrically converging shock wave (cf. Guderley 1942; Landau & Lifschitz 1991; Ponchaut et al. 2006), which results in strong shock compression that can be followed if sufficiently small scales are resolved. Due to self-similarity, the scales that need to be resolved to see a certain compression just become smaller if the shock from the shell detonation is weaker. However, according to numerical studies of the shock convergence and reflection problem, the maximum possible compression is limited (see Fink et al.

[2]Rotation effects that are neglected here could break the symmetry of the one-point ignition scenario if the ignition spot was located off the rotation axis. This could distort the minimum shocked volume and make a core detonation more difficult. The spherical shell ignition case and all ignition geometries that are symmetric with respect to the rotation axis should, however, not be influenced.

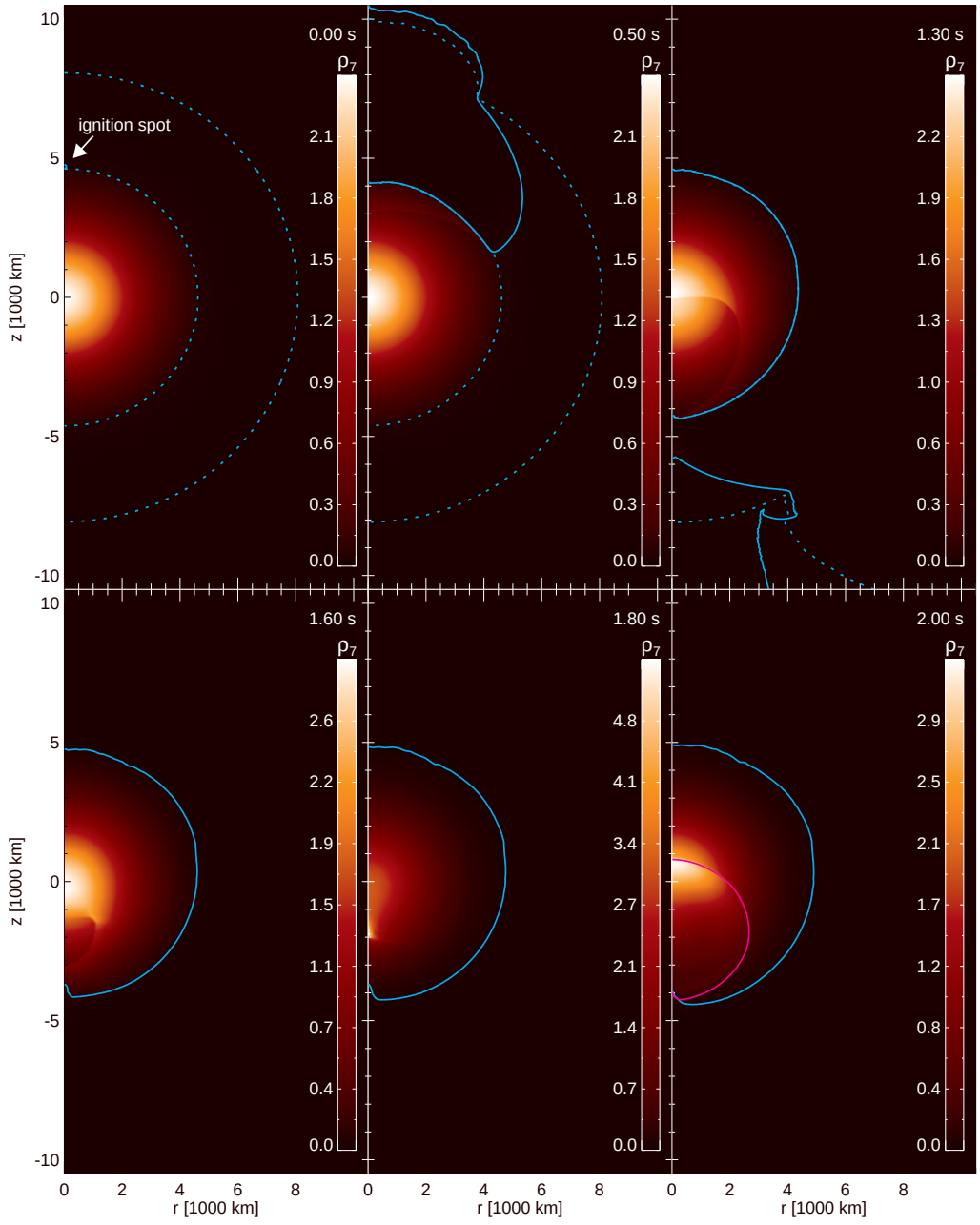

Figure 3.2.: Explosion evolution for Model 2. The density is color coded, and the solid cyan and magenta lines are the locations of the helium and C/O detonation flames, respectively. Dashed lines in cyan mark the border of the helium shell.

Table 3.2.: Conditions at core detonation initiation for all models. $t_{\rm ign}$, $T_{9,\rm ign}$, $\rho_{8,\rm ign}$, and $z_{\rm ign}$ are the time, temperature in 10^9 K, density in 10^8 g cm^{-3}, and z coordinate at the ignition spot, respectively. $R_{\rm core}$ denotes the radius of the C/O-WD core and Δ the grid resolution, which is approximately 1/1000 of the WD radius.

Model	$t_{\rm ign}$ [s]	$T_{9,\rm ign}$	$\rho_{8,\rm ign}$	$z_{\rm ign}$ [km]	$\lvert z_{\rm ign}\rvert/R_{\rm core}$	Δ [km]
1	1.94	4.62	1.08	−1910	0.39	9.86
2	1.78	4.15	1.58	−1850	0.40	8.43
3	1.58	4.42	2.24	−1750	0.41	6.81
4	1.30	4.09	1.89	−1560	0.41	5.59
5	1.00	4.14	4.63	−1370	0.46	3.86
6	0.64	3.23	8.92	−1040	0.50	2.54

2007, and references therein). The question to be addressed in this study is whether the volume at which high enough temperatures and densities for dynamical carbon burning are achieved is large enough for a detonation to form. In the simulations densities $>10^8$ g cm^{-3} and temperatures $>3.2 \times 10^9$ K were observed on resolved scales >2.5 km. The critical radius for detonation formation at these conditions, however, is only 2 m (see Table 2.1). Thus, the critical conditions for detonation initiation are met for all models, despite small shell masses. Table 3.2 lists the conditions at which the core detonations were ignited. As in Fink et al. (2007), a conservative critical temperature of 4×10^9 K was used. Thus, the given values are only a lower limit for the maximum possible compression at the given grid resolution Δ. If the detonation would have been suppressed, stronger compression would have been achieved. Only Model 6 did not surpass 4×10^9 K, despite being simulated at the highest spatial resolution. The conditions reached in the shock compression, however, were still sufficient to safely assume a successful detonation triggering. Therefore, it was ignited at this lower temperature in a second run. This model verifies that it is harder to compress the core sufficiently if the helium shell mass is low. Conversely, the high initial density of the most massive model makes a detonation easier. *Based on the approximate initiation criteria it is concluded that the limiting factor for a successful core detonation is only the successful formation of a detonation in the helium shell.*

Table 3.2 gives times and positions of the detonation initiations on the z-axis. The fact that carbon detonations occur earlier for smaller shell masses can be explained by the decrease in the core radii associated with the increasing core masses. At smaller radii the helium detonations have a shorter path around the core while the helium detonation speed at the base of the shell is roughly constant for all models. Note that the approximately self-similar nature of the problem results in the curious fact that the ignition spots of the core detonations lie at similar relative distances (0.4–0.5$R_{\rm core}$) from the center.

Now, the fiducial case (Model 2) is discussed in detail. At densities $\lesssim 4 \times$

10^5 g cm^{-3} in the helium shell, burning is relatively incomplete and NSE is not reached. The final composition is ∼63% of ^{4}He, ∼10% of IMEs, and ∼26% of IGEs (see Table 3.3). The C/O detonation starts at $t \sim 1.8$ s and at $z \sim -1900$ km and it produces 0.34 $M_\odot$ of ^{56}Ni, 0.44 $M_\odot$ of IMEs and 0.11 $M_\odot$ of ^{16}O. The structure of the ejecta at $t = 10$ s, where the simulations stop and the ejecta are close to homologous expansion, is shown in Fig. 3.3. Due to the two detonations, IGEs can be found both in the central region and in the shell. Details of the nucleosynthesis and the asymmetric structures of the ejecta are discussed in the following sections.

Nucleosynthesis

The total nucleosynthetic yields of the explosions are given for each model in Table 3.3. The upper part lists the results of the C/O core detonation, whereas the lower shows those for the helium shell detonation. Neutronization becomes important only for the highest-mass model showing 16% of IGEs that are not ^{56}Ni. This model is also peculiar in producing almost no IMEs (only ∼2% of the total mass). The NSE freeze-out is α-rich for all models with significant contributions of ^{4}He, ^{57}Ni, ^{58}Ni, and ^{60}Zn to the final composition. Fig. 3.4 shows the distribution of the nucleosynthetic products in velocity space along the equatorial axis (this is representative of the mean for the whole explosion).

A slice of Fig. 3.3 in the $z = 0$ plane gives an overview of all nucleosynthesis taking place in Model 2 (Fig. 3.5). Products of the C/O detonation are located below velocities of ∼13 000 km s^{-1}. The yields are: IGEs: 39%, IMEs: 48%, ^{16}O: 12% (see also Table 3.3). For the low central densities present in most of the models, relatively large amounts of IMEs and ^{16}O are found. However, there is almost no unburnt ^{12}C.

The helium detonation products are located at $v \gtrsim 13\,000$ km s^{-1} above the C/O detonation layers. As discussed by Bildsten et al. (2007), the burning products at those low densities differ significantly from previously published values (e.g. Khokhlov 1984, 1989). For Model 2 the most abundant nuclei are unburnt ^{4}He (63%), the IGEs ^{48}Cr (9%), ^{52}Fe (8%), and ^{44}Ti (6%), and the IMEs ^{40}Ca (4%), ^{36}Ar (4%), and ^{32}S (1%). The low-density helium burning regime is characterized by not reaching NSE and by a temperature- and density-dependent competition between triple-α reactions and α-captures. For the low initial densities in the outer shell, helium is mostly unburnt. Deeper in the shell the higher densities increase the triple-α rate leading to more burnt ^{4}He and higher maximum temperatures. Once a ^{12}C nucleus is formed, α-captures process it rapidly to higher mass numbers. Since the Coulomb barriers increase with mass number, this process stops at some maximum mass number depending on the local temperature. This leads to an inwards increase in the mean mass number, peaking roughly at ^{48}Cr or ^{52}Fe. The final yields of Model 2 in velocity space (Figs. 3.5 and 3.6) clearly demonstrate this trend. In the very innermost parts of the shell, where the initial densities are highest, the mass numbers are again lower. This is due to enrichment with carbon produced by triple-α reactions that take place before the onset of the detonation.

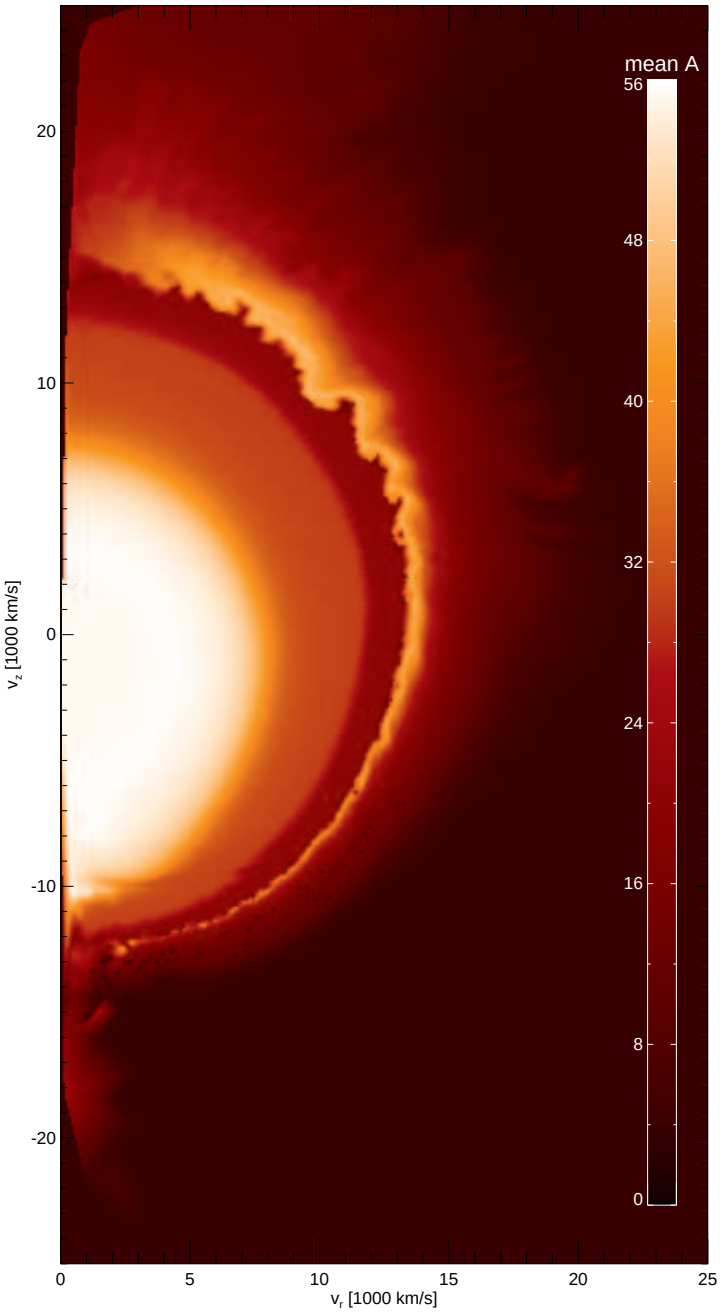

Figure 3.3.: Ejecta structure in velocity space for Model 2 at 10 s. Color coded is the mean mass number (averaged over mass: $\bar{A} = \sum_i A_i X_i$, where A_i and X_i are mass number and mass fraction of a nucleus i, respectively). The shown distribution was derived from the tracer particles after the post-processing step.

Table 3.3.: Total nucleosynthetic yields of selected species or groups of species. $M_{\mathrm{C/O,\,fuel}}$ and $M_{\mathrm{He,\,fuel}}$ are the total masses of initial fuel in the C/O core and the helium shell, respectively. For the helium detonation the values in parentheses give the fraction of an isotope mass to the total shell mass $M_{\mathrm{He,\,fuel}}$. E_{kin} is the asymptotic total kinetic energy.

Model	1	2	3	4	5	6
			C/O core detonation			
$M_{\mathrm{C/O,\,fuel}}$	8.1×10^{-1}	9.2×10^{-1}	1.03	1.13	1.28	1.39
M_{IGEs}	1.8×10^{-1}	3.6×10^{-1}	5.7×10^{-1}	8.2×10^{-1}	1.11	1.33
M_{IMEs}	4.8×10^{-1}	4.4×10^{-1}	3.7×10^{-1}	2.6×10^{-1}	1.2×10^{-1}	3.1×10^{-2}
$M_{^{56}\mathrm{Ni}}$	1.7×10^{-1}	3.4×10^{-1}	5.5×10^{-1}	7.8×10^{-1}	1.05	1.10
$M_{^{52}\mathrm{Fe}}$	7.6×10^{-3}	9.9×10^{-3}	9.6×10^{-3}	7.9×10^{-3}	4.2×10^{-3}	1.7×10^{-3}
$M_{^{48}\mathrm{Cr}}$	3.9×10^{-4}	4.6×10^{-4}	4.5×10^{-4}	3.8×10^{-4}	2.1×10^{-4}	7.1×10^{-5}
$M_{^{16}\mathrm{O}}$	1.4×10^{-1}	1.1×10^{-1}	8.0×10^{-2}	4.2×10^{-2}	3.1×10^{-2}	1.2×10^{-2}
$M_{^{12}\mathrm{C}}$	6.6×10^{-3}	4.4×10^{-3}	2.7×10^{-3}	8.8×10^{-4}	5.9×10^{-3}	7.4×10^{-4}
			Helium shell detonation			
$M_{\mathrm{He,\,fuel}}$	1.3×10^{-1}	8.4×10^{-2}	5.5×10^{-2}	3.9×10^{-2}	1.3×10^{-2}	3.5×10^{-3}
M_{IGEs}	2.9×10^{-2} (23%)	2.2×10^{-2} (26%)	1.7×10^{-2} (30%)	1.3×10^{-2} (33%)	4.2×10^{-3} (32%)	1.1×10^{-3} (31%)
M_{IMEs}	1.3×10^{-2} (10%)	8.2×10^{-3} (10%)	5.3×10^{-3} (10%)	5.7×10^{-3} (15%)	1.9×10^{-3} (14%)	7.3×10^{-4} (21%)
$M_{^{56}\mathrm{Ni}}$	8.4×10^{-4} (1%)	1.1×10^{-3} (1%)	1.7×10^{-3} (3%)	4.4×10^{-3} (11%)	1.5×10^{-3} (11%)	5.7×10^{-4} (16%)
$M_{^{52}\mathrm{Fe}}$	7.6×10^{-3} (6%)	7.0×10^{-3} (8%)	6.2×10^{-3} (11%)	3.5×10^{-3} (9%)	1.2×10^{-3} (10%)	2.0×10^{-4} (6%)
$M_{^{48}\mathrm{Cr}}$	1.1×10^{-2} (9%)	7.8×10^{-3} (9%)	4.4×10^{-3} (8%)	2.2×10^{-3} (6%)	6.8×10^{-4} (5%)	1.5×10^{-4} (4%)
$M_{^{44}\mathrm{Ti}}$	7.9×10^{-3} (6%)	5.4×10^{-3} (6%)	3.4×10^{-3} (6%)	1.8×10^{-3} (5%)	4.9×10^{-4} (4%)	6.2×10^{-5} (2%)
$M_{^{40}\mathrm{Ca}}$	4.7×10^{-3} (4%)	3.2×10^{-3} (4%)	2.2×10^{-3} (4%)	2.2×10^{-3} (6%)	6.8×10^{-4} (5%)	2.4×10^{-4} (7%)
$M_{^{4}\mathrm{He}}$	8.4×10^{-2} (66%)	5.3×10^{-2} (63%)	3.3×10^{-2} (60%)	2.0×10^{-2} (52%)	6.9×10^{-3} (54%)	1.7×10^{-3} (48%)
E_{kin} [10^{51} erg]	0.90	1.04	1.20	1.40	1.59	1.68

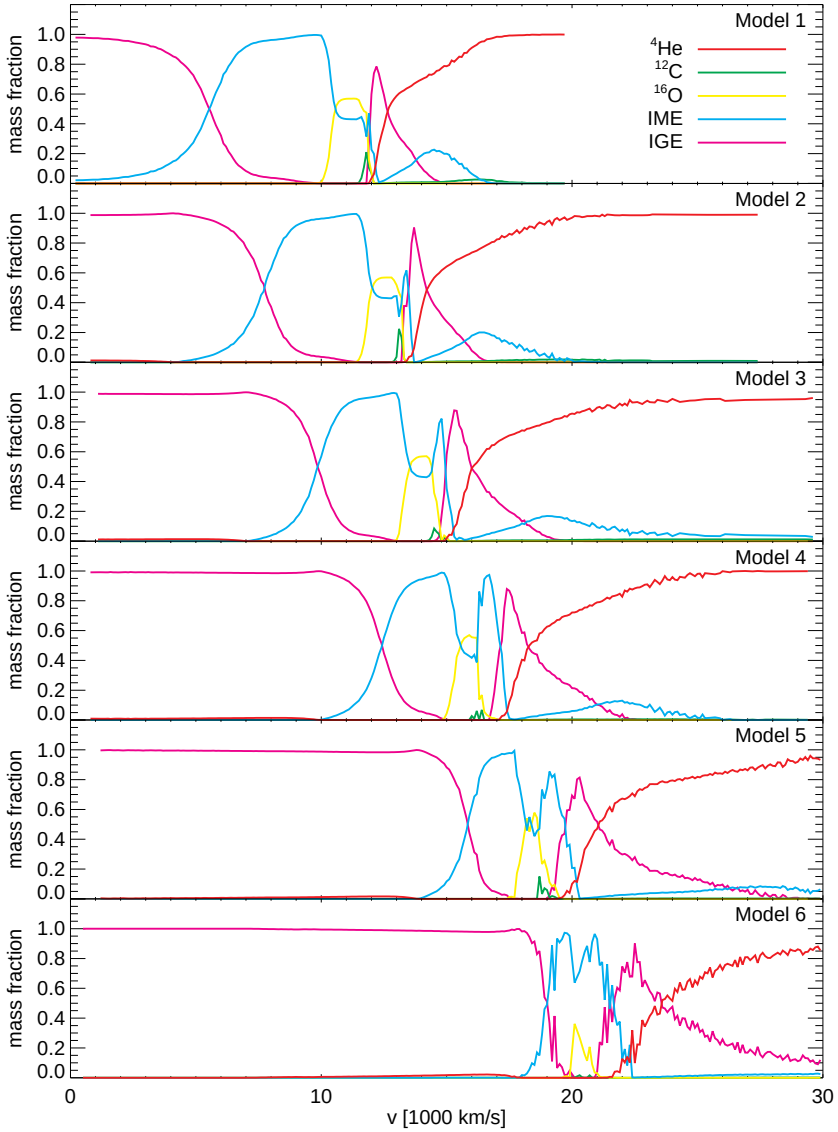

Figure 3.4.: Mass fractions of the main groups of nuclei in velocity space for all models at 10 s. Shown is the average of an angle range of $\pm\pi/32$ about the equator. The velocity bin size is 100 km s^{-1}.

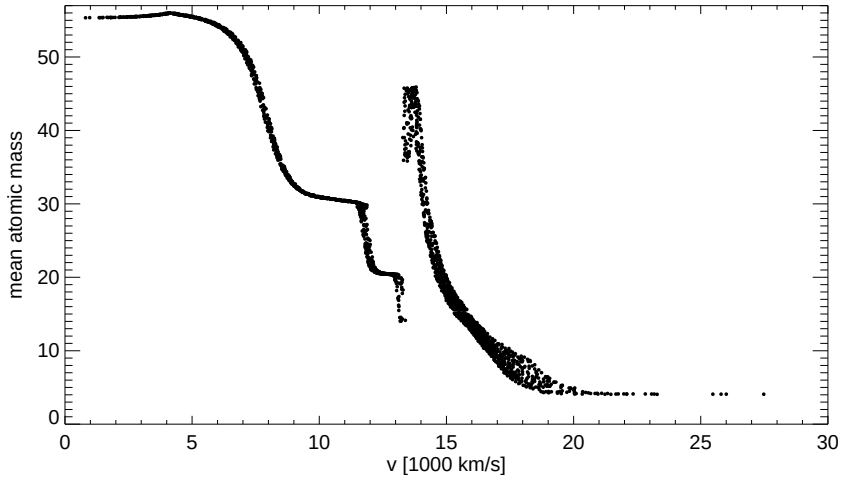

Figure 3.5.: Mean atomic mass number in the equatorial plane ($z = 0$) for Model 2 at 10 s. Points give values for individual tracer particles within $\theta = \pi \pm \pi/32$.

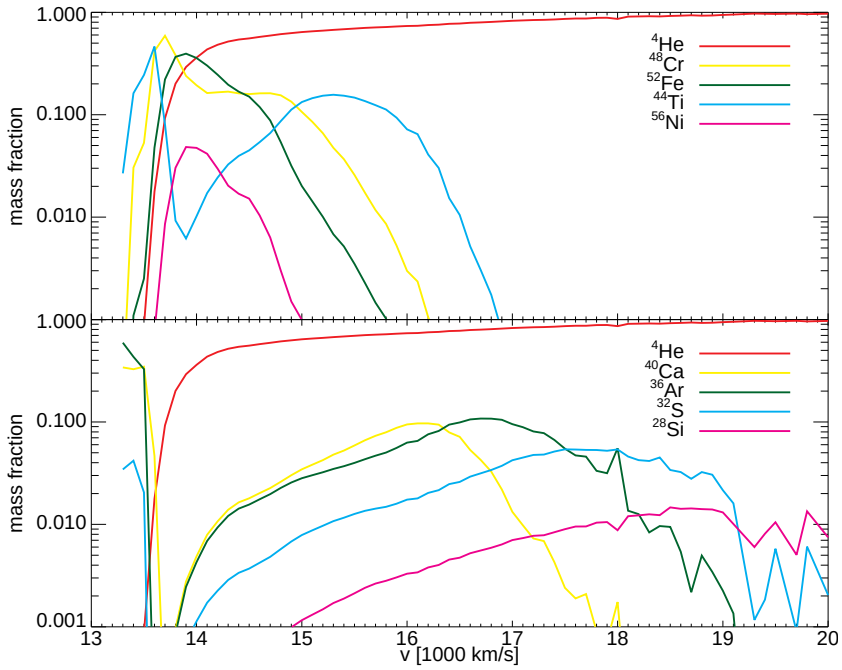

Figure 3.6.: Distribution of the isotopes in the ejecta in velocity space for Model 2 at 10 s. Shown is the average of an angle range of $\pm\pi/32$ about the equator. The velocity bin size is 100 km s^{-1}.

This occurs because of the high temperatures at the base of the helium shells in the initial models. In a mixture of ^{12}C and ^{4}He, if the carbon mass fraction $X_{^{12}\mathrm{C}}$ exceeds a value of $\frac{12}{A}$, then there is not enough ^{4}He to form nuclei with mass number A or higher by α-captures in the course of a detonation passing through this matter; e.g., for $X_{^{12}\mathrm{C}} \geq \frac{1}{3}$ one expects $A_{\mathrm{max}} \leq 36$.

The energy release due to initial triple-α burning in the hottest regions of the shell in the initial models provided by Bildsten et al. (2007) has been ignored in the hydrodynamic simulations, as they lack a nuclear network that could account for this volume burning effect. It has, however, been considered in the post-processing step. This introduces some asymmetry in the results which reflects the choice of a pure helium shell composition and single spot ignition: while the detonation wave wraps around the WD, more and more ^{12}C is produced in the remaining shell material. For Model 2, the mass fraction of initial ^{12}C that is reached at the equator by this volume burning is consistent with the minimum mass fraction values given in Shen & Bildsten (2009). Above the equatorial plane there is less initial carbon, below there is more. Therefore, the total yields of this study should be roughly consistent with that of one-dimensional shell detonations of Bildsten et al. (2007). However, significant differences are found when comparing their yields for a 0.06 $M_{\odot}$ helium shell detonation on top of a 1 $M_{\odot}$ C/O WD with Model 3, which is closest to their model: they burn ∼57% of the helium, whereas in Model 3 only about 40% are burnt. These differences arise partially due to the fact that Bildsten et al. (2007) do not take into account any initial triple-α burning and assume pure helium in the shell. More important, however, will be the differences in the shock compression between the one-point ignited laterally propagating detonation of Model 3 and the whole-shell ignited spherically propagating detonation of Bildsten et al. (2007). Both these effects are discussed in detail in Sect. 2.5.3.

Asymmetry effects

In Fig. 3.3 asymmetries in both composition and ejecta velocities of Model 2 are visible. These are quantified in Fig. 3.7, which shows the abundances of the main groups of elements averaged for three different angular ranges: 0°–45° ("north"), 67.5°–112.5° ("equator"), and 135°–180° ("south"). The main differences are:

- Helium detonation products in the north extend over a wider velocity range than those in the south. As the ejecta are already homologous to good accuracy at 10 s, this cannot change by stronger expansion of the southern ejecta. The effect is also visible in the final distribution of tracer particles shown in Fig. 3.8. As every particle represents the same mass, it can also be seen that the southern regions are denser than the northern ones. This property might be important for spectrum formation, as a wider range in velocity space increases the range of possible photon absorption frequencies.

- From north to south the amount of burnt material in the shell decreases. It is 48%, 37%, and 24%, for the northern, equatorial, and southern directions

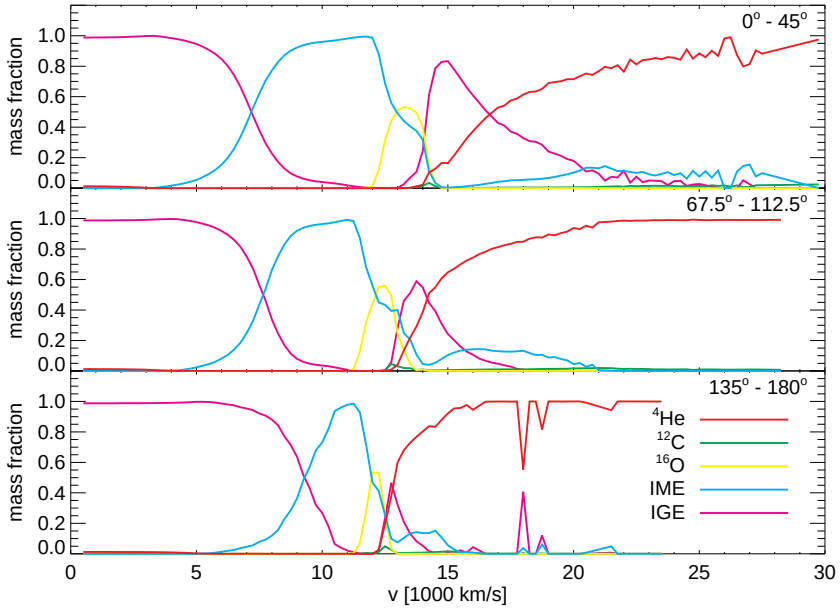

Figure 3.7.: Asymmetry of mass fractions in velocity space for Model 2 at 10 s. (Group) abundances are averaged for three different polar angle ranges and over velocity bins of 250 km s^{-1}.

of Fig. 3.7, respectively. Also the amount of synthesized IGEs is less (corresponding to lower maximum mass numbers in Fig. 3.3): it is 88%, 66%, and 51% of the burnt matter, respectively.

- At the south the C/O core has been compressed more strongly: from the top panel to the bottom panel of Fig. 3.7 the IGE abundance from the core detonation increases (30%, 36%, 55%) at the expense of IMEs (56%, 50%, 38%) and oxygen. Additionally, the outer boundary of the core ejecta is found to be asymmetric with values of roughly 14 000 km s^{-1}, 13 000 km s^{-1}, and 12 000 km s^{-1} from the north to the south.

- While the core ejecta extend to lower velocities in the south, the IGEs reach significantly higher velocities there.

- Especially in the northern hemisphere there seems to be significant mixing of unburnt carbon and oxygen from the core with IGEs from the shell detonation.

Qualitatively similar asymmetry effects appear for all other models.

The asymmetries in the core detonations can be easily understood: the off-center convergence of the helium detonation shock leads to stronger compression of the matter in the south, close to the C/O ignition point, and thus to an enhanced production of IGEs there. Asymmetries in the final velocity distribution of the core

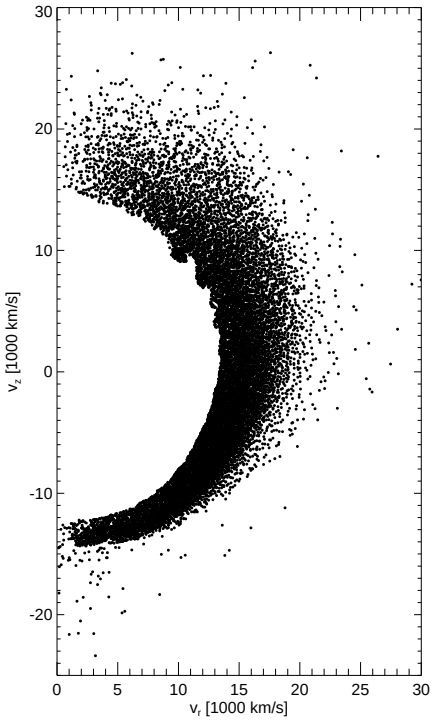

Figure 3.8.: Distribution of tracer particles in velocity space for Model 2 at 10 s. Shown are only particles which initially belong to the helium shell.

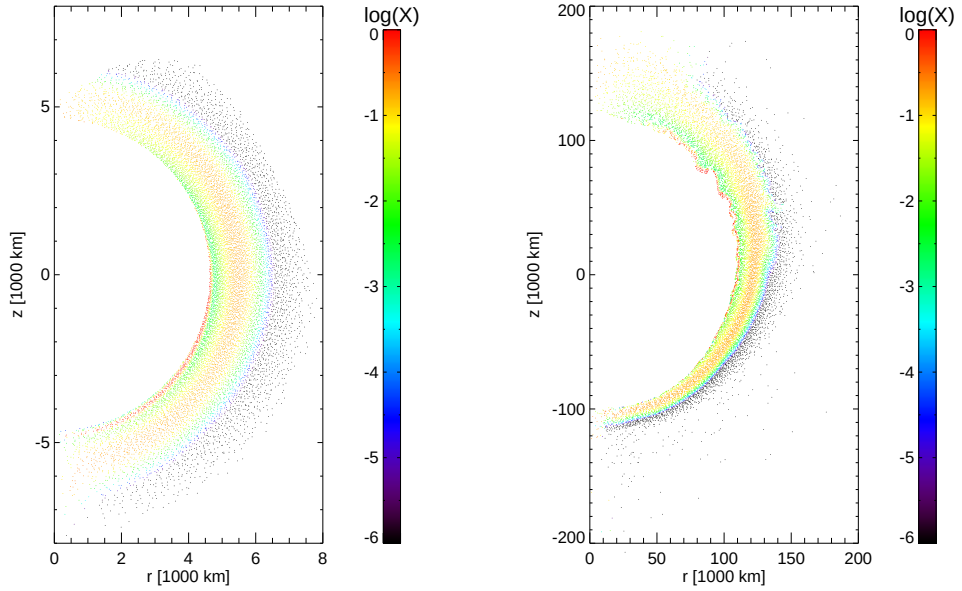

(a) $t = 0$ s (b) $t = 10$ s

Figure 3.9.: Final ^{44}Ti abundances for each tracer particle of Model 2. Shown are initial (a) and final positions (b) of particles belonging to the helium shell.

ejecta are a consequence of both asymmetric detonation initiations: the off-center C/O ignition leads to greater shock steepening (and velocities behind the front) in the north, where the detonation has a longer path down the density gradient than in the south;[3] additionally, the core detonation shock runs into less dense material in the north, as the helium detonation products started expanding earlier there due to the point-like ignition. The greater spread of the final velocities and the lower densities of the helium shell ejecta in the north are also explained by these effects.

In contrast, the reason for asymmetries in the composition of the helium shell ejecta is not obvious. To explain these, it is helpful to look at the tracer particle trajectories. Fig. 3.9(a) shows the initial positions of all tracers belonging to the helium shell. Color coded is the abundance of the final yield of ^{44}Ti. As the shell is set up in spherical symmetry and has no chance to expand before the supersonic detonation propagates through it, the overall ^{44}Ti distribution is very homogeneous. The asymmetry at the upper and upper-right boundary is only due to particles that were lost over the grid boundaries during the simulation (these are not plotted). The thin red line of enhanced ^{44}Ti abundance close to the inner boundary coincides with those parts of the hot inner shell, where initial triple-α burning limits the

[3] In northern directions the detonation first weakens as it has to move up the density gradient towards the center, but this effect is very likely negligible here.

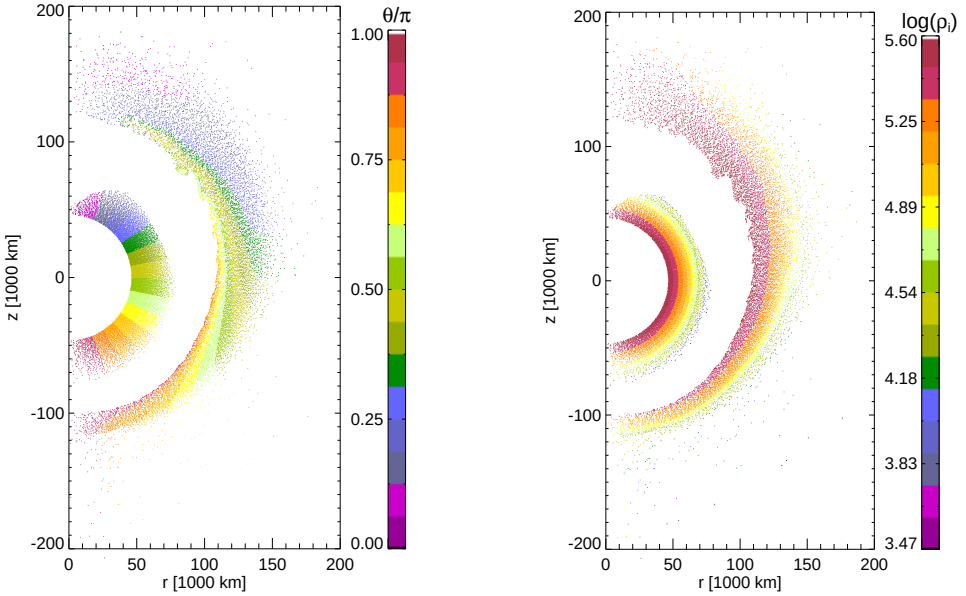

(a) initial angle (b) initial density

Figure 3.10.: Rearrangement of matter in the shell of Model 2. The outer sets give the final positions of tracer particles belonging to the helium shell, while the inner sets represent the initial locations (with coordinates multiplied by a factor of ten for clarity). Color coded are initial angle θ between particle and z-axis (a) and initial density ρ_i (b).

maximum mass numbers to $A = 44$, but this is only a minor effect. Therefore, the asymmetries in the shell nucleosynthesis, clearly, are not due to changes in the helium detonation while it propagates around the core. Fig. 3.9(b) illustrates the final asymmetries by showing the final ^{44}Ti abundances of the tracer particles at their final positions ($t = 10$ s). Keeping in mind the overall homogeneity seen in Fig. 3.9(a), this asymmetry can only stem from a rearrangement of the particles within the shell. This becomes clear when coloring the tracer particles according to their origin. The inner ring in Fig. 3.10(a) shows the initial positions of the tracers (ten times enlarged). Symbols are colored according to each particle's initial angular bin. In the outer ring the tracer colors are the same, but now the final positions are plotted. A significant rearrangement has taken place that can be explained by the asymmetry of the core ignition: the off-center core detonation first hits the shell of helium burning products close to the southern pole; when further expanding, it seems to "sweep" the inner and most burnt parts of the shell significantly further to northern directions. Therefore, the amount of burning products in the final ejecta composition is strongly increased towards the north, what is illustrated also in Fig. 3.10(b) that is similar to Fig. 3.10(a), except that the color coding shows the initial density. The shift of the high density particles to the north explains the dominance of IGEs there.

Finally, it remains to explain the vortices seen at the core–shell interface in the north. These are likely to be due to the Kelvin–Helmholtz instability arising from the shear induced when the core detonation "sweeps" the inner parts of the shell towards the north.

3.2.4. Discussion

The primary goal of this study has been to investigate whether or not secondary core detonations can be triggered for scenarios with the minimum helium shell masses of Bildsten et al. (2007). In all six simulations, C/O detonation conditions were obtained leading to a successful explosion of the WD. This implies that as soon as a detonation triggers in a helium shell covering a C/O WD, a subsequent core detonation is virtually inevitable. Some key observational aspects of the models and some uncertainties are discussed here.

Depending on the initial central density of the model, the C/O detonation produces nickel masses between 0.17 and 1.1 $M_\odot$. In principle, this range is sufficiently broad to encompass all major classes of Type Ia supernovae (cf., e.g., Stritzinger et al. 2006, for a sample of ^{56}Ni masses determined for 16 well-observed Type Ia supernovae; see also Sim et al. 2010): the high mass end of sub-luminous SN 1991bg-like events ($\sim$0.07–0.17 $M_\odot$: Model 1), normal Type Ia supernovae ($\sim$0.4–0.8 $M_\odot$: Models 2–4), and bright SN 1991T-like explosions ($\sim$0.85–1.0 $M_\odot$: Models 4, 5).

For most of the models (1–4), the C/O detonation produces a significant quantity of IMEs ($\sim$0.48–0.26 $M_\odot$), as required to account for the strong lines of e.g. silicon, sulfur, and calcium which characterize the maximum-light spectra of Type Ia supernovae. The extreme Model 6, however, makes almost no IMEs and Model 5 yields only a rather small IME mass ($\sim$0.1 $M_\odot$). This means that they are unlikely to be promising candidates to account for real Type Ia supernovae. However, they are still interesting as a demonstration that detonations of such small shell masses can still trigger a secondary detonation in a C/O-WD core.

Note that possible initial compositions favoring more oxygen (and neon) for massive WDs (cf. Domínguez et al. 2001; Gil-Pons & García-Berro 2001) are not considered here. Extrapolating from Seitenzahl et al. (2009), it can be expected that core detonations would still be triggered for a composition of 30% carbon and 70% oxygen (in mass). For compositions with significantly lower carbon fraction like in O/Ne WDs detonation criteria are not available yet. Detonation conditions and nucleosynthesis in these stars should be investigated in future studies. The concerns regarding the WD initial composition are alleviated by the fact that the ignition spots are far above the center (see Table 3.2) where the carbon fraction is expected to be higher than in the innermost region (see, e.g., Althaus et al. 2005).

The high velocity IGEs produced in the helium detonation impose an important constraint on the ability of the models to reproduce the early spectra of observed Type Ia supernovae. SN 1991bg-like objects show titanium in their spectra, but the models are too bright to fit their light curves. Normal Type Ia supernovae do not

show clear signatures of IGEs at early epochs. Similarly, although there is evidence of IGEs affecting the pre-maximum spectra of SN 1991T-like explosions (e.g. Mazzali et al. 1995), these are inconsistent with the models since the important features there are associated with iron rather than the IGEs predicted to be abundant from the nucleosynthesis calculations[4]. However, to fully address the issue of whether the presence of heavy elements created during minimum helium-shell detonations is in contradiction with observations requires detailed radiative transfer simulations and consideration of possible uncertainties in the helium-shell nucleosynthesis. Results of such simulations are discussed in the next section.

3.3. Synthetic observables

For all six models of the series presented in Sect. 3.2, synthetic spectra and light curves were calculated by Kromer et al. (2010) applying the time-dependent multidimensional Monte Carlo radiative transfer code ARTIS (Kromer & Sim 2009; Sim 2007). To complete the overview of the sub-Chandrasekhar scenario, their main results are summarized here. Most of the discussion focuses on Model 3, as it is exemplary for most other models of the series and, due to its ^{56}Ni-mass of 0.55 $M_{\odot}$, a good candidate for modeling normal Type Ia supernovae. In the following, synthetic spectra (Sect. 3.3.1), light curves (Sect. 3.3.2), and the influence of ejecta asymmetries on these observables (Sect. 3.3.3) are described. Finally, a toy model to test the consequences of an admixture of carbon to the helium shell for the observable predictions is presented (Sect. 3.3.4).

3.3.1. Spectra

The material produced in the helium shell detonation has important observable consequences. Although ^{56}Ni is not very abundant in the models, significant mass fractions are predicted for the radioactive nuclei ^{52}Fe, ^{48}Cr, and ^{44}Ti. The yields of these nuclei are given in Table 3.3 and, for Model 1, are as large as 20% of the core ^{56}Ni mass. The most important finding of Kromer et al. (2010) is that these peculiar elements crucially influence both spectra and light curves of all models. To illustrate this, the spectrum of Model 3 is shown in Fig. 3.11 at three days before B-band maximum. In the figure the thick black line is the angle-averaged model spectrum and the dark blue line is the spectrum of the (faint) normal Type Ia supernova SN 2004eo (Pastorello et al. 2007a) as a reference. The colors below the spectrum specify the mass numbers of elements responsible for emission of quanta in the Monte Carlo simulation, whereas the colored region above the spectrum gives a measure for the strength of absorption and the absorbing elements. Only elements which last removed or injected energy into a wavelength bin are counted. The most striking difference between the synthetic spectrum of Model 3 and the

[4]Note that the decay-time of ^{52}Fe is so short, ∼0.5 days, that it is expected to have almost completely decayed to ^{52}Cr before the light curve is bright.

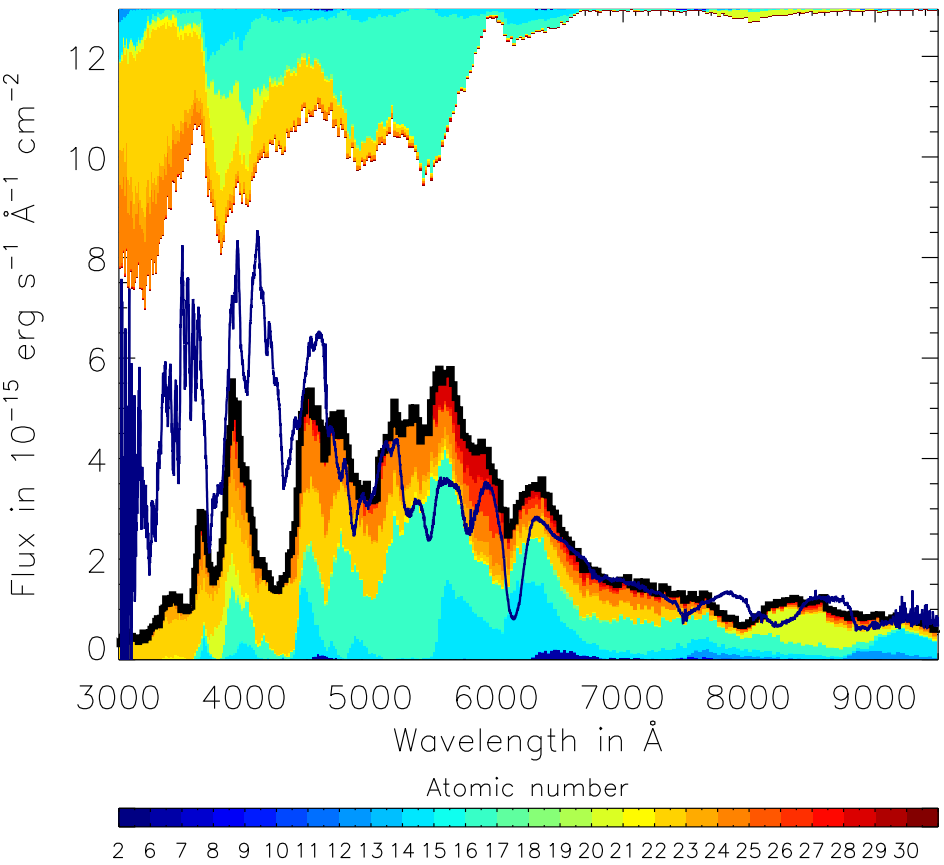

Figure 3.11.: Angle-averaged synthetic spectrum of Model 3 from Kromer et al. (2010) at three days before B-band maximum (thick black line) compared to a de-redshifted and de-reddened spectrum of SN 2004eo (Pastorello et al. 2007a, dark blue line). Colors below the spectrum indicate the relative contributions of elements that last injected energy into a wavelength bin of the radiative transport calculation. The upper part of the figure analogously shows an absorption spectrum and indicates the relative importance of elements that last absorbed energy from a wavelength bin.

observed one is the lack of flux at short wavelengths and the overproduction of flux at longer wavelengths. This is caused mostly by fluorescence of chromium and titanium which are shown in orange color in the plot. These elements have many strong lines at ultra-violet (UV) and blue wavelengths and therefore absorb a lot of flux there. The absorbed energy is then re-emitted almost over the whole displayed frequency range and thus flux is effectively transferred from the UV and the blue towards redder colors. Consequently, the whole spectrum is dominated by emission of titanium and chromium and the characteristic lines of IMEs like silicon and sulfur that are typical for Type Ia supernovae are weakened or totally "blanketed" by this radiation. For example, the Si II λ6355 feature is rather weak, due to this effect.

To provide further evidence for the influence of the shell detonation products on the spectrum, a toy model spectrum was calculated by Kromer et al. (2010) from the ejecta structure of Model 3, but with all the shell detonation material being removed ("Model 3c"). The result is shown in Fig. 3.12: without the influence of the shell the spectrum of normal Type Ia supernovae is surprisingly well reproduced by the core detonation products of the sub-Chandrasekhar-mass model. All the typical characteristic lines of IMEs are present.

Returning to the discussion of the spectrum of Model 3, an exceptional case is calcium, as it is the only IME that has a significant yield in the helium shell detonation. Therefore, it is visible in form of the Ca II near infra-red triplet at $\lambda\lambda$8498, 8542, 8662. Finally, it is remarkable that, despite the significant amount of unburnt helium in the shell, there are no prominent features of it in the spectrum. However, non-thermal excitation and ionization effects which might be important here as helium possesses highly excited states have not been included in the radiative transfer calculations.

Similar to Model 3, the helium detonation products impose important constraints on all other models of the series. However, their importance decreases for the more massive models, as they have smaller shell masses. Models 1–4 can all be excluded as candidates for normal or sub-luminous SN 1991bg-like supernovae. Their shells of 0.126, 0.084, 0.055, and 0.039 $M_\odot$ still dominate the spectra. Models 5 and 6 have only 0.013 and 0.0035 $M_\odot$ in their shells, which might be low enough for not disturbing their spectra. However, these models have other problems that exclude them as candidates for Type Ia supernovae: as mentioned in the discussion of Sect. 3.2.4, due to their very massive cores with high central densities, the C/O detonation produces almost exclusively IGEs—similar to the pure detonation Chandrasekhar-mass model (see Sect. 1.3). Thus, their IME masses of 0.12 and 0.03 $M_\odot$ are so low that the characteristic lines are not visible in their maximum spectra which are instead completely dominated by features of IGEs. This is evident in the synthetic spectrum of Model 6 at three days before B-band maximum shown in Fig. 3.13: it is dominated by red colors representing IGEs and, remarkably, it totally lacks the Si II λ6355 feature. Therefore, Kromer et al. (2010) conclude that spectroscopically none of the models is suitable as candidate for Type Ia supernovae.

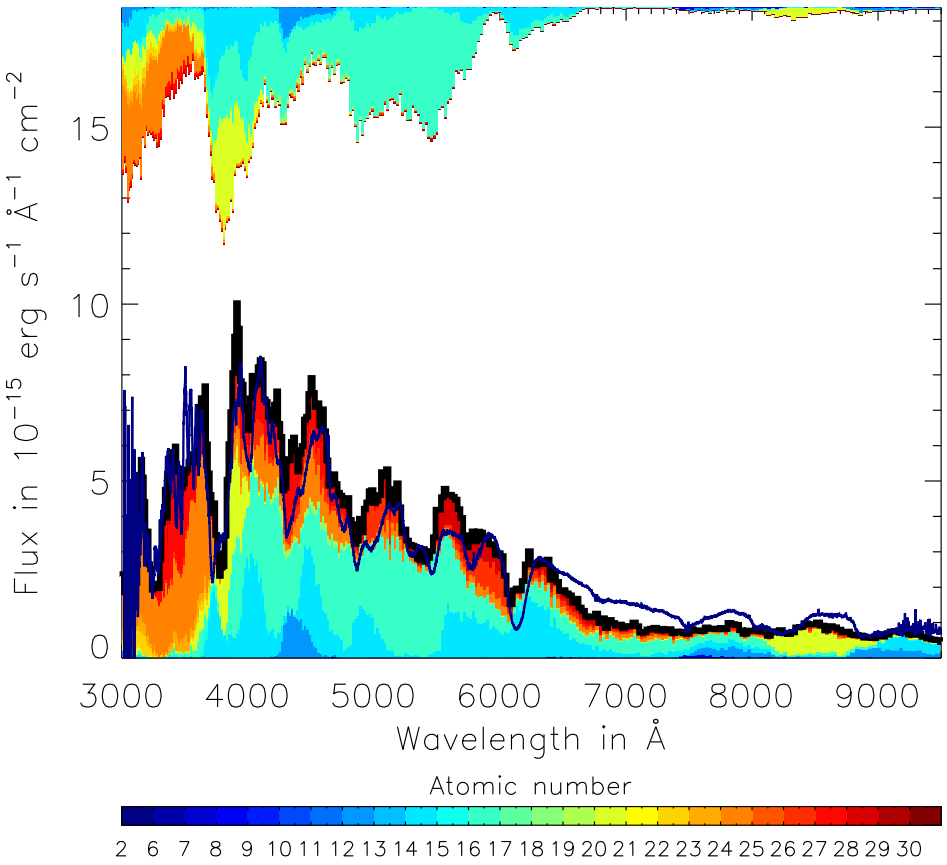

Figure 3.12.: Angle-averaged synthetic spectrum at three days before B-band maximum for toy model 3c consisting only of the core ejecta of Model 3 (Kromer et al. 2010, thick black line). The dark blue line shows the spectrum of SN 2004eo, for comparison. For further details, see the caption of Fig. 3.11.

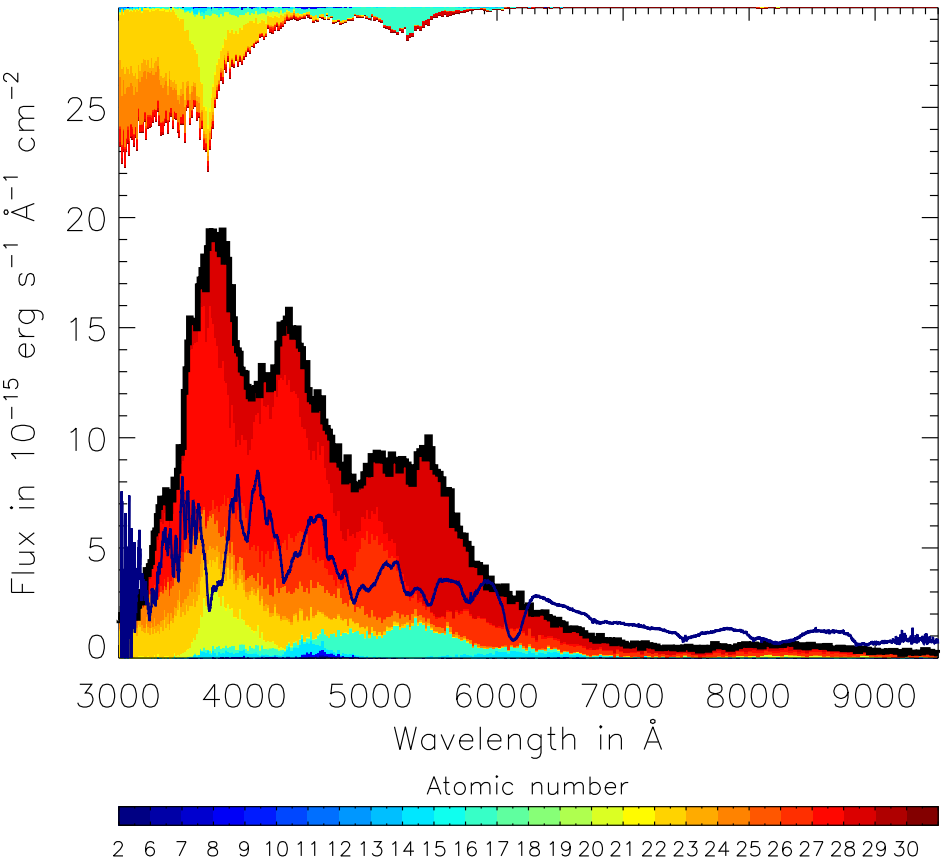

Figure 3.13.: Angle-averaged synthetic spectrum at three days before B-band maximum for Model 6 (thick black line) from Kromer et al. (2010). The dark blue line shows the spectrum of SN 2004eo, for comparison. For further details, see the caption of Fig. 3.11.

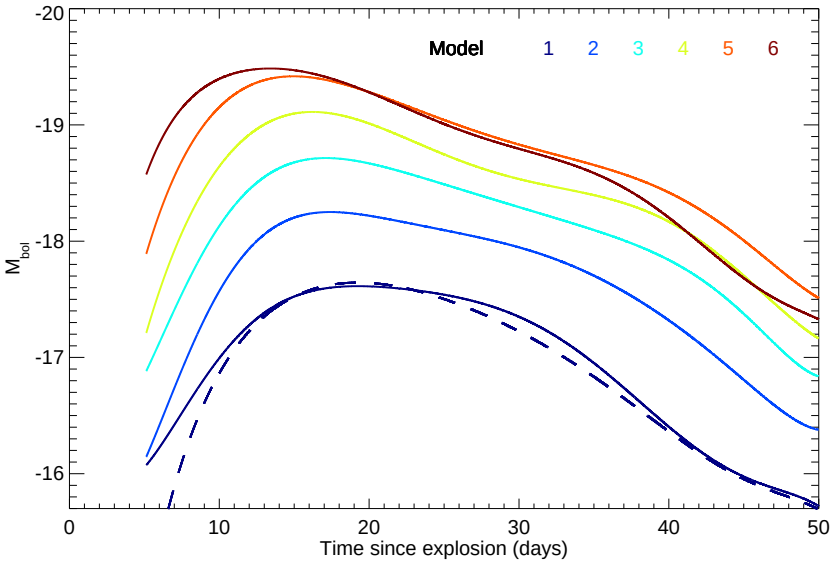

Figure 3.14.: UVOIR bolometric light curves for the models. Two light curves are shown for Model 1: the first (solid line) shows the calculation for the complete model while the second (dashed line) shows the result obtained when the contributions of radioactive ^{52}Fe and ^{48}Cr are neglected.

3.3.2. Light curves

In Fig. 3.14 angle-averaged ultraviolet-optical-infrared (UVOIR) light curves are shown for all six models (corresponding values are given in Table 3.4). The light curves illustrate not only that the peak magnitude varies significantly between the models, as expected from the differences in nickel mass, but also that there is significant diversity in both the rise times (see Table 3.4) and the post-maximum light curve shape. This diversity arises from the different distributions of the burning products in both the core and the helium shell. In particular, there is a clear trend for faster rise times in the brighter models. This occurs since, in

Table 3.4.: Rise times $t_{\rm peak}$ and peak absolute magnitudes $M^{\rm bol}_{\rm peak}$ for the UVOIR bolometric light curves of the models. $\Delta m^{\rm bol}_{15}$ is the change in bolometric magnitude between maximum light and 15 days thereafter. Due to Monte Carlo noise magnitudes are uncertain by ∼0.1 mag.

Model	1	2	3	4	5	6
$t_{\rm peak}$ [days]	18.6	18.6	18.0	15.5	14.4	13.9
$M^{\rm bol}_{\rm peak}$	−17.6	−18.2	−18.7	−19.1	−19.4	−19.5
$\Delta m^{\rm bol}_{15}$	0.64	0.40	0.50	0.55	0.55	0.66

the brighter models, the ^{56}Ni-rich core material extends to higher velocities (see Fig. 3.4) and the opacity of the outermost layers is less owing to the lower masses of the IGEs made in the helium shell detonation. The fainter models show a single, fairly broad UVOIR maximum while the brighter models have an initial peak with a weak shoulder appearing around 30 days after maximum light. This shape is qualitatively similar to that obtained for UVOIR light curves for standard Type Ia supernova models such as W7 (Nomoto et al. 1984); see Fig. 7 of Kromer & Sim (2009).

Due to their radioactivity, the peculiar IGEs ^{52}Fe, ^{48}Cr, and ^{44}Ti that are produced in the helium shell detonations of the models could all play a part in powering the supernova light curve. ^{52}Fe and ^{48}Cr have relatively short decay times and release a similar amount of energy per decay as ^{56}Ni. Since they are located in the outer ejecta (see Figs. 3.4 and 3.6), they can contribute to the early phase light curve of the models in which they are abundant. This is illustrated in Fig. 3.14 where, for Model 1, the light curve computed including the energy released by ^{52}Fe and ^{48}Cr is compared to that obtained if these decay chains are neglected. Generally, the contribution from ^{52}Fe and ^{48}Cr decays is fairly small and is most significant during the rising phase, as expected. The light curve at maximum is completely dominated by energy released from ^{56}Ni and ^{56}Co decays and it remains so throughout the decay phase. There is a modest enhancement around 30 days (of about $\leq$0.2 mag) that is mostly due to energy produced by ^{48}V, the daughter of ^{48}Cr for which the decay time is $\tau_{1/2} = 16$ days. The half-life of ^{44}Ti is too long for its decay to directly contribute to the early light curve. Nevertheless, the abundance of titanium is crucial for U- and B-band light curves since even small amounts contribute significantly to the opacity of the shell (see below).

As the models have already been excluded spectroscopically, the color light curves and their temporal evolution are not discussed here in detail. Instead, only the main shortcomings found by Kromer et al. (2010) are described. It is the chromium and the titanium from the shell detonation products that are crucial here: as already mentioned in the previous section, they shift flux from the UV and the blue towards the red part of the spectrum. This results in the U and B color light curves being generally too faint and the redder color light curves being too bright. In Fig. 3.15 $B-V$ color curves are given for all models and compared with that of representative Type Ia supernovae: SN 2005cf (Pastorello et al. 2007b) and SN 2004eo (Pastorello et al. 2007a) mark the bright and the faint end of normal Type Ia supernovae, respectively. SN 1991bg (Filippenko et al. 1992a; Leibundgut et al. 1993) is chosen as the proto-typical sub-luminous event. Except for Model 6, all models are at all times (much) redder than normal Type Ia supernovae. Additionally, within the series of models the $B-V$ color increases in the direction of higher shell masses and therefore the offset from the observations becomes larger. At maximum light, $B-V$ ranges from 0.28 (Model 5) to 1.67 (Model 1). Contrary to this, normal Type Ia supernovae show values of $\sim$0.0. Remarkably, a previous study of sub-Chandrasekhar models with more massive

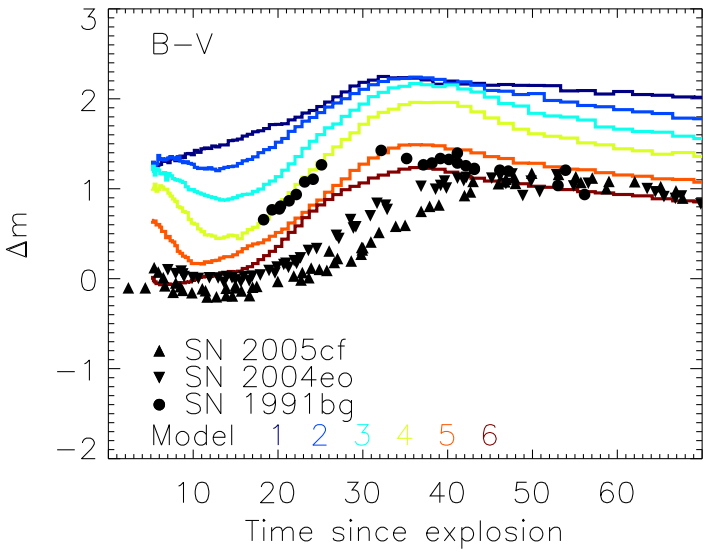

Figure 3.15.: $B-V$ color curves for all models from Kromer et al. (2010). Symbols show the colors of real supernovae: SN 2005cf (Pastorello et al. 2007b) and SN 2004eo (Pastorello et al. 2007a) mark the bright and the faint end of normal Type Ia supernovae, whereas SN 1991bg (Filippenko et al. 1992a; Leibundgut et al. 1993) is a sub-luminous event.

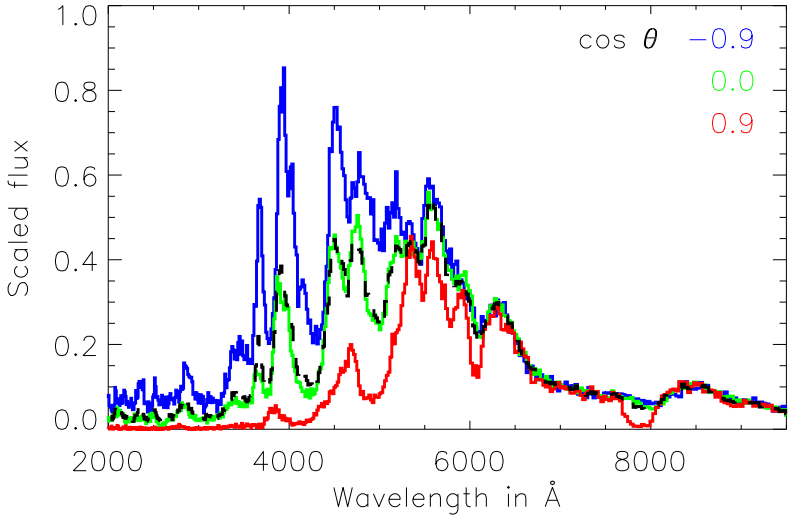

Figure 3.16.: Synthetic spectra for Model 3 at maximum light from Kromer et al. (2010) for northern ($\cos\theta = 0.9$), equatorial ($\cos\theta = 0.0$), and southern ($\cos\theta = -0.9$) lines of sight. θ is the angle between the northern polar axis and the observer's line of sight.

shells by Höflich & Khokhlov (1996) found significantly bluer colors than in the model series of this work with $B - V$ ranging from -0.04 to 0.06 (from their brightest to the faintest model).

As SN 1991bg is much redder than normal Type Ia supernovae (at least in the early phases), it is comparable to Model 4 around maximum light. However, this model has a nickel mass of $\sim$0.8 $M_\odot$ and is far too bright to be a candidate for a sub-luminous explosion. Also, Model 6, which appears to have $B - V$ colors comparable to normal supernovae because of its negligible shell mass, can be excluded by several other criteria like its spectrum or its light curves that are declining too rapidly.

3.3.3. Asymmetry effects

Asymmetry effects of both core and shell ejecta in the models have been described already in Sect. 3.2.3. According to Kromer et al. (2010), most important for the synthetic spectra is the inhomogeneous distribution of the IGEs chromium and titanium in the shell ejecta: from northern to southern directions the amount of unburnt material increases and among the burnt material the IGE fraction decreases. Therefore, the spectra and light curves viewed from southern directions are much less influenced by IGEs from the shell than the northern directions. This is illustrated in Fig. 3.16 that shows line-of-sight dependent maximum spectra

for Model 3: going from southern, equatorial to northern lines of sight, more and more flux is shifted from UV and blue wavelengths to red wavelengths. This also leads to significant differences in the band limited luminosities. For example, the B-band maximum observed from the south is as much as $\sim$2 mag brighter than that observed from the north. Thus, the angle-dependent spread within one model can easily be larger than the spread of angle averaged quantities between two different models of the series. This spread is far too large compared to the observational scatter found among Type Ia supernovae and emphasizes the extreme sensitivity of the observables on the amount of IGEs present in the shell ejecta. All other models show qualitatively similar line-of-sight effects; however, for the models with less mass in the shell they are less pronounced. Therefore, with these strong asymmetries the models could only be considered as candidates for extreme outliers among Type Ia supernovae.

A secondary asymmetry effect is also present in all models, as pointed out by Kromer et al. (2010): due to the off-center initiation of the core detonation, more IMEs are produced in northern and equatorial directions than in the south. Therefore, e.g., the Si II λ6355 feature as seen in Fig. 3.16 is most prominent in the north despite the stronger influence of shell IGE material there.

3.3.4. Carbon-enriched helium shells

The good reproduction of normal Type Ia supernova spectra by the core-only toy model 3c seen in Fig. 3.12 is remarkable. But, is there a way to avoid the production of the problematic IGEs in the helium detonation? One possibility could be a restriction of the maximum mass numbers that can be achieved by successive α-captures on seed nuclei in the helium detonation. By assuming a significant initial amount of carbon seed nuclei and thus a smaller amount of available α-particles, the number of possible α-captures can be limited (other α-chain elements and ^{14}N could also be enriched, but would be less frequent). Three different effects might contribute to such a carbon enrichment: the production of carbon in the donor before accretion, hydrostatic volume burning in the hot accreted helium layer before runaway, or dredge-up of core material (cf. Shen & Bildsten 2009).

By assuming a large carbon fraction, another toy model was constructed, called "Model 3m", that completely avoids IGEs in the shell ejecta. According to the considerations of Sect. 3.2.3, for $X_{^{12}\mathrm{C}} = 1/3$, maximum mass numbers at densities below ρ_{NSE} are as small as 36, which corresponds to the element argon. Argon is almost invisible in synthetic observables and therefore this change is expected to influence the results in a favorable way. Based on this argumentation, in Model 3m, which is very similar to Model 3, a carbon mass fraction of $X_{^{12}\mathrm{C}} = 0.34$ was artificially assumed in the post-processing step (the hydrodynamic simulation was still carried out with a pure helium shell). Triple-α reactions occurring before the detonation at the high shell temperatures of Model 3 had produced additional seed nuclei (see Sect. 3.2.3). To reduce this effect, this time the maximum initial shell

Table 3.5.: Total nucleosynthetic yields of the most abundant species for the helium detonations of Models 3m and 3. For further details, see the caption of Table 3.3.

Model	3m	3
$M_{\mathrm{He,\,fuel}}$	4.6×10^{-2}	5.5×10^{-2}
M_{IGEs}	4.2×10^{-5}	1.7×10^{-2} (30%)
M_{IMEs}	4.6×10^{-2} (99%)	5.3×10^{-3} (10%)
$M_{^{56}\mathrm{Ni}}$	1.1×10^{-8}	1.7×10^{-3} (3%)
$M_{^{52}\mathrm{Fe}}$	6.1×10^{-9}	6.2×10^{-3} (11%)
$M_{^{48}\mathrm{Cr}}$	7.9×10^{-8}	4.4×10^{-3} (8%)
$M_{^{44}\mathrm{Ti}}$	4.2×10^{-5}	3.4×10^{-3} (6%)
$M_{^{40}\mathrm{Ca}}$	3.5×10^{-3} (8%)	2.2×10^{-3} (4%)
$M_{^{36}\mathrm{Ar}}$	2.7×10^{-2} (60%)	2.0×10^{-3} (4%)
$M_{^{32}\mathrm{S}}$	1.4×10^{-2} (30%)	7.8×10^{-4} (1%)
$M_{^{28}\mathrm{Si}}$	5.9×10^{-4} (1%)	1.4×10^{-4}
$M_{^{12}\mathrm{C}}$	3.2×10^{-5}	2.2×10^{-4}
$M_{^{4}\mathrm{He}}$	2.74×10^{-4} (1%)	3.3×10^{-2} (60%)

temperature was lowered to 4×10^8 K, yielding a slightly different base density and shell mass of $\rho_\mathrm{b} = 6.2 \times 10^5$ g cm^{-3} and 0.046 $M_\odot$, respectively. In all other respects the hydrodynamic simulation was very similar to that of Model 3: it showed the same off-center shock convergence and triggered a secondary carbon detonation. Assuming $X_{^{12}\mathrm{C}} = 0.34$ in the post-processing step is not consistent with the hydrodynamic burning scheme that was calibrated for detonations in pure helium. However, according to the fast convergence speed of the calibration runs discussed in Sect. 2.5, the approximation should still be reasonable.

The final nucleosynthetic yields produced in the modified helium detonation of Model 3m are given in Table 3.5. For comparison, the corresponding results of the original Model 3 are also listed. Figure 3.17 shows how products (indicated by the mean mass number) and density are distributed in velocity space at the end of the simulation ($t = 10$ s). Almost exclusively IMEs with $\bar{A} \lesssim 36$ are produced and almost no helium remains unburnt (1% compared to 60% for Model 3), as the "bottle neck" of the triple-α reaction at low densities is avoided due to the initial carbon. The distribution of $\bar{A}$ appears to be remarkably homogeneous both angularly and radially. The remaining asymmetry arises only from the density distribution: high density regions reach out to greater velocities if one goes from the south to the north. Here, however, this asymmetry does almost not matter for the observables, as none of the products of the helium shell has very strong absorption capabilities.

Regarding the synthetic spectrum of Kromer et al. (2010) at three days before B-band maximum (Fig. 3.18), the increase in the carbon abundance in the shell has the intended effect: fluorescence of ^{48}Cr and ^{44}Ti does no longer dominate

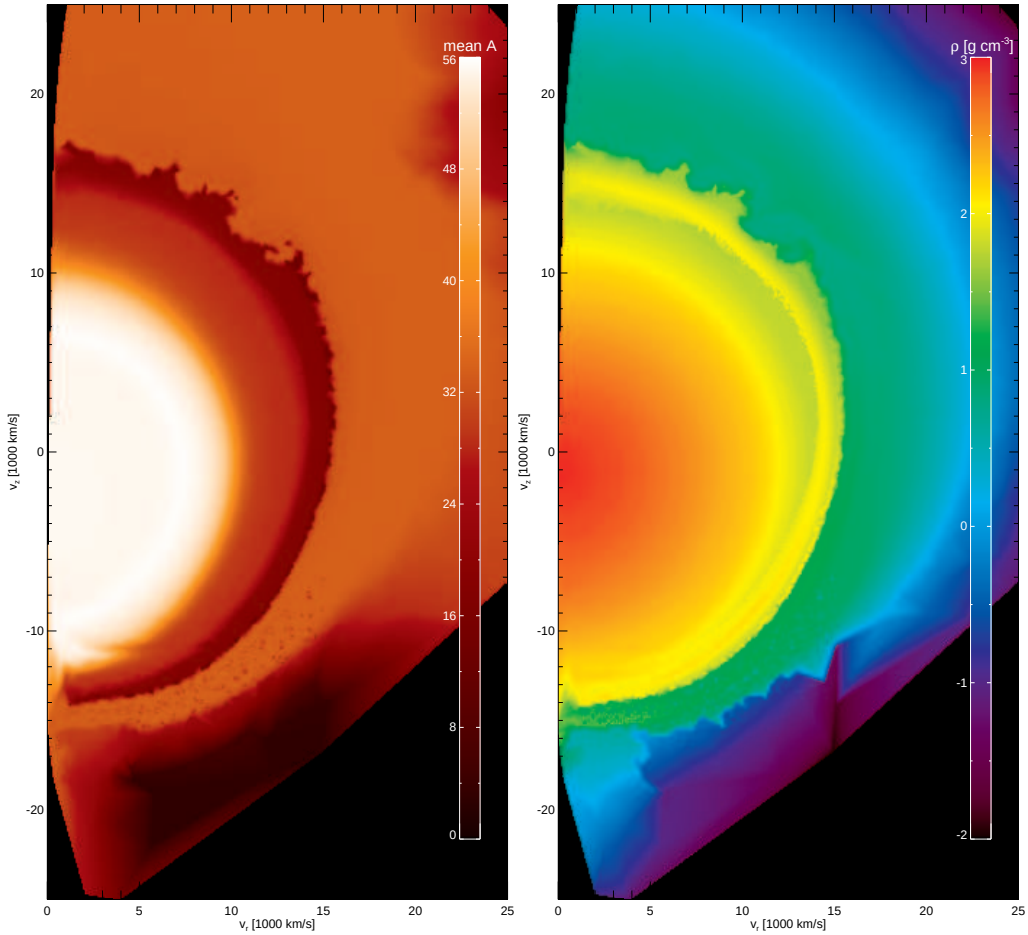

Figure 3.17.: Ejecta structure in velocity space for Model 3m at 10 s derived from the tracer particle distribution after the post-processing step. Color coded are the mean mass number ($\bar{A} = \sum_i A_i X_i$, left plot) and the density (right plot).

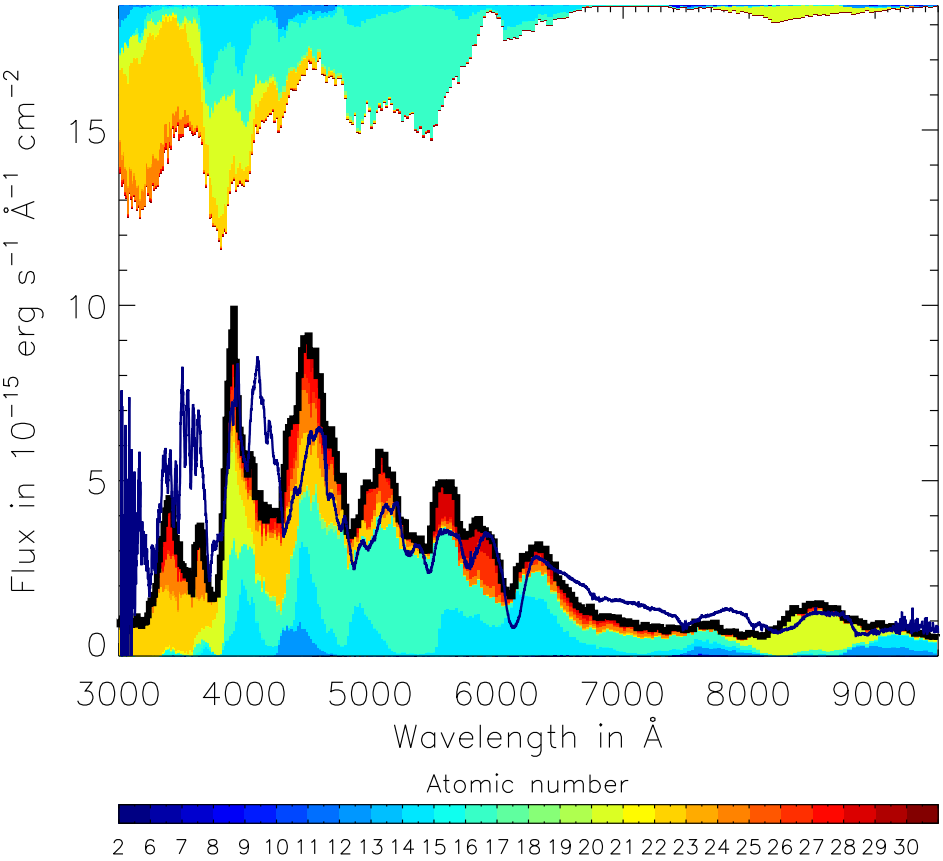

Figure 3.18.: Angle-averaged synthetic spectrum at three days before B-band maximum for Model 3m (thick black line) from Kromer et al. (2010). The dark blue line shows the spectrum of SN 2004eo, for comparison. For further details, see the caption of Fig. 3.11.

the spectrum. Despite the helium shell products being present, the spectrum now shows the typical lines of IMEs similar to the core-only Model 3c (Fig. 3.12) and, in the case of ^{40}Ca, the agreement is even better for the Ca II near infra-red triplet ($M_{^{40}\mathrm{Ca}}$ has increased from 2.2 to 3.5×10^{-3} $M_\odot$). The overall agreement with SN 2004eo is, however, slightly worse than for Model 3c due to the presence of 4.2×10^{-5} $M_\odot$ of ^{44}Ti. Even after a decrease of almost two orders of magnitude in ^{44}Ti it seems to be still too abundant and causes characteristic absorption troughs to the left and to the right of $\lambda \approx 4000$ Å.

Over-abundances of ^{44}Ti turn out to be a good criterion for excluding models as candidates for Type Ia supernovae. Unfortunately, the precise amount of ^{44}Ti depends on details of the nucleosynthesis and the detonation dynamics that are not yet represented accurately enough in the applied numerical modeling scheme. With the current simulations it can be concluded, that even more initial carbon should have been included in the shell to further reduce ^{44}Ti (several smaller initial carbon fractions have been tried in the post-processing, yielding always greater amounts of ^{44}Ti than for Model 3m). $X_{^{12}\mathrm{C}} \sim 1/3$ appears to be a lower boundary of carbon or other seed nuclei that are needed in the double-detonation sub-Chandrasekhar models of this work to produce synthetic observables that agree with that of Type Ia supernovae.

3.4. Summary, discussion, and outlook

In this work the suitability of the double-detonation sub-Chandrasekhar scenario as a model for Type Ia supernovae has been investigated. It has been shown that an assumed detonation in the helium shell robustly triggers a secondary detonation in the C/O-WD core even for the smallest possible shell masses that may detonate (Sect. 3.2). Further, if one assumes the helium detonation to occur, population synthesis studies predict enough progenitor systems from AM CVn binaries to explain a significant fraction of the Galactic Type Ia supernova rate (see Sect. 3.1.2).

An important benefit of the sub-Chandrasekhar scenario is that the variable mass of the exploding star could provide a natural parameter to account for the diversity among observed supernovae. According to Sim et al. (2010), it might even allow for a link between the host galaxy stellar population and the typical brightnesses of supernovae and thus explain observed correlations (see e.g. Howell 2001).

Another argument in favor of the sub-Chandrasekhar model has been derived by Stritzinger et al. (2006) who empirically modeled a set of well-observed bolometric light curves. By fitting parametrized models describing the radioactive decay energy deposition to the quasi-exponential phase of the light curves (∼50 to 100 days after maximum light) they found that different ejecta masses—often significantly below the Chandrasekhar limit—are needed to explain the investigated sample of events. Therefore, sub-Chandrasekhar explosions are a promising model for thermonuclear

supernovae, provided that their synthetic observables match the observations.

In Sect. 3.3 it has been shown that the models of Sect. 3.2 that assume pure helium in the accreted shell and use an approximate burning scheme do not agree with any type of observed thermonuclear supernova (Kromer et al. 2010). Even for minimum helium shell masses, too much IGEs, especially ^{44}Ti and ^{48}Cr, are produced in the shell detonations. Therefore, both spectra and light curves are too red due to fluorescence effects and the lines of IMEs are extremely weak. If this is true for minimum shell masses, it will likely be true for higher shell masses as well. However, toy model calculations without the shell products or with modified shell compositions show that sub-Chandrasekhar explosions can, in principle, reproduce even normal Type Ia supernovae remarkably well.

This success has lead to a parameter study about detonations of pure sub-Chandrasekhar C/O-WDs (i.e. without any helium shell) by Sim et al. (2010). Carrying out similar hydrodynamics and post-processing calculations as in this work and also multi-wavelength radiative transfer simulations with the code ARTIS, they found a wide range of ^{56}Ni-masses and a good reproduction of both Type Ia supernova spectra and light curves by their series of models. The optical light curve rise times, peak colors, and decline time scales display trends which are in agreement with observed characteristics. For example, a B-band width–luminosity relationship similar to the "Phillips relation" (Pskovskii 1977; Phillips 1993) is found (an exact reproduction cannot be expected due to the simplicity of the models). The spectra display features of IMEs at maximum light and even show the correct sense of the correlation between brightness and the ratio of the Si II line strengths at λ6355 and λ5972.

As already mentioned, all these arguments in favor of sub-Chandrasekhar scenarios apply to the helium shell detonation channel only if the IGEs in the shell burning products can be avoided. Unfortunately, scenarios that avoid helium detonations are unexplored and therefore pure speculations. If the IGEs cannot be avoided, the arguments might be also turned around: if every helium shell detonation causes a successive core detonation and the progenitor systems are frequent, but the spectra are always too red, dominated by the wrong elements and thus in contradiction to observations, then the only conclusion can be that the helium detonations do not occur, are very rare, or happen only for systems that are not massive enough to produce any ^{56}Ni. Note here that wrong classifications are very unlikely. One could speculate that relatively dim thermonuclear supernovae that show too red colors and no strong silicon line could be accidentally classified as Type Ic supernovae. However, in most cases a classification is performed spectroscopically and Type Ic supernovae do not show features of titanium or chromium that Kromer et al. (2010) find in the maximum model spectra (see Sect. 3.3.1). Instead, these supernovae show forbidden oxygen lines in the nebular phase which are not found in Type Ia supernova spectra and are also not expected in the models of Sect. 3.2, as unburnt oxygen and nickel (to excite the oxygen) are not found intermixed.

Therefore, the only remedy for the helium detonation channel is to avoid the effects of IGEs in the helium burning products as discussed in Sect. 3.3.4: if enough

seed nuclei, like ^{12}C, ^{16}O, ^{20}Ne, ^{24}Mg, or ^{14}N (cf. Shen & Bildsten 2009), are added to the shell before dynamical burning, then there are not enough α-particles to reach IGEs by α-captures on the seeds during detonation. These seed nuclei were shown to remain unburnt until the onset of dynamical burning by Shen & Bildsten (2009). However, it is unclear if hydrostatic volume burning that could produce carbon via triple-α reactions in the hot accreted helium layer before runaway, or dredge-up of core material can really provide that many seed nuclei (e.g., $X_{^{12}\mathrm{C}} \gtrsim 1/3$). To settle this question, the accretion phase before runaway should be simulated in detail in the future, including all relevant physical processes.

On the other hand, if the strong enrichment of the helium shell with heavy seed nuclei turns out to be possible, it is not yet enough: the lack of observations of the peculiar spectra and light curves described in Sect. 3.3 makes it necessary that the majority of helium detonations that cause bright enough explosions happen with such huge admixtures of seed nuclei. Thus, these enrichment processes would have to work very robustly. Suggestions by Kromer et al. (2010) that part of the problematic titanium and chromium atoms in the shell could be in a different ionization state (where they do not show the aforementioned fluorescence) could however help to weaken this constraint significantly.

If these requirements seem difficult to fulfill, one should keep in mind the study of Sim et al. (2010). It shows that the density stratification of sub-Chandrasekhar explosions and the straightforward parametrization with the total mass of the progenitor can reproduce a large sample of observed supernova spectra and light curves remarkably well. This suggests that there may exist some realization of the sub-Chandrasekhar model in nature that works without having the problems discussed in Sect. 3.3 and should motivate more work on sub-Chandrasekhar scenarios. Refining the double-detonation sub-Chandrasekhar models with more realistic initial shell compositions and improving the modeling of detonation burning (see Sect. 2.5.4) could contribute to answering this question. Other tasks that cannot be separated from the explosion modeling will of course be improving the radiative transfer simulations and studies of binary evolution and the detailed accretion processes that set the stage for the supernova explosions.

4. Delayed detonations in differentially rotating white dwarfs

Inspired by the work of Pfannes et al. (2010b,a), the influence of rapidly rotating white dwarf progenitors on Type Ia supernovae is studied in this chapter. The main focus is on the delayed detonation scenario that has not been investigated in the context of rotating initial models before. Rotation can influence both the progenitor structure (allowing the production of more IMEs due to a flattened initial density profile) and the propagation of the flame. In the following, first, an introduction is given in which the findings of previous studies on the role of rotation in Type Ia supernovae are summarized and the simulations of this work are motivated (Sect. 4.1). Then, the rotating initial models are introduced (Sect. 4.2), followed by the ignition conditions (including also the DDT criterion; Sect. 4.3), and the numerical methods used in the simulations (Sect. 4.4). For a better understanding of the further results, the applied detonation scheme is compared to the rather different one used by Pfannes et al. (2010a). To this end, a prompt detonation simulation of a rapidly rotating progenitor is studied (Sect. 4.5). Results of delayed detonation simulations are then presented in Sect. 4.6 and, finally, a summary is given in Sect. 4.7.

4.1. Introduction: rapidly rotating C/O white dwarfs and Type Ia supernovae

4.1.1. Spinning up C/O white dwarfs by accretion

Almost all simulations of Type Ia supernovae have thus far completely neglected potential effects due to rotation of the progenitor star. However, for WDs accreting matter from a binary companion even rapid rotation is plausible. Yoon & Langer (2004) point out the example of cataclysmic variables: WD accretors in such systems have been shown to rotate much faster than isolated ones (Sion 1999). On the other hand, explosive burning in Type Ia supernovae takes place on very short time scales on the order of the dynamical time scale of the WD. Therefore, rotation must be nearly critical to have any significant impact on the propagation of the flame (Pfannes et al. 2010b).

C/O WDs have an average mass of $\sim$0.6 $M_\odot$ (Homeier et al. 1998). Thus, in the standard single-degenerate scenario for Type Ia supernovae, a lot of material has to be accreted until the Chandrasekhar limit of $\sim$1.4 $M_\odot$ is reached. Together with the matter also angular momentum is accreted. Many complex physical

processes play a role here. First, the accretion disc is believed to be Keplerian, i.e, the matter rotates fast enough for the gravitational force to yield exactly the centripetal force. Thus, the material has to be slowed down somehow (e.g. by viscous effects in the accretion disc) to be accreted on the WD. Then, for the star to spin up significantly, the gained angular momentum has to be transported inwards. Otherwise, the rotation in the outer parts will become critical and no more matter and thus angular momentum can be accreted (rotation is said to be critical when the star loses mass at its equator due to the matter moving faster than Keplerian).

According to Yoon & Langer (2004), "angular momentum can be transported [towards the center] by Eddington-Sweet circulations and by turbulent diffusion induced by hydrodynamic instabilities". The most important hydrodynamic instability in this context is the dynamic shear instability. Using a one-dimensional stellar evolution code that models angular momentum transport as a diffusion process and effectively includes all the relevant physical processes (partially in a parametrized way), they analyze the spin up during accretion and the importance of the various instabilities. Their main results are:

- Accreting WDs rotate differentially throughout their evolution.
- Due to differential rotation, carbon ignition (assumed to occur at densities of 2×10^9 g cm^{-3}) is found to potentially occur at a wide range of masses above the Chandrasekhar limit of the non-rotating case. Rotation can, indeed, be critical when carbon ignites (Yoon & Langer 2005).
- From the rapidly rotating outer parts of the star, where matter is accreted, the angular velocity first rises to a maximum, Ω_{peak}. This increase is caused by contraction: inner parts of the shell contract faster than outer parts while matter is accreted. Further inwards, the angular velocity decreases again, as the angular momentum transport is too slow to speed up the matter there as much as the outer parts. The angular velocity maximum lies in a range of $1.5 \text{ rad s}^{-1} \lesssim \Omega_{\mathrm{peak}} \lesssim 6.5 \text{ rad s}^{-1}$ when central carbon ignition densities are reached (Pfannes et al. 2010b). The corresponding range of total masses is $1.5\ M_\odot \lesssim M \lesssim 2.1\ M_\odot$.

Note that all the models of Yoon & Langer (2004) were initially rotating too rapidly when reaching the Chandrasekhar mass. Thus, the central density was too low for carbon ignition and an accretion induced collapse seemed unavoidable. Only after the inclusion of a way to lose some of the accreted angular momentum, carbon ignition densities could be reached. One possibility that is found to be suitable by Yoon & Langer (2004) is the Chandrasekhar–Friedman–Schutz (or CFS) instability (for references see Yoon & Langer 2004), in which non-axisymmetric perturbations of the mass distribution lead to gravitational wave emission.

An important restriction of the study of Yoon & Langer (2004) may be that they neglect effects of magnetic fields, which tend to slow down rotation, in

their calculations. Therefore, rapid rotation of accreting WDs is still afflicted with uncertainties. If there are, e.g., strong braking magnetic torques or efficient viscous angular momentum transport, also rigidly rotating WDs may form (Pfannes et al. 2010b). Even close to the critical case, for those the Chandrasekhar mass increases only slightly to $\sim$1.48 $M_\odot$ (Yoon & Langer 2004) and rotation in the interior is significantly less rapid than for differentially rotating models, which can be dynamically stable until $\sim$4.0 $M_\odot$ (see Yoon & Langer 2004, and references therein). In the following, the term 'rapid rotation' therefore only refers to (nearly critical) differential rotation in non-magnetized WDs.

Before applications of the rapidly rotating WD models are discussed, it should be stressed that rapid rotation will most likely not play a role in the sub-Chandrasekhar helium shell detonation models of Sect. 3.2. As in this scenario only $\lesssim$0.1 $M_\odot$ are accreted, the angular momentum gain will be much lower than in the "super-Chandrasekhar" scenarios discussed below. Therefore, rotation effects should be unimportant for the models of Chap. 3.

4.1.2. Influence of rotating progenitors on Type Ia supernova explosions

Pfannes et al. (2010b) have studied the influence of rapid rotation of the progenitor star on Type Ia supernova explosions for the Chandrasekhar-mass scenario. They used the accreting white dwarf (AWD) models of Yoon & Langer (2004) to construct their rotating progenitor stars. As the results of Yoon & Langer (2004) partially depend on model parameters and the relevant physical processes are not well understood yet, Pfannes et al. (2010b) just mimic the range of expected rotation laws in a parametrized manner. Their conclusion is, however, robustly found for all of their models: *the standard deflagration scenario and rapidly rotating progenitors are incompatible when trying to explain Type Ia supernovae.* In all of their simulations "the flame develops a strong anisotropy with a preferred direction towards the stellar poles, leaving great amounts of unburnt matter along the equatorial plane." The consequences of this are twofold: for moderate deflagration ignition conditions, the burning will fail to unbind the star and there will be no explosion; for strong deflagrations, there may be an explosion, but the unburnt material close to the center conflicts with observed spectra that show no carbon features after the early explosion phase (cf. Sect. 1.2).

In simulations with almost critical rigid rotation ($\Omega \approx 0.37$ rad s^{-1}) and only a slightly increased Chandrasekhar mass of 1.47 $M_\odot$, on the other hand, Pfannes et al. (2010b) found very similar results as for non-rotating deflagrations (even in the non-rotating case, deflagrations have the problem of unburnt carbon close to the center). This illustrates that only very rapid (differential) rotation has a significant influence on Type Ia supernova models.

A way to avoid unburnt fuel close to the center of supernovae with rapidly rotating progenitors and to produce bright explosions was discussed in Pfannes et al. (2010a). They investigated the suitability of pure detonations of rapidly rotating

progenitors for modeling super-luminous Type Ia supernovae. Due to the shallow density profiles arising from the differential rotation (see Sect. 1.3), significant amounts of IMEs might be produced. A similar scenario was already investigated earlier by Steinmetz et al. (1992), who applied the so-called "j-const" rotation law that unphysically assumes an overall constant specific angular momentum j. In this study the change in the density profile was found insufficient to significantly enhance the IME production over that of the non-rotating pure detonation model (Arnett 1969; Arnett et al. 1971). Contrary, in the new study of Pfannes et al. (2010a) reasonable agreement with super-luminous Type Ia supernovae in terms of both burning products and explosion kinematics is claimed. However, they assume a very high NSE transition density in their detonations, which is shown to be very unlikely by comparison with a prompt detonation model using the improved scheme of this work (see Sect. 4.5).

Another explosion scenario that has not been investigated in the context of rapidly rotating progenitors and that could avoid the shortcomings of both the deflagration and the pure detonation model is the delayed detonation scenario. It has been proposed (Yoon & Langer 2004; Pfannes et al. 2010a) that rapid differential rotation could trigger a deflagration-to-detonation transition (DDT). The velocity gradients in a differentially rotating WD could be enhanced due to the expansion that accompanies the deflagration flame in the polar direction: in this region the rotational velocities would go down; in the outer layers that are further away from the axis the rotation could, however, sill be very rapid (also, the angular velocity maximum is located there). Thus, strong velocity gradients could arise, induce an abrupt acceleration of the flame by increasing its surface and lead to an increased probability of a DDT. If both the deflagration and the pure detonation scenario are no suitable models for explaining Type Ia supernovae, delayed detonations remain the last possibility. They have the advantage that unburnt fuel, which is left by the deflagration in the equatorial plane, can be consumed by the detonation. Compared to the prompt detonations, the delayed detonation scenario further has the benefit that, due to pre-expansion of the fuel during the deflagration phase, it could produce a sufficient amount of IMEs and potentially also explain not only super-luminous, but normally bright Type Ia supernovae. Therefore, it was decided to study this scenario applying the improved tools for modeling nuclear burning fronts introduced in Chap. 2.

4.2. Rotating initial models

In this work rotating C/O-WD models similar to those of Pfannes et al. (2010b) have been constructed and the same nomenclature is used. Model parameters are given in Table 4.1. The models span a range of total masses M (1.6–2.0 $M_\odot$) and angular momentum J (0.9–2.2×10^{50} g cm^2 s^{-1}). Larger masses than $M \sim 2.0\ M_\odot$ are not expected due to the limited mass budget in single degenerate progenitor systems (Langer et al. 2000). For the calculation of the initial models, a C/O-mass

Table 4.1.: Initial model parameters.

model	AWD1	AWD4	AWD3
ρ_c $[10^9$ g cm$^{-3}]$	2.0	2.0	2.0
Ω_c [rad s^{-1}]	1.659	4.663	4.081
Ω_{peak} [rad s^{-1}]	4.473	5.239	5.299
M^a $[M_\odot]$	1.622	1.775	2.004
c_1	7.347	−16.265	−18.823
c_2	62.006	162.39	196.62
c_3	−275.25	−480.84	−563.38
c_4	342.62	531.85	600.25
c_5	−137.09	−200.81	−218.51
$\bar{s}_{rigid}$	0	0.2	0
$r_{equator}/r_{pole}$	1.629	1.796	2.183
$r_{equator}$ $[10^8$ cm]	3.23	3.32	4.02
r_{pole} $[10^8$ cm]	1.98	1.85	1.84
$E_{grav}{}^a$ $[10^{50}$ erg]	−36.2	−40.9	−44.9
$E_{int}{}^a$ $[10^{50}$ erg]	27.2	29.0	29.5
$E_{rot}{}^a$ $[10^{50}$ erg]	1.77	3.01	4.58
$E_{bind}{}^a$ $[10^{50}$ erg]	−7.22	−8.90	−10.8
β^a [%]	4.867	7.342	10.16
J $[10^{50}$ g cm^2 s$^{-1}]$	0.9110	1.352	2.211

[a] These quantities have been determined after mapping the initial models on the 512^3 grids of the highest resolved simulations.

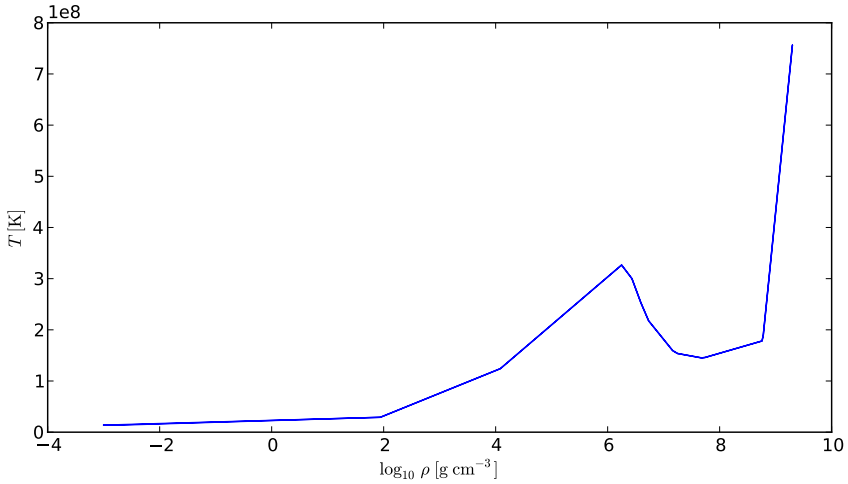

Figure 4.1.: Initial temperature profile of the models as a function of density.

ratio of 0.5 is assumed and the same equation of state as in the hydrodynamics code is applied (for numerical details see Sect. 4.4.3). No enhancement of the chemical composition due to the metallicity of the progenitors is assumed in all calculations. A temperature profile as suggested by Yoon & Langer (2004) for an accreting WD was chosen similar to Pfannes et al. (2010b,a) and Pfannes (2006) (see Fig. 4.1). In the center, high temperatures arise due to the "simmering" phase before ignition. A local maximum at the outer parts of the degenerate core is caused by accretion-induced heating (see Yoon & Langer 2004). In all models, a central density ρ_c of 2×10^9 g cm^{-3} is chosen. The angular velocity distributions have central values Ω_c between 1.6 and 4.6 rad s^{-1} and peak values $\Omega_\mathrm{peak} \sim 5$ rad s^{-1}. Shapes of the rotation laws and the initial density profiles are illustrated in Fig. 4.2. The figure shows cross-sections of the WDs along the rotational axis which is in z-direction. The rotation laws are parametrized by Ω_c, the polynomial coefficients c_1 to c_5 and $\bar{s}_\mathrm{rigid}$ (see Sect. 4.2; $\bar{s}$ is the distance from the rotation axis normalized to the equatorial radius). Contrary to the other models, the AWD4 model does not rotate differentially in its center, but rigidly (for $\bar{s} < \bar{s}_\mathrm{rigid}$). This may occur in all rotating Type Ia supernova progenitors as consequence of the simmering phase before core ignition: efficient convective mixing in this phase should equilibrate the angular momentum.[1] Down to $\rho \sim 10^8$ g cm^{-3}, the WD cores do not deviate much from spherical symmetry. At lower densities they show a typical extended "bulge" of low density material in equatorial direction that becomes more pronounced with increasing total mass (see Fig. 1.1 b). For completeness, equatorial and polar radii and their ratio $r_\mathrm{equator}/r_\mathrm{pole}$, the excentricity parameter, are also given in Table 4.1. E_grav, E_int,

[1] Note that the influence of rapid rotation on the convective simmering phase is still unexplored. Here, it is assumed that the rotation does not prevent a successful ignition.

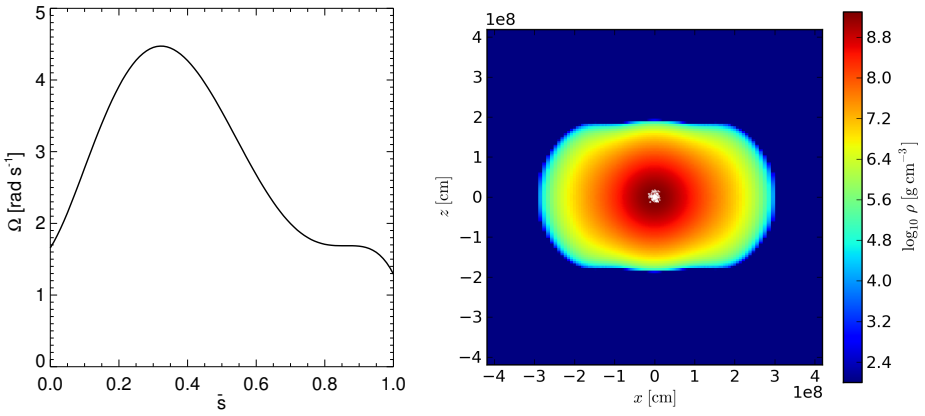

(a) AWD1

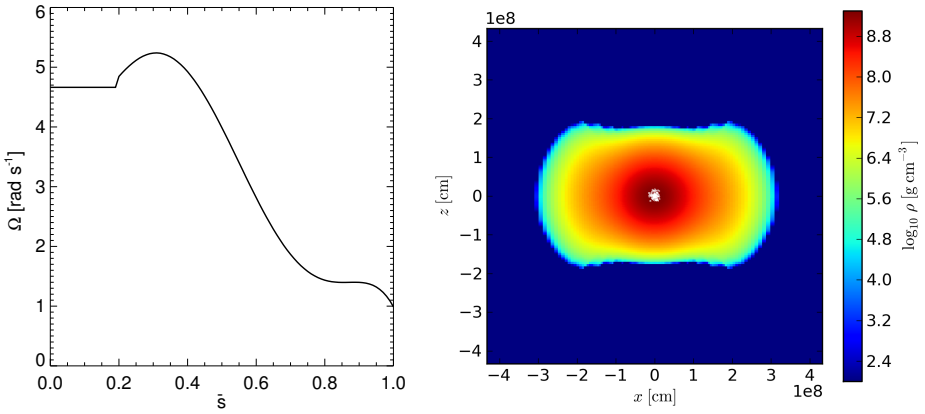

(b) AWD4

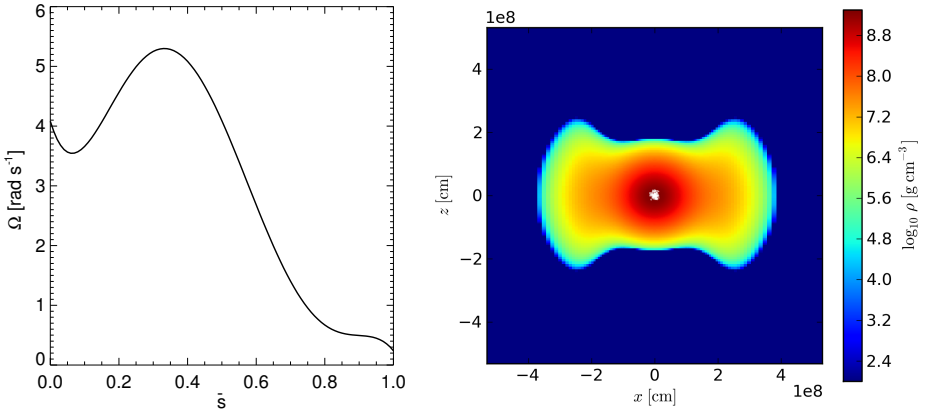

(c) AWD3

Figure 4.2.: Initial rotation laws and density distributions of all rapidly rotating progenitor models.

$E_{\rm rot}$, and $E_{\rm bind}$ are the initial values of gravitational potential, internal, rotational kinetic, and effective binding energy ($E_{\rm bind} = E_{\rm grav} + E_{\rm int} + E_{\rm rot}$), respectively. Finally, $\beta = E_{\rm rot}/|E_{\rm grav}|$ is the ratio of rotational energy and gravitational binding energy.

4.3. Ignition conditions

It is assumed that the supernova explosion starts as a turbulent deflagration in the central core and later turns into a detonation, like in the currently favored delayed detonation scenario for modeling normal Type Ia supernovae. The effects of rapid rotation that are considered here are however not part of the standard model.

Deflagration ignition conditions were shown to have a strong influence on the burning result (see, e.g., Niemeyer et al. 1996; Livne et al. 2005; Röpke et al. 2006; Schmidt & Niemeyer 2006). The goal of this work is to achieve moderate detonation strengths that might lead to explosions distinct from pure detonations (Pfannes et al. 2010a) and produce significant amounts of IMEs. This is possible when the deflagration consumes large parts of the star and the detonation burns only the remaining parts at low densities. Thus, the deflagration phase needs to be relatively strong despite the tendency of deflagrations to be relatively weak in rapidly rotating progenitors (Pfannes et al. 2010b). Therefore, the deflagration ignition conditions are chosen as in Röpke et al. (2007a), who were able to model a strong deflagration producing as much as 0.6 $M_\odot$ of IGE from a (non-rotating) $M_{\rm Ch}$ progenitor. Their simulation was carried out in three dimensions at high resolution and they put 1600 ignition kernels in a spherical volume of radius 180 km around the center (see their Fig. 1). Exactly the same positions of the ignition kernels are used in this study, however, due to the lower resolutions, larger kernel radii of 6 and 10 km are chosen for the simulations with 256^3 and 512^3 cells, respectively. Figure 4.2 illustrates the configuration by showing intersections of the ignition kernels with the xz-plane (for the 512^3 grid) as white contour lines. According to Röpke et al. (2007a), this ignition condition favors burning next to the center and enhances the burning over that of centrally or sparsely ignited models.

To complete the explosion setup, the DDT criterion has to be defined. In one-dimensional simulations DDTs are parametrized relatively arbitrarily. A commonly used scheme is to trigger a detonation when the deflagration flame reaches fuel with densities $\lesssim 10^7$ g cm^{-3}. However, this criterion is only motivated by optimizing the agreement of synthetic with real observables of Type Ia supernovae or, alternatively, by matching the nucleosynthesis (Höflich & Khokhlov 1996; Iwamoto et al. 1999). A rigorous determination from first principles is still not possible, as the exact physical mechanism leading to a DDT is still unknown. An improvement in this sense is achieved by multidimensional modeling, as turbulent flame propagation is an inherently three-dimensional process. This allows a physically motivated parametrization of the DDT from properties of the flame (which is itself only a parametrization in one-dimensional modeling). There exist different DDT criteria

that are related to the onset of the distributed burning regime. The latter is reached when at low densities the flame becomes sufficiently thick to allow small eddies to penetrate into the reaction zone and mix hot ash with cold fuel without immediately burning (cf. Peters 2000). An equivalent condition is

$$\mathrm{Ka} \gtrsim 1, \tag{4.1}$$

with

$$\mathrm{Ka} = \left(\frac{\delta_{\mathrm{lam}}}{l_{\mathrm{Gibs}}} \right)^{1/2} \tag{4.2}$$

being the Karlovitz number. Here, δ_{lam} is the laminar flame width and l_{Gibs} is the Gibson scale (the size of the eddy that turns over in a laminar flame crossing time). Golombek & Niemeyer (2005) and Röpke & Niemeyer (2007) used (4.1) as criterion for the DDT in two- and three-dimensional simulations, following earlier suggestions by Niemeyer & Woosley (1997). However, Woosley (2007) argues that at the onset of distributed burning the first structures to form are too small to detonate and yet more mixing, lower densities, and higher Karlovitz numbers are required.[2] Therefore, Kasen et al. (2009) chose critical values of the Karlovitz number between 250 and 750, which causes a somewhat later transition. In this study, similar criteria are used: at the flame

$$\mathrm{Ka} \geq 250 \quad \text{and} \tag{4.3}$$

$$6 \times 10^6 \ \mathrm{g\,cm^{-3}} < \rho_{\mathrm{u}} < 1.2 \times 10^7 \ \mathrm{g\,cm^{-3}} \tag{4.4}$$

is required for a successful DDT. Multiple transition points are allowed in the WD.

4.4. Numerical methods

4.4.1. Hydrodynamics code and nuclear burning

Most methods that are applied in the numerical simulations here have been used already in previous delayed detonation studies (Röpke & Niemeyer 2007; Kasen et al. 2009). The Eulerian hydrodynamics code, the level-set based scheme for modeling detonation burning, and the post-processing method using tracer particle information to determine more accurate nucleosynthetic abundances are described in Sect. 2.4.

Deflagration flames are modeled in a large-eddy approach using methods developed by Niemeyer & Hillebrandt (1995), Reinecke et al. (1999b, 2002a), Röpke (2005), Schmidt et al. (2006a,b), and Röpke & Schmidt (2009). The deflagration front is propagated analogously to the detonation using a separate level set (cf.

[2] Strictly speaking, within the distributed burning regime only an effective Karlovitz number can be defined because the concept of a laminar flame width does not exist here. The Damköhler number, Da, is the relevant quantity in this regime. Here, a Karlovitz number that is parametrized by the turbulent velocity fluctuations and ρ_{u} is used as a proxy for the corresponding Damköhler number.

Golombek & Niemeyer 2005) and a subgrid-scale model to determine the effective burning speed from unresolved turbulence. Two separate level sets are used to avoid unphysical propagation of the detonation into the deflagration ashes (Maier & Niemeyer 2006).

All simulations presented in this study are full-star simulations in three dimensions. A moving Cartesian hybrid grid is used as described in Röpke et al. (2006): a finely resolved uniformly spaced inner part tracks the growing flame front and an outer part with exponentially growing cell sizes independently follows the WD expansion. The main simulations are carried out with finer resolution (512^3 cells, initial resolution of inner grid: 1.9 km), while some additional runs use lower resolution (256^3 cells, initial resolution of inner grid: 3.9 km). All simulations were stopped at $t = 10$ s, when the expansion of the ejecta can be assumed to be homologous to good approximation.

4.4.2. Modeling self-gravity

Previous studies with this supernova code have approximated the gravitational potential Φ_{grav} only from the monopole moment of the mass distribution. As the rotating initial models significantly depart from spherical symmetry, Φ_{grav} has to be calculated in a more accurate way to allow for hydrostatic stability. Following Pfannes et al. (2010b), the multipole solver from the FLASH code (Fryxell et al. 2000) that is based on the implementation of Müller & Steinmetz (1995) was adapted and integrated in the code. The spherical multipole expansion (see Pfannes 2006, for a detailed description) was cut off after the quadrupole term ($l \leq 2$, $m \leq l$). In contrast to Pfannes et al. (2010b,a), rotational symmetry ($m = 0$) of the mass distribution was not assumed.

To take into account additional symmetries of the mass distribution when simulating only a quadrant of the star in two dimensions or an octant in three dimensions, the implementation was extended to set the according source moments to zero in these cases.

To allow two-dimensional test simulations on a co-rotating cylindrical (r_{cyl}, z_{cyl}, ϕ_{cyl}) coordinate system, a Coriolis force term ($f_\phi = -2 v_r v_\phi / r_{\mathrm{cyl}}$) had to be integrated in the code to couple spherical expansion of the star to an appropriate change in rotational velocity (v_ϕ).

4.4.3. Setup of initial rotators

The three rotating WD models described above (Sect. 4.2) were constructed in hydrostatic equilibrium following Pfannes et al. (2010b) and Pfannes (2006). The method of Eriguchi & Müller (1985) that solves the equation of hydrostatic equilibrium in integral form for a given rotation law, central density and axis ratio $r_{\mathrm{equator}}/r_{\mathrm{pole}}$ was applied. Using the integral form of the equation has the advantage that the boundary conditions can be incorporated in a straightforward way. Discretization yields a system of non-linear equations that is solved by an

iterative Newton-Raphson scheme starting out from a suitable initial guess (see below). The same equation of state as used in the hydrodynamics code was included in piecewise polytropic representation (Müller & Eriguchi 1985). Thereby, a physically motivated temperature profile $T(\rho)$ (Fig. 4.1) was assumed to provide the pressure as a function of density only. In the rotation laws the central angular velocity Ω_c is not fixed, but determined from the iteration scheme by prescribing the axis ratio $r_\mathrm{equator}/r_\mathrm{pole}$. A polynomial representation of the AWD rotation laws (see Sect. 4.2) was chosen by Pfannes et al. (2010b) to allow for an analytic integration of the centrifugal potential ($\Phi_\mathrm{rot}(s) = -\int^s \Omega^2(s')s'\,\mathrm{d}s'$) and an analytic calculation of the Jacobian of the system. The angular velocities have the following form:

$$\Omega(\bar{s}) = \Omega_\mathrm{c} + \begin{cases} 0 & \text{if } 0 \le \bar{s} \le \bar{s}_\mathrm{rigid}, \\ \sum_{i=1}^{5} c_i \bar{s}^i & \text{if } \bar{s}_\mathrm{rigid} < \bar{s} \le 1. \end{cases} \tag{4.5}$$

Here, s is the absolute distance from the rotation axis, while $\bar{s} = s/r_\mathrm{equator}$ is the distance normalized to the equatorial radius r_equator. In the case of the AWD4 rotator the inner region with $s < s_\mathrm{rigid}$ rotates rigidly with Ω_c. For the other models s_rigid is set to zero. Coefficients for all models are given in Table 4.1.

In the algorithm of Eriguchi & Müller (1985) a series of mass distributions and central angular velocities for rotators with increasing prescribed axis ratio ($r_\mathrm{equator}/r_\mathrm{pole} = 1.05^n,\ n = 1, 2, 3, \ldots$) and fixed functional form of the rotation law is calculated. The start values for the Newton-Raphson iteration are taken from a non-rotating WD in hydrostatic equilibrium for $n = 1$ (an initial guess for Ω_c also has to be made) and from the previous model in the series for $n > 1$, respectively.

As in Pfannes et al. (2010b), this scheme was applied for the AWD1 rotation law up to $n = 12$, i.e., an axis ratio of 1.629 yielding $\Omega_\mathrm{c} = 1.659$ and $M = 1.622\ M_\odot$ (see Table 4.1). The other two rotation laws are more extreme. Therefore, a non-rotating density stratification could not be used as start value of the algorithm in these cases (the Newton-Raphson scheme turns out to converge only for a fairly good initial guess). Instead, the AWD1 series was continued to larger axis ratios and the results for $n = 14$ and $n = 16$, which have already the desired axis ratios, were used as start values for the calculation of models AWD4 and AWD3, respectively. From this starting point, series of models were calculated, in which the AWD1 rotation law was continuously transformed into the designated rotation law AWDj, according to

$$c_i = (1-w)c_i^\mathrm{AWD1} + w \cdot c_i^\mathrm{AWD}j, \quad i = 1, \ldots 5, \tag{4.6}$$

$$\bar{s}_\mathrm{rigid} = (1-w)\bar{s}_\mathrm{rigid}^\mathrm{AWD1} + w \cdot \bar{s}_\mathrm{rigid}^\mathrm{AWD}j, \tag{4.7}$$

with $w = 0.1, 0.2, \ldots, 1.0$.

The resulting model parameters differ slightly from that of Pfannes et al. (2010b). The deviations might arise from differences in the used equation of state, temperature profile, resolution of the grid in the initial model calculations, and the way in

which the code of Eriguchi & Müller (1985) was adapted to incorporate the new rotation laws.

In the initial model calculations a non-regular two-dimensional adaptive spherical (r, θ)-grid is used. To map the resulting density distributions on the Cartesian hydrodynamic grid, an interpolation scheme similar to the one described by Pfannes (2006) was applied. The Cartesian coordinate of every hydrodynamic grid cell is mapped to (r, θ) coordinates. Then, the density value for the cell is determined on the spherical grid of the initial model solution by higher-order interpolation (see Sect. 11.4 of Pfannes 2006). Close to the borders of the WD ($\rho < 10^5$ g cm^{-3}) the order of the scheme was reduced to bilinear and the interpolation was performed in logarithmic (instead of linear) density space, as the densities of neighboring grid points can be several orders of magnitude different there (the surface radius of the WD can change dramatically with θ). For all calculated models, the resulting density profiles after the mapping on the computational grid are shown in Fig. 4.2.

4.5. Test of the detonation scheme: a prompt detonation simulation

Before the discussion of the main subject of this study—the delayed detonation models—results of a prompt detonation simulation are presented. This section shows the differences of the detonation models of Pfannes et al. (2010a) and of this work and illustrates the impact that the new detonation table applied here has on supernova models involving detonations.

The detonation table of this work (see Fig. 4.3 a) provides the abundances of the reduced species, $\boldsymbol{X}^{\mathrm{red}}$ (see Sect. "Simplified scheme for nuclear reactions" on page 42), as a function of the density of the unburnt fuel, ρ_{u}. With the iteration scheme of Sect. 2.5 the table has been iteratively calibrated to spherical detonations in C/O WDs using a large nuclear network. Furthermore, it has been shown that the table ensures consistent results in hydrodynamic simulations (see Sect. 2.5.3).

Pfannes et al. (2010a) use a very similar scheme for modeling detonations as this work, however, in their hydrodynamic simulations they apply a (simplified) abundance table (see Fig. 4.3 b) that includes a very high transition density $\rho_{\mathrm{NSE}} = 5.2 \times 10^7$ g cm^{-3} between NSE and the incomplete burning regime. They refer to it as the "high NSE burning density threshold" (HBT) case. For simplicity, and as a sensible upper cutoff, they adopted this high transition density just from the deflagration case. This seems unrealistically high compared to the value of $\sim 10^7$ g cm^{-3} used in this work. The high ρ_{NSE}, leads to a significant underestimation of both the produced IGEs and the explosion energy in their simulations and, correspondingly, an overestimation of IMEs (in their prompt detonation simulation of the AWD3 rotator, Pfannes et al. find $M_{\mathrm{IGE}} = 1.41\ M_\odot$, $M_{\mathrm{IME}} = 0.45\ M_\odot$, and $E_{\mathrm{tot}} = 1.53 \times 10^{51}$ erg). More importantly, the overestimation of ρ_{NSE} leads to the production of IMEs at much too small radii. Combined with the underestimation of the explosion energy this leads to significantly too low expansion velocities of

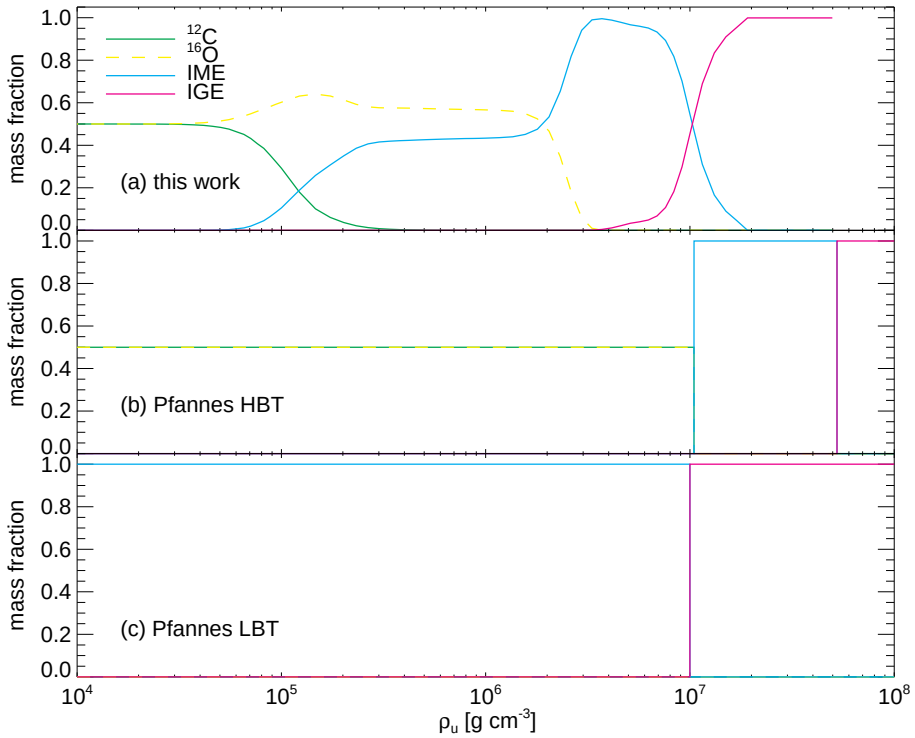

Figure 4.3.: Mass fractions of the species in the C/O detonation tables of this work (a) and of Pfannes et al. (2010a) (b, c) plotted against the density of the unburnt fuel ρ_u.

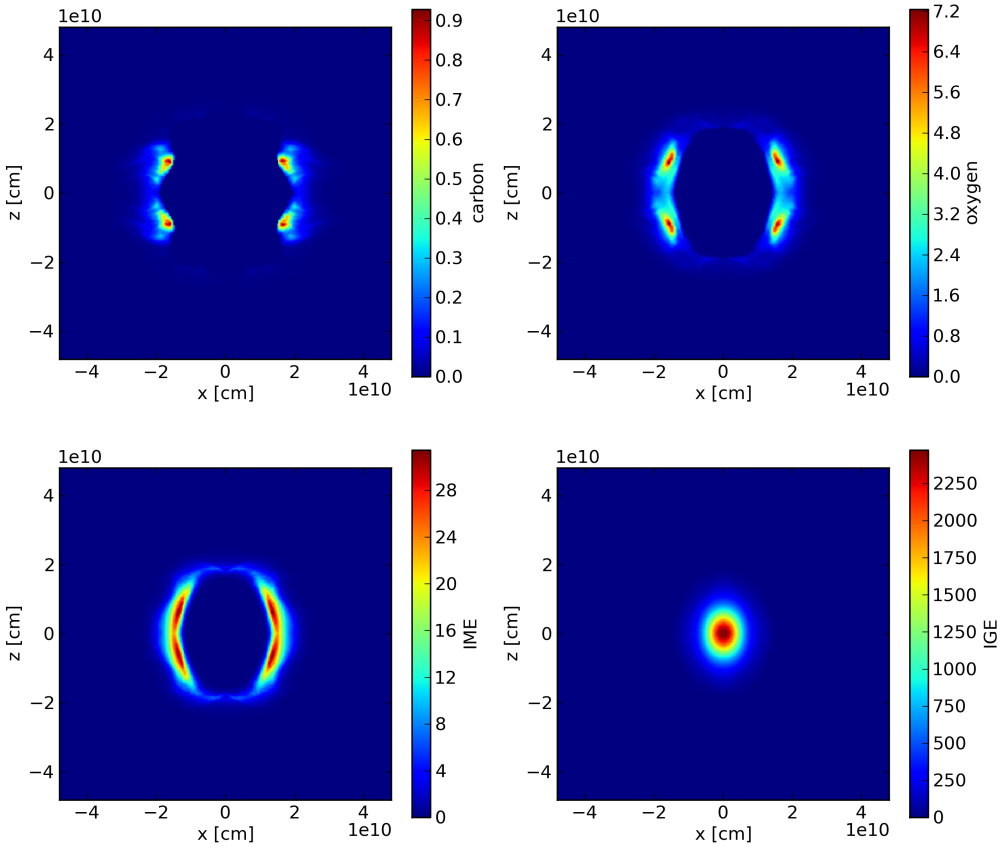

Figure 4.4.: Final composition of the pure detonation model AWD3$^{\mathrm{det}}_{256}$ indicated by the fractional densities ρX_i of species in the hydrodynamic simulation.

IMEs, $v_{\mathrm{IME}} \sim 10\,000$ km s^{-1} (see Fig. 5 b in Pfannes et al. 2010a), in the ejecta in the phase of homologous expansion (where $v \propto r$).

To quantify the influence of a lower (and most likely more realistic) value of ρ_{NSE} on the pure detonation scenario of rapidly rotating WDs, the "AWD3 detonation" model of Pfannes et al. (2010a) was re-simulated using the detonation scheme of this work (Fig. 4.3 a). The resulting Model AWD3$^{\mathrm{det}}_{256}$ produced 1.90 $M_\odot$ of IGEs, only 0.09 $M_\odot$ of IMEs, and $E_{\mathrm{tot}} = 1.95 \times 10^{51}$ erg (for detailed nucleosynthesis results and the explosion energetics see Table 4.2 and Fig. 4.7). Thus, the explosion is much more energetic and produces ∼40% more IGEs than in the case of Pfannes et al. (2010a). Figure 4.4 shows the spatial distributions of the fractional densities[3] ρX_i of the reduced species of the hydrodynamic simulation, ^{12}C, ^{16}O, IMEs, and IGEs, at $t = 10$ s. Intermediate mass elements, unburnt ^{12}C, and ^{16}O are present only at the very low density outer regions (note the very different density scales in

[3]Here, and in all following plots of fractional densities ρX_i, mass fractions X_i below 0.01 are set to zero to avoid the overemphasis of trace abundances in high density regions.

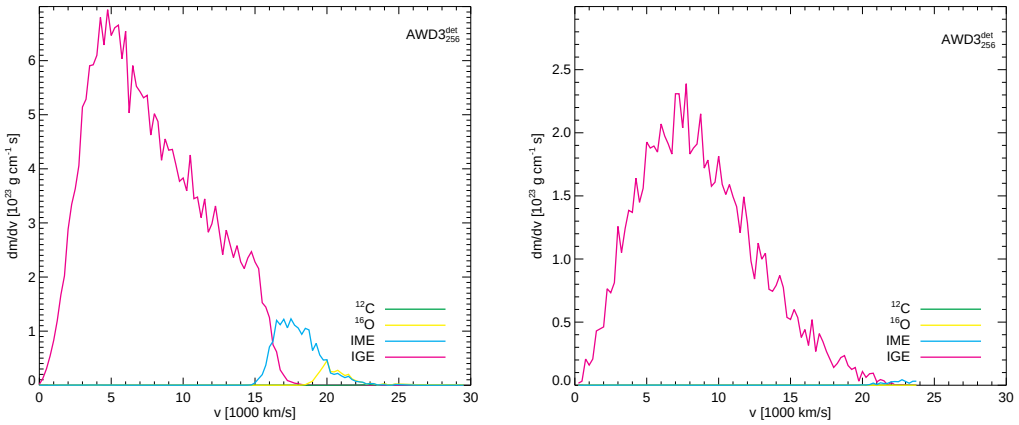

(a) equator plane, $|\theta - \frac{\pi}{2}| < \frac{\pi}{16}$ (b) northern polar axis, $\theta < \frac{\pi}{8}$

Figure 4.5.: Mass distribution of the pure detonation model AWD3$^{\mathrm{det}}_{256}$. Shown are the main groups of elements (determined by Eqs. 2.65–2.69 from the post-processing abundances) in velocity space for selected ranges of the polar angle θ. The velocity bin size is $\Delta v = 250$ km s^{-1}.

every sub-plot) and predominantly close to the equatorial plane. In final velocity space, as shown in Fig. 4.5, these species are found at correspondingly high speeds: IMEs peak around 17 500 km s^{-1} in radial direction (a) and at very high velocities $\gtrsim$22 000 km s^{-1} in polar direction (b), where only very little IMEs are found. As discussed before, Pfannes et al. (2010a) significantly underestimate these expansion velocities and claim to find good agreement with observed spectral line velocities, but this is only possible due to their very high value of ρ_{NSE}. Contrary to these claims, here, it has to be concluded that the prompt detonation of the AWD3 rotator strongly disagrees with observations of super-luminous Type Ia supernovae, which show low silicon velocities around 9000 km s^{-1} at maximum light (for details see the discussion in Sect. 4.6.4). As the delayed detonation models of the next section will show, very high expansion velocities are common to all explosions of rapidly rotating WDs that are dominated by a detonation. Thus, *prompt detonations of rapidly rotating C/O WDs can be excluded in general as candidates for Type Ia supernovae.*

Now, the NSE transition density ρ_{NSE} is discussed. Pfannes et al. (2010a) already mention a potential range of possible ρ_{NSE} values: they argue that effects of shear acting on the detonation front and the cellular instability (see Sects. 2.2.2 and 2.2.3) tend to increase ρ_{NSE} over the value of planar detonations ($\sim 10^7$ g cm^{-3}; Eq. 2.45) and suggest the value of planar deflagrations (their HBT case) as a plausible upper cutoff. As a lower cutoff, they suggest the planar detonation case and denote it as "low NSE burning density threshold" (LBT) case (see Fig. 4.3 c). Using this ρ_{NSE}, they estimate the resulting explosion yields to be $M_{\mathrm{IGE}} = 1.86\ M_\odot$ and $M_{\mathrm{IME}} = 0.21\ M_\odot$. This estimate is based on the hydrostatic density profile of the

progenitor. Regarding the small deviations of real detonations from the planar case (cf. Sect. 2.2.3), it seems very unlikely that shear or cellular instability effects will increase ρ_{NSE} as much as in the HBT case. Instead, for massive progenitors, overdrive effects may shift the resulting ρ_{NSE} significantly below the planar (or LBT) case. These effects arise due to shock strengthening when a detonation propagates towards decreasing densities in a WD and are found to be important in all models of this work (see Sect. 2.5.3 and Fig. 2.12). The detonation table of this work was calibrated only for a low mass WD with a flat density profile and thus very little overdrive. However, additional overdrive in models with heavier progenitors is taken into account in the detonation scheme of this work, as the final abundances are always determined from the post-processing step that reacts to an increased shock compression. For example, in Model $\mathrm{AWD3}_{256}^{\mathrm{det}}$ the post-processing yields ∼5% more IGEs than the hydrodynamic simulation and ∼6% more than the LBT estimate of Pfannes et al. (2010a) (when normalized to the same progenitor mass). Thus, the above conclusion that pure C/O detonation models can be excluded also in the case of rapid rotation of the progenitor should be robust.

Finally, it is stressed that the exact value of ρ_{NSE} is so crucial for supernova models, including also delayed detonations, that it should be further investigated in future (microscopical) studies. Those should especially take into account effects of the multidimensional structure and overdrive in the presence of density gradients. Studying the effects of different progenitor composition would also be of interest: lower C/O ratios or even O/Ne compositions could lead to an increase in ρ_{NSE} provided that such WDs could successfully detonate.

4.6. Results of the delayed detonation simulations

After the failure of both the deflagration and the pure detonation model in the context of rapidly rotating progenitors, the suitability of the delayed detonation scenario as model for Type Ia supernovae remains to be investigated in this section. In the following, results of several numerical simulations are presented. The discussion includes the evolution of the delayed detonations (Sect. 4.6.1), the explosion energetics (Sect. 4.6.2), nucleosynthesis and ejecta structure (Sect. 4.6.3), and the expected spectral features (Sect. 4.6.4).

4.6.1. Evolution of a DDT explosion

The evolution of Model $\mathrm{AWD3}_{512}^{\mathrm{DDT}}$ is discussed as representative example for all delayed detonation simulations (subscripts in the model names indicate the number of cells per dimension, superscripts the explosion mode). Figure 4.6 shows the density distribution for several different times. Locations of both the deflagration (white line) and the detonation flames (blue line) are marked. From the very beginning, the deflagration flame develops a pronounced anisotropy: it propagates much faster along the rotational axis (the z-axis) than perpendicular to it. According to Pfannes et al. (2010b), this has two reasons:

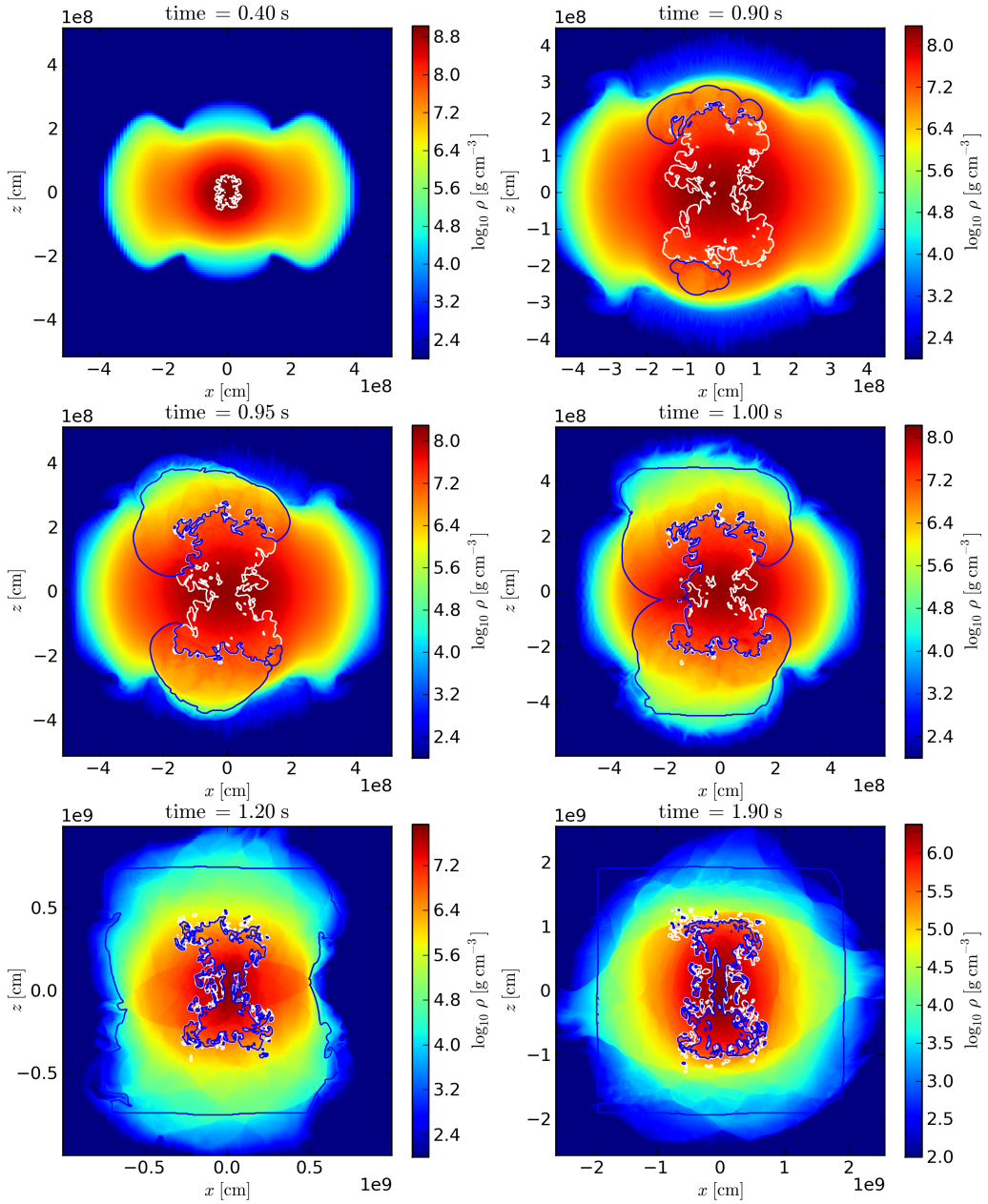

Figure 4.6.: Evolution of Model AWD3$^{\mathrm{DDT}}_{512}$. The density is color coded and white and blue contours mark the positions of the deflagration and the detonation flame, respectively. (After detonation extinction the outer edge of the former detonation front is passively advected with the flow. Due to the coarse zoning of the grid there, it develops a rectangular shape that has no physical meaning and also no influence on thermonuclear burning in the model.)

- First, the buoyant forces acting on the hot ashes are stronger in polar direction due to the effective gravitational acceleration g_{eff} being greater in polar than in equatorial direction. On the one hand, the steeper density decline in polar direction of the AWD models causes a greater gravitational acceleration g_{grav} there. On the other hand, the centrifugal acceleration that reduces the resultant acceleration from g_{grav} to g_{eff} is minimal in polar direction.

- Second, the turbulent spreading of the front perpendicular to the rotation axis is suppressed due to an effective angular momentum barrier: outflowing ashes have to gain angular momentum, while inflowing fuel has to lose angular momentum. Thus, Rayleigh–Taylor and Kelvin–Helmholtz instabilities are suppressed and the flow develops less turbulence. Consequently, the flame surface increase (by turbulent wrinkling) is smaller and less material is burnt.

At $t = 0.827$ s, when the flame approaches the border of the WD close to the poles, the DDT criterion is met for the first time. This happens at the trailing edge of the outer flame front as it is typical for DDTs (cf. Röpke & Niemeyer 2007). There, turbulence is most pronounced and, due to the low densities, the flame width is broadest. Therefore, the distributed burning regime in which turbulence changes the inner structure of the flame is reached earliest. The first DDTs are found almost synchronously close to the southern ($z = -1840$ km, $s = 1110$ km, $t = 0.827$ s) and the northern pole ($z = 1790$ km, $s = 1330$ km, $t = 0.830$ s). In total, the DDT criterion is met in $N_{\mathrm{DDT}} = 135$ points over a period of 0.155 s. Table 4.2 provides DDT and explosion parameters for all models: t_{DDT} and N_{DDT} denote the time at which the first DDT occurs and the total number of DDT points; $E_{\mathrm{nuc}}^{\mathrm{DDT}}$ and E_{nuc} are the nuclear energy released by the deflagration at the onset of the DDT and the total energy released by nuclear burning; $E_{\mathrm{tot}}^{\mathrm{ini}}$ and E_{tot} finally are the initial and final values of the total energy ($E_{\mathrm{tot}} = E_{\mathrm{grav}} + E_{\mathrm{int}} + E_{\mathrm{kin}}$) of the star.

After their polar initiation, the detonation fronts wrap around the deflagration ashes towards the equator and merge there. Reflections of the leading shocks cause an enhanced compression at this moment (cf. Fig. 4.6, $t = 1.20$ s). Note that all unburnt fuel in the equatorial plane and close to the center is consumed. As found in previous studies (Röpke & Niemeyer 2007), no large pockets of unburnt material are totally enclosed by deflagration ashes and thus unreachable by the detonation.

4.6.2. Explosion energetics

The explosion energies of all models are given in Table 4.2. As can be seen from the total energy evolution shown in Fig. 4.7, all delayed detonation models evolve similarly in time. After a relatively slow energy release in the initial deflagration phase, all curves show a kink at around 0.8–0.85 s, marking the onset of the detonation. From then on, nuclear energy is released much faster due to the supersonic detonation before the total energy saturates at around 1.3–1.5 s. All models produce significantly more energy than pure deflagrations (Pfannes et al.

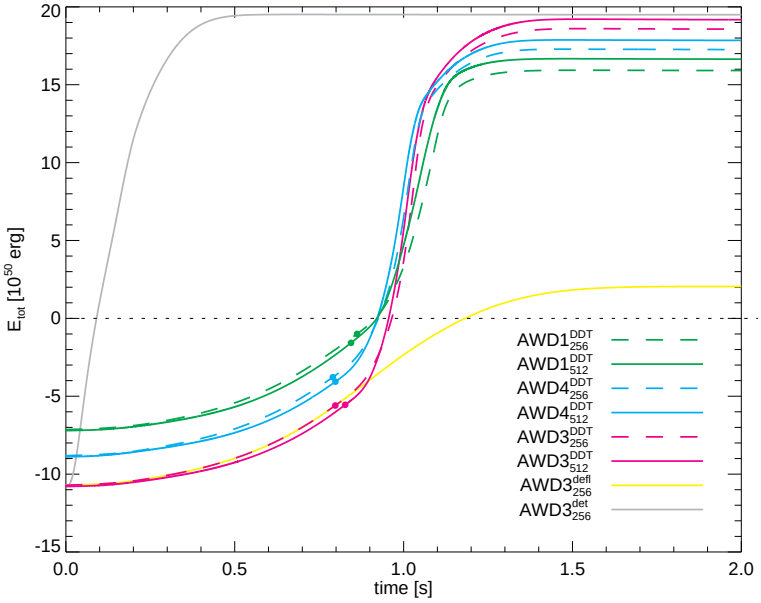

Figure 4.7.: Total energy evolution of all models.

2010b). For comparison, a pure deflagration, Model $\mathrm{AWD3}^{\mathrm{defl}}_{512}$ was calculated and is shown as yellow curve in Fig. 4.7. From the figure and also from the values given in Table 4.2 it is obvious that the *detonation phase dominates* the overall burning in all models: the total nuclear energy, E_{nuc}, is always several times larger than the energy released in the deflagration, $E^{\mathrm{DDT}}_{\mathrm{nuc}}$. For Model $\mathrm{AWD3}^{\mathrm{DDT}}_{512}$ this is also demonstrated by the fact that the DDT model releases only 2% less energy than the corresponding pure detonation model $\mathrm{AWD3}^{\mathrm{det}}_{256}$ (shown as gray curve in Fig. 4.7). A comparison of $E^{\mathrm{DDT}}_{\mathrm{nuc}}$ with the initial effective binding energy $E^{\mathrm{ini}}_{\mathrm{tot}}$ further illustrates that the deflagration does not lead to a significant pre-expansion of the star at the onset of the detonation.

The models form a series of growing rotational energy E_{rot} and total mass of the progenitor. The more massive models are more tightly bound and therefore start at lower initial total energy $E^{\mathrm{ini}}_{\mathrm{tot}}$, despite the greater E_{rot} (see Table 4.1). However, due to the fast and almost complete consumption of all the fuel in the explosive burning, all models get unbound already at ∼0.9–0.95 s and the more massive models reach larger final E_{tot}. Thus, within the series also the asymptotic kinetic energy of the ejecta, $E^{\mathrm{asymp.}}_{\mathrm{kin}} \approx E_{\mathrm{tot}}(t = 10\ \mathrm{s})$, increases.

As three-dimensional simulations are expensive, the resolution in the study is limited. Therefore, to test for numerical convergence, each well resolved simulation (512^3 grid cells) is compared with a lower resolved simulation (256^3 grid cells) of the same model (for energetics and nucleosynthesis, see Table 4.2). Generally, in the higher resolved models more nuclear energy is released (2.4–4.8%) and larger nickel masses are produced (4–11%). This is at the expense of IMEs and some unburnt

Table 4.2.: Explosion outcomes of all models.

Model	$\mathrm{AWD1}_{256}^{\mathrm{DDT}}$	$\mathrm{AWD1}_{512}^{\mathrm{DDT}}$	$\mathrm{AWD4}_{256}^{\mathrm{DDT}}$	$\mathrm{AWD4}_{512}^{\mathrm{DDT}}$	$\mathrm{AWD3}_{256}^{\mathrm{DDT}}$	$\mathrm{AWD3}_{512}^{\mathrm{DDT}}$	$\mathrm{AWD3}_{256}^{\mathrm{det}}$
t_{DDT} [s]	0.862	0.844	0.790	0.798	0.798	0.827	–
N_{DDT}	97	175	67	102	51	135	–
$E_{\mathrm{nuc}}^{\mathrm{DDT}}$ [10^{51} erg]	0.59	0.54	0.48	0.46	0.48	0.50	–
E_{nuc} [10^{51} erg]	2.29	2.38	2.59	2.66	2.92	2.99	3.03
$E_{\mathrm{tot}}^{\mathrm{ini}}$ [10^{51} erg]	−0.72	−0.72	−0.89	−0.89	−1.08	−1.08	−1.08
E_{tot} [10^{51} erg]	1.59	1.66	1.72	1.78	1.85	1.91	1.95
M_{IGE} [$M_\odot$]	1.16	1.28	1.47	1.54	1.66	1.72	1.90
$M_{^{56}\mathrm{Ni}}$ [$M_\odot$]	1.01	1.12	1.31	1.37	1.49	1.55	1.53
M_{IME} [$M_\odot$]	0.40	0.30	0.26	0.21	0.29	0.24	0.09
$M_{^{16}\mathrm{O}}$ [$M_\odot$]	0.05	0.04	0.04	0.03	0.05	0.03	0.01
$M_{^{12}\mathrm{C}}$ [$M_\odot$]	0.00	0.00	0.00	0.00	0.00	0.00	0.00
iron group elements							
$M_{^{54}\mathrm{Fe}}$ [$M_\odot$]	0.06	0.06	0.06	0.06	0.06	0.06	0.17
$M_{^{58}\mathrm{Ni}}$ [$M_\odot$]	0.04	0.05	0.05	0.05	0.05	0.05	0.12
$M_{^{52}\mathrm{Fe}}$ [$M_\odot$]	0.02	0.01	0.01	0.01	0.01	0.01	0.01
$M_{^{57}\mathrm{Ni}}$ [$M_\odot$]	0.01	0.01	0.02	0.02	0.02	0.02	0.04
$M_{^{56}\mathrm{Fe}}$ [$M_\odot$]	0.01	0.01	0.01	0.01	0.01	0.01	0.00
$M_{^{60}\mathrm{Zn}}$ [$M_\odot$]	0.00	0.00	0.01	0.01	0.01	0.01	0.01
$M_{^{55}\mathrm{Co}}$ [$M_\odot$]	0.00	0.01	0.01	0.01	0.01	0.01	0.02
intermediate mass elements							
$M_{^{28}\mathrm{Si}}$ [$M_\odot$]	0.22	0.16	0.15	0.11	0.16	0.13	0.05
$M_{^{32}\mathrm{S}}$ [$M_\odot$]	0.11	0.09	0.07	0.06	0.08	0.07	0.02
$M_{^{36}\mathrm{Ar}}$ [$M_\odot$]	0.02	0.02	0.01	0.01	0.02	0.01	0.00
$M_{^{40}\mathrm{Ca}}$ [$M_\odot$]	0.02	0.02	0.01	0.01	0.02	0.01	0.00
$M_{^{24}\mathrm{Mg}}$ [$M_\odot$]	0.02	0.01	0.01	0.01	0.01	0.01	0.00
$M_{^{20}\mathrm{Ne}}$ [$M_\odot$]	0.00	0.00	0.00	0.00	0.00	0.00	0.00

carbon. More nickel can be produced if the detonation occurs at higher densities, i.e., at a lower degree of pre-expansion due to the deflagration phase. Another effect that acts in the same direction is a faster spread of the detonation flame by a larger number of points that meet the DDT criterion (those might potentially also cover a greater surface in front of the deflagration flame). Regarding Fig. 4.7, both effects seem to contribute to some degree: the higher resolved models (solid lines) all have a slightly slower energy release in the deflagration phase (the DDT is marked on each curve by a filled circle) and a faster accelerating energy release in the initial detonation phase than their lower resolved counterparts (dashed lines). The data given in Table 4.2 also confirm this: in the case of both the AWD1 and and the AWD4 models the higher resolved simulations produce less nuclear energy $E_{\mathrm{nuc}}^{\mathrm{DDT}}$ in the deflagration before the DDT sets in than the lower resolved ones. Also, the number of DDT points N_{DDT} is always significantly greater in the high-resolution runs. The applied DDT criterion is known to show some resolution dependence. Due to the influence of turbulent structures that depend on the spatial resolution of the simulation, numerical convergence is not expected. In this sense, the agreement of higher and lower resolved simulations in Fig. 4.7 appears quite reasonable. For future studies, however, resolution independent DDT criteria should be developed.

4.6.3. Nucleosynthesis and ejecta structure

Detailed nucleosynthetic abundances have been calculated in the post-processing step. They are given in Table 4.2. Due to their high initial masses and densities and the dominance of the detonation phase, all models produce very large nickel masses in the range of 1.0–1.55 $M_{\odot}$. But, because of the flat density profile and some pre-expansion by the deflagration burning, the detonation phase also produces a significant amount of IMEs. In total, IME masses ranging from 0.21–0.40 $M_{\odot}$ are found. Remarkably, despite being more massive, Model AWD3$_{512}^{\mathrm{DDT}}$ produces more IMEs (0.24 $M_{\odot}$) than Model AWD4$_{512}^{\mathrm{DDT}}$ (0.21 $M_{\odot}$), as the progenitor has more mass at low densities $\lesssim 10^7$ g cm^{-3} due to the more rapid rotation. Carbon is almost completely exhausted in the models and only small amounts of oxygen (0.03–0.05 $M_{\odot}$) are found. Note that Model AWD3$_{256}^{\mathrm{DDT}}$ produces almost the same nickel and IME masses as the pure detonation models of Pfannes et al. (2010a) that used the same progenitor model and were based on relatively high NSE transition densities (see Sect. 4.5). However, there are significant differences in the distribution of neutron-rich IGEs that reflect the differences in the burning modes of both models.

Regarding the range of nickel masses and the significant amounts of IMEs, the models seem to be good candidates for very super-luminous Type Ia supernovae with $M_{^{56}\mathrm{Ni}} \gtrsim 1.2\ M_{\odot}$ like SN 2003fg (Howell et al. 2006) that were suggested to originate from "super-Chandrasekhar" mass ($M \gtrsim 1.4\ M_{\odot}$) progenitors. The suitability of the models for this channel together with the expected spectral properties is discussed in Sect. 4.6.4.

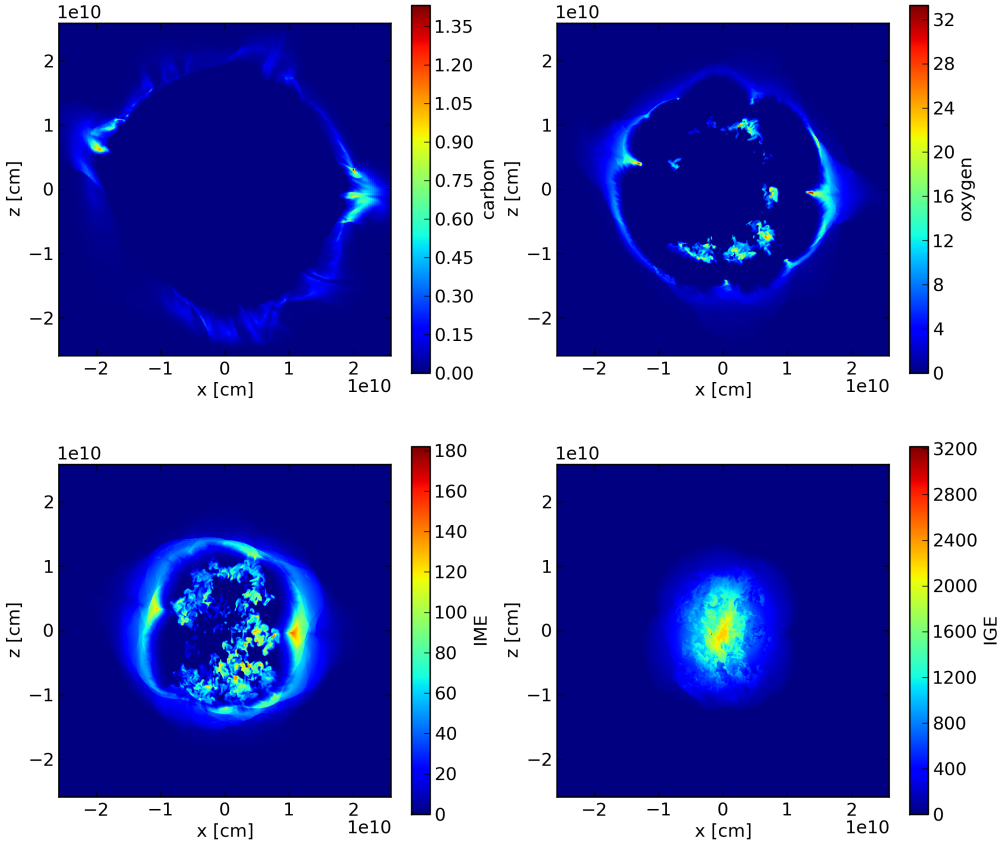

Figure 4.8.: Final composition of Model AWD1$^{\mathrm{DDT}}_{512}$ indicated by the fractional densities ρX_i of species in the hydrodynamic simulation.

The nucleosynthetic abundances from the post-processing are found to be fairly consistent with the reduced species information $\boldsymbol{X}^{\mathrm{red}}$ directly obtained from the hydrodynamic simulations (nickel masses differ not more than 5%). Therefore, the analysis of the spatial distribution of the explosion ejecta is restricted to $\boldsymbol{X}^{\mathrm{red}}$. Figures 4.8 to 4.10 show the fractional densities ρX_i of the reduced species ^{12}C, ^{16}O, IMEs, and IGEs for all three better resolved rotating DDT models. Unburnt carbon and oxygen are present only at the very low density outer regions, where the detonation flame extinguishes. A lot of IGEs have been produced in central regions, but they show an asymmetric distribution extending further towards polar than towards equatorial directions due to the anisotropic propagation of the deflagration flame. Complex asymmetric structures can be assigned to deflagration burning, whereas the smooth equatorial outer parts stem from the detonation.

All simulations produce a pronounced equatorial bulge of IMEs that originates from the extended low density regions of the rapidly rotating WDs. A similar structure is found in pure detonation models (see Fig. 4.4). In the models of this

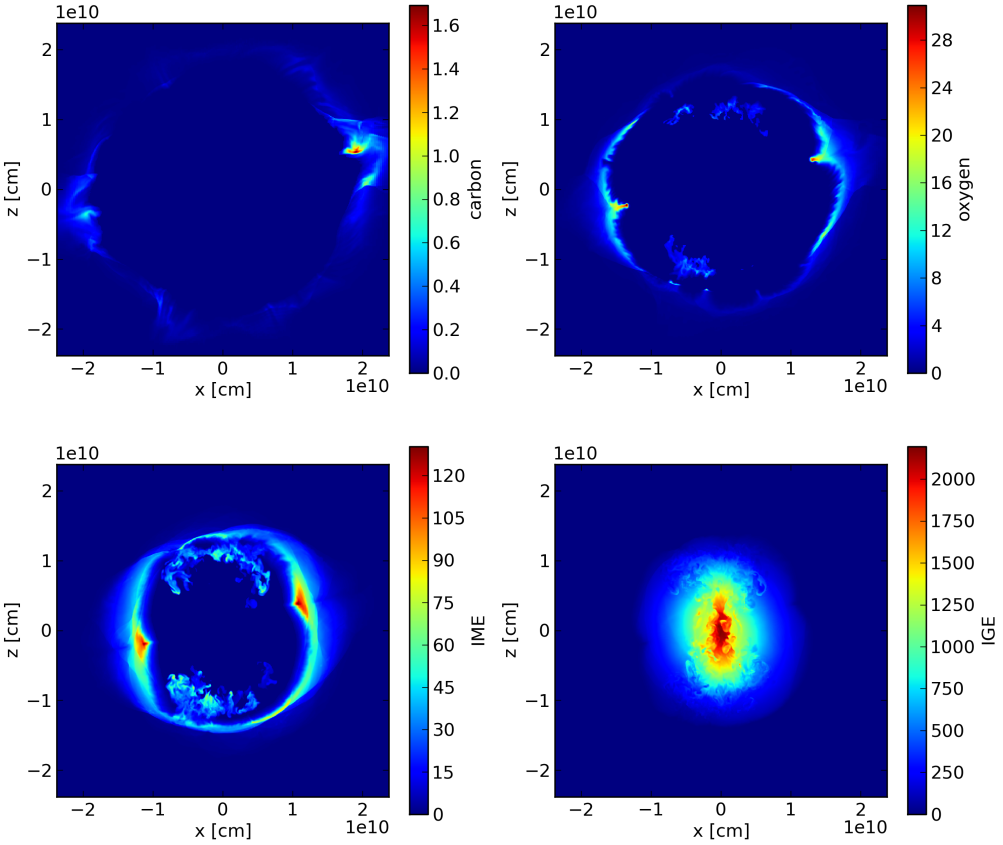

Figure 4.9.: Final composition of Model AWD4$^{\mathrm{DDT}}_{512}$ indicated by the fractional densities ρX_i of species in the hydrodynamic simulation.

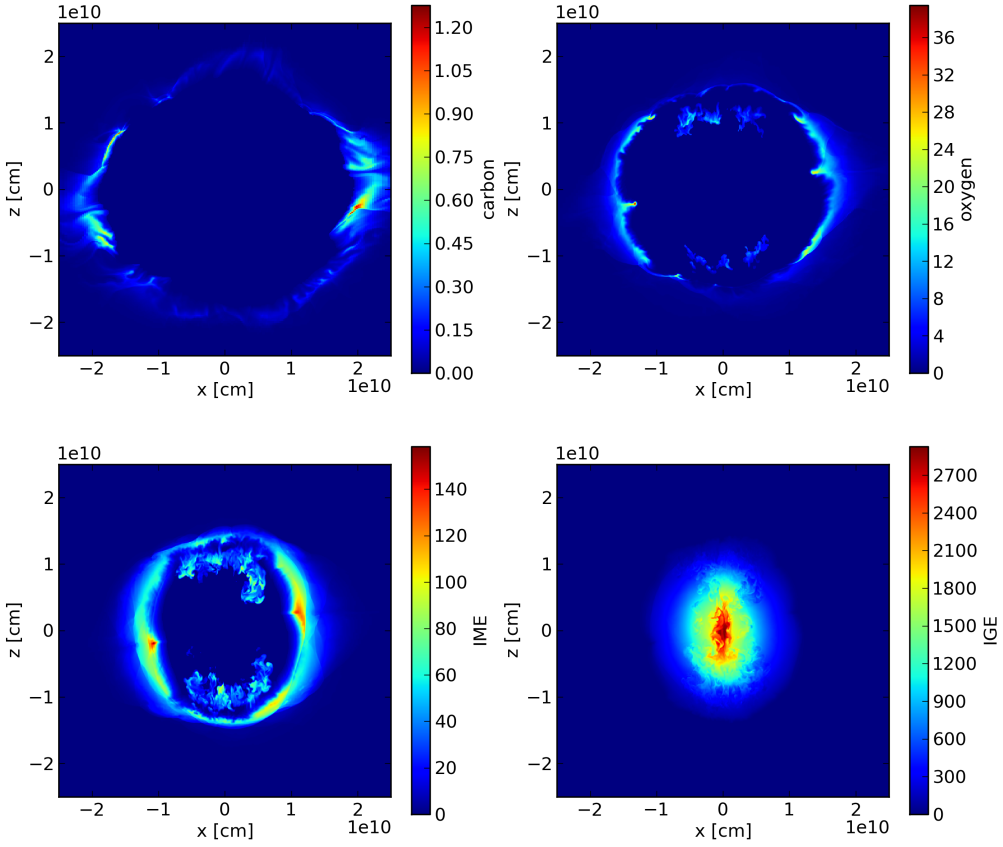

Figure 4.10.: Final composition of Model AWD3$^{\mathrm{DDT}}_{512}$ indicated by the fractional densities ρX_i of species in the hydrodynamic simulation.

work the detonation produces also significant amounts of IMEs in polar direction, but in these directions they are much less extended. Close to the poles, where the DDT started, the deflagration also produces some IMEs which are intermixed with IGEs there. Here, Model AWD1$_{512}^{\mathrm{DDT}}$ differs from the other models, as the deflagration leaves behind significantly more IMEs that seem to be intermixed with IGEs almost over the whole burnt volume.

Also some secondary asymmetries are found in the detonation products: at several angles IMEs, carbon, and oxygen have higher densities and form cusps that reach deeper into the core of the ejecta. At the same locations high densities also reach further outwards. These structures are due to the aforementioned collisions of independent detonation fronts that lead to higher local densities and an ejection of the burning products perpendicular to the collision direction.

4.6.4. Expected spectral features

Synthetic spectra and light curves of the models are not yet available due to resolution problems of the tracer particle method in three dimensions: test calculations of synthetic observables are not reliable up to now, as they depend on the mapping scheme that is used to project the coarse tracer information on the Cartesian grid of the radiative transfer code. Therefore, expected spectral features are discussed only by analyzing the final velocity distribution of the ejecta here.

Figure 4.11 shows the mass distribution of the main groups of elements in velocity space both for an angle range around the equatorial plane (a) and around the northern polar axis (b) of all three better resolved DDT models. For all models the velocity distributions are fairly similar: the increase in gravitational binding energy within the series seems to compensate almost exactly for the growing nuclear energy release in this respect. Due to the lower explosion energies at the same total masses, the lower resolved simulations show somewhat lower velocities. Here, only the better resolved models are presented, as for higher resolutions even somewhat greater velocities than in Fig. 4.11 would be expected.

In the figure, the large amounts of IGEs of all models show a broad distribution around a peak value at $\sim$7500 km s^{-1}. As expected from Figs. 4.8 to 4.10, they reach out to slightly higher velocities in polar directions. In equatorial directions IMEs peak around 13 000–14 000 km s^{-1} and are not found below 10 000–12 000 km s^{-1}. Towards the poles IMEs are less frequent, peak around 15 000 km s^{-1}, and are intermixed into the IGE core slightly deeper.

High velocities above 20 000 km s^{-1} are reached in equatorial directions by both IMEs and oxygen. Therefore, the models could potentially explain observed high velocity features (cf. Mazzali et al. 2005). However, this is not further discussed here, as the velocities, especially those of the IME maximum, are significantly too high for the models to be candidates for normal Type Ia supernovae. According to their nickel masses, the models can only be compared with the peculiar class of extremely super-luminous and slowly evolving events, like SNe 2003fg, 2006gz, 2007if, and 2009dc (Howell et al. 2006; Hicken et al. 2007; Scalzo et al. 2010;

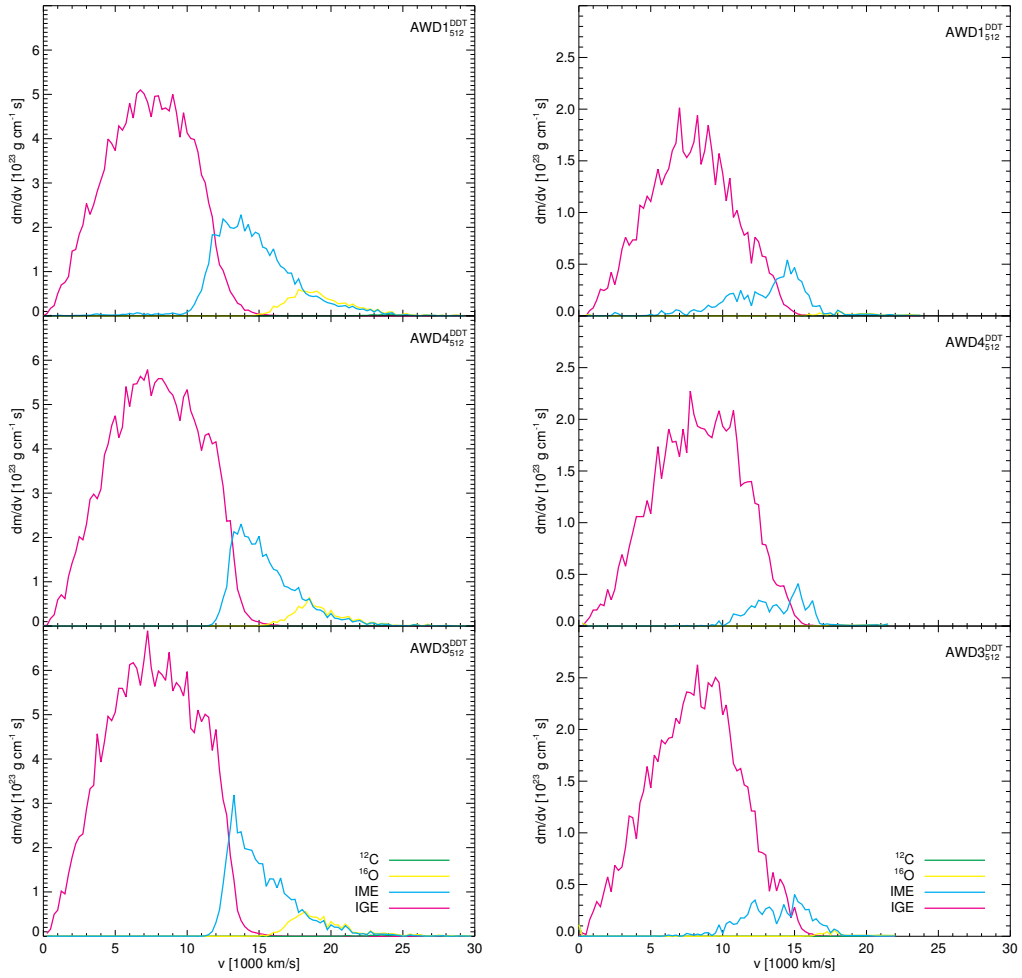

(a) equator plane, $|\theta - \frac{\pi}{2}| < \frac{\pi}{16}$ (b) northern polar axis, $\theta < \frac{\pi}{8}$

Figure 4.11.: Mass distribution of the main groups of elements in velocity space for selected ranges of the polar angle θ. The velocity bin size is $\Delta v = 250\ \mathrm{km\,s^{-1}}$.

Silverman et al. 2010). Despite their brightness, these events generally show very low Si II line velocities in their spectra of ∼8000–9000 km s^{-1} and below. This is clearly incompatible with the distribution of IMEs in the models. SN 2006gz is an exception in this respect. It shows relatively normal Si II velocities at maximum light, but its very low early phase velocities of 13 000 km s^{-1} (which should resemble the maximum velocities of silicon in the outer ejecta) disagree with the maximum model silicon velocities that are at least 17 000 km s^{-1} for all models and lines of sight.

Also, strong carbon absorption lines are found in the early spectra of very super-luminous observations suggesting a thick layer of unburnt carbon in the outer ejecta. This finding is also in contradiction with the complete carbon consumption of the models. Thus, *the models have to be excluded as candidates for observed Type Ia supernovae.*

To avoid the above mentioned spectral problems, larger total masses of the progenitor have been suggested (see, e.g., Howell et al. 2006). This could allow for large nickel masses and, at the same time, low velocities due to the increased binding energy of the system. However, it would require a totally different progenitor scenario (like a WD merger) with an appropriate fraction of low density material to produce significant amounts of both IMEs and unburnt carbon.

4.7. Summary

The influence of rapid differential rotation of the progenitor WD on the delayed detonation scenario has been investigated. To this end, full-star hydrodynamic simulations have been carried out in three dimensions using three initial rotators that cover the expected range of rotational energies. A multi-spot ignition scenario was chosen for the deflagration ignition and the DDT parametrization is based on a critical Karlovitz number of 250.

Several important effects of rotation on the explosion scenario are found to be the same as for the pure deflagration scenario (Pfannes et al. 2010b). The progenitor stars are significantly more massive than non-rotating Chandrasekhar-mass WDs, which allows greater explosion energies in the models. But, there is also more low density material ($\rho \lesssim 10^7$ g cm^{-3}) that can potentially be burnt to IMEs. Deflagration burning is weak and anisotropic with a preferred propagation direction towards the stellar poles (parallel to the rotation axis).

In the delayed detonation models the deflagration quickly spreads towards the poles before it can significantly propagate in equatorial direction, thus, the DDT is always found to occur close to the poles (in multiple spots) and when large fractions of the star are still unburnt. The pre-expansion of the remaining fuel by the deflagration is also found to be relatively limited. Therefore, in all models the detonation phase dominates the burning. Consequently, very bright explosions ensue ($M_{^{56}\mathrm{Ni}} > 1\ M_\odot$) that could be potential candidates for extremely super-luminous Type Ia supernovae (they are too bright for normal explosions). However,

the velocities of IMEs are found to be significantly too high when compared with the low line velocities that are found in observed spectra of this class. It is thus concluded that the delayed detonation scenario in rapidly rotating WDs is incompatible with observed Type Ia supernovae.

These results are *robust* with respect to several uncertainties that are still present in the models:

- Details of the rotation laws will not allow for much change in the explosion outcomes. Within the series of models that covers a broad range of rotational energies, the expected spectral signatures are found to be very similar.
- As the chosen ignition conditions are known to produce strong deflagrations in non-rotating scenarios, a modification in this sense could only lead to even stronger detonations.
- The DDT criterion may still be uncertain. But, the dominant effect in the models is the anisotropy of the deflagration. The flame will always quickly reach the low density edge of the WD in polar directions and the DDT has to occur close to that instant. Due to the very slow propagation of the deflagration in the equatorial plane, a somewhat later DDT will not cause much more pre-expansion of unburnt fuel there.

The problem of too high ejecta velocities was found to be even more serious in the case of pure detonations. This was shown in a pure detonation simulation of the AWD3 rotator similar to Pfannes et al. (2010a). Due to the significantly lower NSE transition density of the improved detonation scheme of this work, much higher ejecta velocities and less IMEs than in Pfannes et al. (2010a) were found. As the delayed detonations showed too high IME velocities for the whole series of initial rotators, the same trend will also hold for the corresponding pure detonation models. Thus, the pure detonation scenario is excluded together with the delayed detonations in the context of rapidly rotating progenitors.

Apart from speculations of lower C/O ratios and O/Ne compositions in the progenitor WDs (see the discussion at the end of Sect. 4.5), only significantly less rapidly rotating WD progenitors could be suitable to model Type Ia supernova explosions. For example, rotation might be a parameter to regulate the strength of the detonation phase within "normal" delayed detonation models at $M_{\mathrm{Ch}} \approx 1.4\ M_{\odot}$: by reducing the strength of the deflagration phase the detonations could be enhanced. This could allow for modeling bright normal Type Ia supernovae. The extremely super-luminous events, however, are out of reach. Finally, a restriction of rapid rotation of supernova progenitors is also plausible for another reason: Yoon & Langer (2004) totally neglect effects of magnetic fields; those would, however, most likely slow down rotation.

5. Concluding remarks

Due to their importance in almost any currently discussed scenario for Type Ia supernovae, detonations and their accurate modeling in the degenerate matter of white dwarf stars have been investigated in this thesis. To this end, the detonation scheme of an existing supernova code was improved and tested for consistency. Moreover, the new scheme was applied in multidimensional full-star hydrodynamic simulations of Type Ia supernovae that aim at a better theoretical understanding of the nature and the variety of these thermonuclear explosions. Both double-detonations in sub-Chandrasekhar-mass WDs and delayed detonations of rapidly rotating Chandrasekhar-mass WDs were explored. In the following, the main results of this thesis are summarized and their significance in the context of Type Ia supernova modeling is discussed. Afterwards, possibilities for future improvements are suggested.

5.1. Summary and conclusions

Detonation model

Detonations in this work are modeled in the framework of full-star hydrodynamic simulations assuming the discontinuity approximation, thus, their internal structure is unresolved. Due to the iterative calibration with the post-processing network, the applied front tracking scheme however allows a consistent energy release and explosion dynamics. Thus, an accurate nucleosynthesis is expected from the post-processing of the Lagrangian tracer particles followed in the explosion simulations. Importantly, detonations in both degenerate C/O and helium can now be accurately and efficiently modeled even in the incomplete burning regimes. The scheme was also shown to behave well in the case of changes in the shock strength when the detonation propagates through density gradients in the star.

Sub-Chandrasekhar models

The improved detonation model was first applied to investigate the double-detonation sub-Chandrasekhar model for Type Ia supernovae in two-dimensional hydrodynamic simulations. In this scenario, an assumed detonation in an accreted helium shell was shown to robustly trigger a secondary detonation of a C/O-WD core even in the most conservative case of minimum shell masses that might still detonate. Consequently, if a helium detonation occurs, a C/O detonation is found to be virtually inevitable.

Due to the just mentioned robustness of the triggering mechanism, the whole model series of this study, which covers a wide range of possible progenitor masses,

successfully explodes and thus also produces a wide range of ^{56}Ni masses of 0.2–1.1 $M_\odot$. Thus, sub-Chandrasekhar-mass explosions are not found to be subluminous: they can be bright enough to cover the whole range of normal Type Ia supernovae.

Due to the one-point ignition in the helium shell and, more importantly, the off-center C/O detonation, the shell detonation products are found to be very asymmetrically distributed. The helium detonation nucleosynthesis differs significantly from previous publications: the IGEs ^{52}Fe, ^{48}Cr, and ^{44}Ti are most abundant and more than half of the helium remains unburnt.

Radiative transfer calculations of Kromer et al. (2010) show that the synthetic observables of all models, despite their minimum shell masses, strongly disagree with observed Type Ia supernovae due to the presence of the helium detonation products in the outer layers: ^{44}Ti and ^{48}Cr efficiently absorb radiation at blue wavelengths and redistribute it towards redder parts of the spectrum. Therefore, both light curves and spectra are found to be too red and lines of ^{44}Ti and ^{48}Cr dominate the spectrum at maximum brightness instead of the expected lines of IMEs like silicon. Thus, the models in their current form with shells of pure helium have to be excluded as candidates for Type Ia supernovae. Radiative transfer simulations of toy models constructed from one model by removing the shell detonation products or by changing the shell nucleosynthesis, however, make clear that good agreement with observables of normal Type Ia supernovae is possible, but strongly depends on details of the shell nucleosynthesis.

Rapidly rotating Chandrasekhar models

In another study, explosions of rapidly differentially rotating WDs at the thus increased M_{Ch} were explored in three-dimensional simulations. With the new detonation scheme, pure detonations were shown to be incompatible with the Chandrasekhar-mass model even in the case of rapid rotation. Despite the increased fraction of low density material in the WD due to rapid rotation (see Fig. 1.1 b), too little IMEs were produced and the IME velocities were significantly too high compared to the low silicon line velocities of super-luminous Type Ia supernovae. Pfannes et al. (2010a) claim good agreement with observations in a very similar pure detonation model, but they apply a very high NSE transition density in their C/O detonations, which was shown to be very unlikely in this work: spherically expanding detonations in high mass WDs are found to be strongly overdriven, which leads to even lower NSE transition densities than in the steady state unsupported case.

Also, delayed detonations were investigated in rapidly rotating progenitors. As previously reported by Pfannes et al. (2010b), the deflagration is very weak in all studied models and preferentially propagates towards the stellar poles (in the direction of the rotation axis). Therefore, the DDT is triggered close to the poles with little pre-expansion of the star and the detonation totally dominates the explosion. Although producing IMEs in much larger amounts, a delayed detonation cannot alleviate the second problem found for pure detonations: the velocities of

IMEs are still too high. Thus, delayed detonations have to be excluded as model for Type Ia supernovae in the context of rapidly rotating WDs when compared to current observational data.

5.2. Implications for Type Ia supernova modeling

Detonation model

As already mentioned, overdrive effects were found to be important in C/O detonations propagating down density gradients of massive WDs. Due to shock strengthening, the NSE transition is shifted to lower densities resulting in an increased IGE production. This might increase the nickel masses of previous delayed detonation simulations that do not take overdrive effects into account.

In the case of low density helium detonations, the multidimensional propagation in the lateral direction around the WD core was found to produce significantly different results than one-dimensional spherical shell detonations. Due to the weaker detonation shock, the matter is burnt at lower densities and temperatures resulting in lower average mass numbers. Thus, one-dimensional simulations may predict wrong nucleosynthesis and overestimate IGEs.

Sub-Chandrasekhar models

The robustness of the triggering mechanism of a secondary core detonation together with the ensuing wide range of possible nickel masses that can be covered by double-detonation sub-Chandrasekhar models are very important prerequisites for a scenario to successfully explain normal Type Ia supernovae. Based on this foundation and the assumption that a realization of the scenario exists, which is not dominated by the explosion products of the outer shell, Sim et al. (2010) have shown that a series of detonations of pure C/O WDs can reproduce both spectra and light curves of a significant part of the parameter space of normal Type Ia supernovae well. They even found trends in the observable characteristics such as the "Phillips relation" to be reproduced. If the helium detonation could be proven to occur robustly in a certain fraction of the potential progenitor systems, then, according to population synthesis calculations (Ruiter et al. 2009), the sub-Chandrasekhar scenario could account for a significant part of the observed Type Ia supernova explosions.

A future requirement for double-detonation sub-Chandrasekhar modeling is to avoid the dominance of IGEs on the spectral signatures. As already discussed in detail in Sect. 3.4, this could either be achieved by changes in the nucleosynthesis of the helium shell detonation (due to more realistic initial shell compositions) or by improved radiative transfer simulations that include non-thermal excitation and ionization effects and might reduce the fluorescence effects of ^{44}Ti and ^{48}Cr. Realistic helium shell compositions may include a significant enrichment with ^{12}C or other α-chain elements due to dredge-up effects from the C/O core, the accretion of already enriched material from the companion, or volume burning in

the accreted shell before thermonuclear runaway.

The crucial influence of the helium shell nucleosynthesis on the observables in the sub-Chandrasekhar models identified in this work should be a warning: accurate detonation modeling can be essential and should be an objective in general in supernova modeling.

Rapidly rotating Chandrasekhar models

The inconsistency of the expected spectral features of pure and delayed detonations and also pure deflagrations (Pfannes et al. 2010b) with observations suggests either that rapid differential rotation does not occur in potential progenitor systems of Type Ia supernovae (e.g. due to effects like magnetic braking or depletion of the donor mass or accretion rate), or that rapid rotation prevents the explosion as thermonuclear supernova (e.g. by avoiding C/O ignition or by favoring conditions for accretion induced collapse).

5.3. Future work

The promising results of the double-detonation sub-Chandrasekhar simulations motivate further investigation of this scenario. As made clear above, a primary goal would be to figure out whether the dominance of the IGEs in the synthetic spectra can be avoided. To this end, the suggestions for improvements already discussed in the last section should be tested. This could involve the following steps:

- Simulations of the details of the accretion process should determine realistic shell compositions and the conditions at shell ignition.
- If this is not feasible in the near future, a parameter study of the effects of potential shell compositions on the synthetic spectra with the same setup as in this work and newly calibrated detonation tables could be carried out more easily.
- The success of all modeling relies on accurate radiative transfer simulations. As mentioned above, the inclusion of non-thermal excitation and ionization effects could be of crucial importance to alleviate the restrictive dependence on shell nucleosynthesis.

As already discussed in detail in Sect. 2.5.4, the double-detonation sub-Chandrasekhar models may also be improved by refining the detonation scheme of this work: a departure from the discontinuity approximation and the inclusion of a small nuclear network would ensure a correct energy release independent of the initial composition, potential volume burning effects, changes of the shock strength, and rapid expansion behind the front. Also, a potential overestimation of the maximum temperatures due to the instantaneous energy release would be avoided. Most of these changes tend to produce lower temperatures and thus less IGEs in the helium shell detonation.

In summary, there seems to be enough room for improvement of the double-detonation sub-Chandrasekhar simulations of this work. Thus, the scenario remains a promising candidate for explaining normal Type Ia supernovae. But, it still provides several challenges that have to be addressed.

A. Abbreviations

The following abbreviations are frequently used in the text:

AWD accreting white dwarf

DDT delayed detonation transition

IME intermediate mass element

IGE iron group element

$M_\odot$ solar mass

M_{Ch} Chandrasekhar mass

NSE nuclear statistical equilibrium

WD white dwarf

Bibliography

Althaus, L. G., Serenelli, A. M., Panei, J. A., et al. 2005, A&A, 435, 631

Arnett, D. 1997, in NATO ASIC Proc. 486: Thermonuclear Supernovae, ed. P. Ruiz-Lapuente, R. Canal, & J. Isern, 405–424

Arnett, W. D. 1969, Ap&SS, 5, 180

Arnett, W. D., Truran, J. W., & Woosley, S. E. 1971, ApJ, 165, 87

Astier, P., Guy, J., Regnault, N., et al. 2006, A&A, 447, 31

Benz, W. 1997, in NATO ASIC Proc., Vol. 486, Thermonuclear Supernovae, ed. P. Ruiz-Lapuente, R. Canal, & J. Isern (Dordrecht: Kluwer Academic Publishers), 457–474

Bildsten, L., Shen, K. J., Weinberg, N. N., & Nelemans, G. 2007, ApJ, 662, L95

Boisseau, J. R., Wheeler, J. C., Oran, E. S., & Khokhlov, A. M. 1996, ApJ, 471, L99

Branch, D., Fisher, A., & Nugent, P. 1993, AJ, 106, 2383

Branch, D., Romanishin, W., & Baron, E. 1996, ApJ, 465, 73

Cappellaro, E., Evans, R., & Turatto, M. 1999, A&A, 351, 459

Cassisi, S., Iben, I. J., & Tornambe, A. 1998, ApJ, 496, 376

Clavin, P. 2004, Chaos, 14, 825

Colella, P. & Glaz, H. M. 1985, Journal of Computational Physics, 59, 264

Colella, P. & Woodward, P. R. 1984, Journal of Computational Physics, 54, 174

Colgate, S. A. & McKee, C. 1969, ApJ, 157, 623

Courant, R. & Friedrichs, K. O. 1948, Supersonic Flow and Shock Waves (New York: Springer Verlag)

Dgani, R. & Livio, M. 1990, ApJ, 361, 540

Domínguez, I., Höflich, P., & Straniero, O. 2001, ApJ, 557, 279

Eriguchi, Y. & Müller, E. 1985, A&A, 146, 260

Fickett, W. & Davis, C. 1979, Detonation, ed. D. H. Sharp & L. M. Simmons, Los Alamos Series in Basic and Applied Sciences (University of California Press)

Filippenko, A. V. 1997a, ARA&A, 35, 309

Filippenko, A. V. 1997b, in NATO ASIC Proc., Vol. 486, Thermonuclear Supernovae, ed. P. Ruiz-Lapuente, R. Canal, & J. Isern (Dordrecht: Kluwer Academic Publishers), 1–32

Filippenko, A. V., Richmond, M. W., Branch, D., et al. 1992a, AJ, 104, 1543

Filippenko, A. V., Richmond, M. W., Matheson, T., et al. 1992b, ApJ, 384, L15

Fink, M., Hillebrandt, W., & Röpke, F. K. 2007, A&A, 476, 1133

Forcada, R. 2007, in Supernovae: lights in the darkness

Forcada, R., Garcia-Senz, D., & José, J. 2006, in International Symposium on Nuclear Astrophysics - Nuclei in the Cosmos

Fryxell, B., Olson, K., Ricker, P., et al. 2000, ApJS, 131, 273

Fryxell, B. A., Müller, E., & Arnett, W. D. 1989, Hydrodynamics and nuclear burning, MPA Green Report 449, Max-Planck-Institut für Astrophysik, Garching

Gamezo, V. N., Wheeler, J. C., Khokhlov, A. M., & Oran, E. S. 1999, ApJ, 512, 827

García-Senz, D., Bravo, E., & Woosley, S. E. 1999, A&A, 349, 177

Gil-Pons, P. & García-Berro, E. 2001, A&A, 375, 87

Gilfanov, M. & Bogdán, Á. 2010, Nature, 463, 924

Godunov, S. K. 1959, Matematicheskii Sbornik, 47, 271

Golombek, I. & Niemeyer, J. C. 2005, A&A, 438, 611

Guderley, G. 1942, Luftfahrtforschung, 19, 302

Guillochon, J., Dan, M., Ramirez-Ruiz, E., & Rosswog, S. 2010, ApJ, 709, L64

Hamuy, M., Phillips, M. M., Maza, J., et al. 1995, AJ, 109, 1

Hamuy, M., Phillips, M. M., Suntzeff, N. B., et al. 1996, AJ, 112, 2391

Harkness, R. P. & Wheeler, J. C. 1990, in Supernovae, ed. A. G. Petschek (New York: Springer-Verlag), 1–29

Hicken, M., Garnavich, P. M., Prieto, J. L., et al. 2007, ApJ, 669, L17

Hillebrandt, W. & Niemeyer, J. C. 2000, ARA&A, 38, 191

Höflich, P. & Khokhlov, A. 1996, ApJ, 457, 500

Homeier, D., Koester, D., Hagen, H., et al. 1998, A&A, 338, 563

Howell, D. A. 2001, ApJ, 554, L193

Howell, D. A., Sullivan, M., Nugent, P. E., et al. 2006, Nature, 443, 308

Hoyle, F. & Fowler, W. A. 1960, ApJ, 132, 565

Iben, Jr., I. & Tutukov, A. V. 1989, ApJ, 342, 430

Imshennik, V. S. & Khokhlov, A. M. 1984, Soviet Astronomy Letters, 10, 262

Iwamoto, K., Brachwitz, F., Nomoto, K., et al. 1999, ApJS, 125, 439

Kasen, D., Röpke, F. K., & Woosley, S. E. 2009, Nature, 460, 869

Khokhlov, A. M. 1984, Soviet Astronomy Letters, 10, 123

Khokhlov, A. M. 1988, Ap&SS, 149, 91

Khokhlov, A. M. 1989, MNRAS, 239, 785

Khokhlov, A. M. & Érgma, É. V. 1985, Astrofizika, 23, 605

Kromer, M. & Sim, S. A. 2009, MNRAS, 398, 1809

Kromer, M., Sim, S. A., Fink, M., et al. 2010, ApJ, 719, 1067

Kuchner, M. J., Kirshner, R. P., Pinto, P. A., & Leibundgut, B. 1994, ApJ, 426, L89

Landau, L. D. & Lifschitz, E. M. 1991, Lehrbuch der theoretischen Physik, Vol. 6, Hydrodynamik (Berlin: Akademie Verlag)

Langanke, K. & Martinez-Pinedo, G. 2000, Nuclear Physics A, 673, 481

Langer, N., Deutschmann, A., Wellstein, S., & Höflich, P. 2000, A&A, 362, 1046

Lee, J. H. S., Knystautas, R., & Yoshikawa, N. 1978, Acta Astronautica, 5, 971

Leibundgut, B., Kirshner, R. P., Phillips, M. M., et al. 1993, AJ, 105, 301

Li, W., Leaman, J., Chornock, R., et al. 2010, ArXiv e-prints

Livne, E. 1990, ApJ, 354, L53

Livne, E. 1997, in NATO ASIC Proc. 486: Thermonuclear Supernovae, ed. P. Ruiz-Lapuente, R. Canal, & J. Isern, 425–440

Livne, E. & Arnett, D. 1995, ApJ, 452, 62

Livne, E., Asida, S. M., & Höflich, P. 2005, ApJ, 632, 443

Livne, E. & Glasner, A. S. 1990, ApJ, 361, 244

Livne, E. & Glasner, A. S. 1991, ApJ, 370, 272

Maier, A. & Niemeyer, J. C. 2006, A&A, 451, 207

Mazzali, P. A., Benetti, S., Altavilla, G., et al. 2005, ApJ, 623, L37

Mazzali, P. A., Danziger, I. J., & Turatto, M. 1995, A&A, 297, 509

Mazzali, P. A., Lucy, L. B., Danziger, I. J., et al. 1993, A&A, 269, 423

Mulder, W., Osher, S., & Sethian, J. A. 1992, Journal of Computational Physics, 100, 209

Müller, E. & Eriguchi, Y. 1985, A&A, 152, 325

Müller, E. & Steinmetz, M. 1995, Computer Physics Communications, 89, 45

Nelemans, G. 2005, in Astronomical Society of the Pacific Conference Series, Vol. 330, The Astrophysics of Cataclysmic Variables and Related Objects, ed. J.-M. Hameury & J.-P. Lasota, 27–40

Niemeyer, J. C. & Hillebrandt, W. 1995, ApJ, 452, 769

Niemeyer, J. C., Hillebrandt, W., & Woosley, S. E. 1996, ApJ, 471, 903

Niemeyer, J. C. & Woosley, S. E. 1997, ApJ, 475, 740

Nomoto, K. 1982, ApJ, 253, 798

Nomoto, K. & Kondo, Y. 1991, ApJ, 367, L19

Nomoto, K., Sugimoto, D., & Neo, S. 1976, Ap&SS, 39, L37

Nomoto, K., Thielemann, F.-K., & Yokoi, K. 1984, ApJ, 286, 644

Nugent, P., Baron, E., Branch, D., Fisher, A., & Hauschildt, P. H. 1997, ApJ, 485, 812

Osher, S. & Sethian, J. A. 1988, Journal of Computational Physics, 79, 12

Paczyński, B. 1967, Acta Astronomica, 17, 287

Pagel, B. E. J. 1970, Vistas in Astronomy, 12, 313

Pakmor, R., Kromer, M., Röpke, F. K., et al. 2010, Nature, 463, 61

Pastorello, A., Mazzali, P. A., Pignata, G., et al. 2007a, MNRAS, 377, 1531

Pastorello, A., Taubenberger, S., Elias-Rosa, N., et al. 2007b, MNRAS, 376, 1301

Perlmutter, S., Aldering, G., Goldhaber, G., et al. 1999, ApJ, 517, 565

Peters, N. 2000, Turbulent Combustion (Cambridge: Cambridge University Press)

Pfannes, J. M. M. 2006, PhD thesis, Universität Würzburg

Pfannes, J. M. M., Niemeyer, J. C., & Schmidt, W. 2010a, A&A, 509, A75+

Pfannes, J. M. M., Niemeyer, J. C., Schmidt, W., & Klingenberg, C. 2010b, A&A, 509, A74+

Phillips, M. M. 1993, ApJ, 413, L105

Phillips, M. M., Wells, L. A., Suntzeff, N. B., et al. 1992, AJ, 103, 1632

Piersanti, L., Cassisi, S., Iben, I., & Tornambé, A. 2002, in American Institute of Physics Conference Series, Vol. 637, Classical Nova Explosions, ed. M. Hernanz & J. José, 99–103

Piersanti, L., Cassisi, S., Iben, Jr., I., & Tornambé, A. 1999, ApJ, 521, L59

Piersanti, L., Cassisi, S., Iben, Jr., I., & Tornambé, A. 2000, ApJ, 535, 932

Ponchaut, N. F., Hornung, H. G., Pullin, D. I., & Mouton, C. A. 2006, Journal of Fluid Mechanics, 560, 103

Press, W. H., Teukolsky, S. A., Vetterling, W. T., & Flannery, B. P. 2007, Numerical Recipes: The Art of Scientific Computing, Vol. 3 (Cambridge University Press)

Pskovskii, I. P. 1977, Soviet Astronomy, 21, 675

Reinecke, M., Hillebrandt, W., & Niemeyer, J. C. 1999a, A&A, 347, 739

Reinecke, M., Hillebrandt, W., & Niemeyer, J. C. 2002a, A&A, 386, 936

Reinecke, M., Hillebrandt, W., & Niemeyer, J. C. 2002b, A&A, 391, 1167

Reinecke, M., Hillebrandt, W., Niemeyer, J. C., Klein, R., & Gröbl, A. 1999b, A&A, 347, 724

Reinecke, M. A. 2001, PhD thesis, Technical University of Munich, available at http://tumb1.biblio.tu-muenchen.de/publ/diss/allgemein.html

Riess, A. G., Filippenko, A. V., Challis, P., et al. 1998, AJ, 116, 1009

Röpke, F. K. 2005, A&A, 432, 969

Röpke, F. K. & Hillebrandt, W. 2005, A&A, 431, 635

Röpke, F. K., Hillebrandt, W., & Niemeyer, J. C. 2004a, A&A, 420, 411

Röpke, F. K., Hillebrandt, W., & Niemeyer, J. C. 2004b, A&A, 421, 783

Röpke, F. K., Hillebrandt, W., Niemeyer, J. C., & Woosley, S. E. 2006, A&A, 448, 1

Röpke, F. K., Hillebrandt, W., Schmidt, W., et al. 2007a, ApJ, 668, 1132

Röpke, F. K. & Niemeyer, J. C. 2007, A&A, 464, 683

Röpke, F. K., Niemeyer, J. C., & Hillebrandt, W. 2003, ApJ, 588, 952

Röpke, F. K. & Schmidt, W. 2009, in Interdisciplinary Aspects of Turbulence, ed. W. Hillebrandt & F. Kupka, Lecture Notes in Physics (Berlin: Springer-Verlag), 255–289

Röpke, F. K., Woosley, S. E., & Hillebrandt, W. 2007b, ApJ, 660, 1344

Ruiter, A. J., Belczynski, K., & Fryer, C. 2009, ApJ, 699, 2026

Ruiter, A. J., Sim, S. A., Hillebrandt, W., Fink, M., & Belczynski, K. 2010, in preparation

Scalzo, R. A., Aldering, G., Antilogus, P., et al. 2010, ApJ, 713, 1073

Schmidt, W. & Niemeyer, J. C. 2006, A&A, 446, 627

Schmidt, W., Niemeyer, J. C., & Hillebrandt, W. 2006a, A&A, 450, 265

Schmidt, W., Niemeyer, J. C., Hillebrandt, W., & Röpke, F. K. 2006b, A&A, 450, 283

Seitenzahl, I. R., Meakin, C. A., Townsley, D. M., Lamb, D. Q., & Truran, J. W. 2009, ApJ, 696, 515

Sharpe, G. J. 1999, MNRAS, 310, 1039

Sharpe, G. J. 2001, MNRAS, 322, 614

Shen, K. J. & Bildsten, L. 2009, ApJ, 699, 1365

Shen, K. J., Kasen, D., Weinberg, N. N., Bildsten, L., & Scannapieco, E. 2010, ApJ, 715, 767

Silverman, J. M., Ganeshalingam, M., Li, W., et al. 2010, ArXiv e-prints

Sim, S. A. 2007, MNRAS, 375, 154

Sim, S. A., Röpke, F. K., Hillebrandt, W., et al. 2010, ApJ, 714, L52

Sion, E. M. 1999, PASP, 111, 532

Smiljanovski, V., Moser, V., & Klein, R. 1997, Combustion Theory Modelling, 1, 183

Steinmetz, M., Muller, E., & Hillebrandt, W. 1992, A&A, 254, 177

Stewart, D. S. 1998, Symposium (International) on Combustion, 27, 2189

Stritzinger, M., Leibundgut, B., Walch, S., & Contardo, G. 2006, A&A, 450, 241

Sullivan, M., Le Borgne, D., Pritchet, C. J., et al. 2006, ApJ, 648, 868

Sussman, M., Smereka, P., & Osher, S. 1994, Journal of Computational Physics, 114, 146

Thielemann, F.-K., Hashimoto, M.-A., & Nomoto, K. 1990, ApJ, 349, 222

Thielemann, F.-K., Nomoto, K., & Hashimoto, M.-A. 1996, ApJ, 460, 408

Timmes, F. X., Hoffman, R. D., & Woosley, S. E. 2000, ApJS, 129, 377

Timmes, F. X. & Niemeyer, J. C. 2000, ApJ, 537, 993

Travaglio, C., Hillebrandt, W., Reinecke, M., & Thielemann, F.-K. 2004, A&A, 425, 1029

Truran, J. W., Arnett, W. D., & Cameron, A. G. W. 1967, Canadian Journal of Physics, 45, 2315

Wiggins, D. J. R. & Falle, S. A. E. G. 1997, MNRAS, 287, 575

Wiggins, D. J. R., Sharpe, G. J., & Falle, S. A. E. G. 1998, MNRAS, 301, 405

Woosley, S. E. 2007, ApJ, 668, 1109

Woosley, S. E., Taam, R. E., & Weaver, T. A. 1986, ApJ, 301, 601

Woosley, S. E. & Weaver, T. A. 1994a, in Les Houches Session LIV: Supernovae, ed. S. A. Bludman, R. Mochkovitch, & J. Zinn-Justin (Amsterdam: North-Holland), 63–154

Woosley, S. E. & Weaver, T. A. 1994b, ApJ, 423, 371

Yao, J. & Stewart, D. S. 1996, Journal of Fluid Mechanics, 309, 225

Yoon, S. & Langer, N. 2005, A&A, 435, 967

Yoon, S.-C. & Langer, N. 2004, A&A, 419, 623

Zel'dovich, Y. B., Librovich, V. B., Makhviladze, G. M., & Sivashinskii, G. I. 1970, Journal of Applied Mechanics and Technical Physics, 11, 264

Acknowledgments

First of all I would like to thank my supervisors Fritz Röpke and Wolfgang Hillebrandt for giving me the possibility to work on this interesting project and for their constant encouragement, advise, and patience.

I am also grateful to the whole thermonuclear supernova group at MPA for the good working atmosphere, the helpfulness, and friendship. Special thanks go to Markus Kromer and Stuart Sim for performing the radiative transfer simulations for my supernova models and for many fruitful discussions, to Ivo Seitenzahl for sharing his expertise about detonations and nucleosynthesis, and to Rüdiger Pakmor for providing help whenever there was a numerical or computational problem.

Moreover, I want to thank Ken Shen and Lars Bildsten for kindly providing the parameters for the minimum helium shell models of Chap. 3 and also for many helpful discussions.

I am grateful for the nice atmosphere at MPA and for the friendship with many great colleagues. This has essentially contributed to the progress of my work.

Last but not least, I am indebted to my family, especially to my parents and my brother, for their unresting support and encouragement.